

Die approbierte Originalversion dieser Dissertation ist an der Hauptbibliothek der Technischen Universität Wien aufgestellt (<http://www.ub.tuwien.ac.at>).

The approved original version of this thesis is available at the main library of the Vienna University of Technology (<http://www.ub.tuwien.ac.at/englweb/>).



Dissertation

**Instability Modes in Lid-Driven Triangular
Cavities
(Linear Stability Analysis)**

ausgeführt zum Zwecke der Erlangung des akademischen Grades eines Doktors
der technischen Wissenschaften unter der Leitung von

Univ.Prof. Dipl.-Phys. Dr.rer.nat. H. C. Kuhlmann
Institutsnummer E322
Institut für Strömungsmechanik und Wärmeübertragung

eingereicht an der Technischen Universität Wien
Fakultät für Maschinenwesen und Betriebswissenschaften

von

Manzoor Ahmed
Matrikelnummer 0725247
E322, Resselgasse 3, 1040 Wien.

Wien, im Juni 2011

To my loving parents.

Acknowledgements

I would like to express my sincere gratitude to my thesis supervisor Univ.Prof. Dipl.-Phys. Dr.rer.nat. Hendrik Christoph Kuhlmann. His suggestions, guidance, feedback, and discussions during this work are deeply appreciated.

I would like to thank Em.O.Univ.Prof. Dr.techn. Dipl.-Ing. Alfred Kluwick for being a referee to this work.

I am indebted to Dr. Christiane Lechner for reading the manuscript.

The support and help from Guido Fuchs, Ulrich Schoisswohl and Bernhard Weingartner in understanding most of the minor details during the initial phase of this work are invaluable.

The discussions and ideas of Markus Müllner and Thomas Müllner regarding the numerics are always fruitful.

Scientific and non-scientific discussions with Daniel Lanzerstorfer and Michael Lukasser was always necessary to win some comfort in life.

Nice wishes and prayers of my parents made this work possible.

Computing time provided by Zentraler Informatik Dienst (ZID) of the Vienna University of Technology is gratefully acknowledged.

The scholar ship provided by the Higher Education Commission of Pakistan (HEC) under the program "Pakistan Overseas Scholarship Program for PhD in Selected Fields" is gratefully acknowledged.

I would like to thank my wife, all the friends in Vienna and colleagues at the institute who made life easy for me in Vienna located so far away from my home (Pakistan).

Abstract

In this work incompressible Newtonian flow in lid-driven triangular cavities is studied. The primary interest is transition of two-dimensional steady-state flow to three-dimensional flow and the identification of physical mechanisms driving this transition. The neutral stability curves and perturbation flows are computed numerically through linear stability analysis. In order to get more insight into physical mechanisms kinetic energy analysis is carried out. The problem is investigated in the following parameter ranges

- Ratio between lengths of the moving lid and one of side-walls $\Gamma \in [0.2 - 4.0]$.
- Angle enclosed by the moving lid and a side-wall $\theta \in [15^\circ - 135^\circ]$.
- The motion of the lid is directed either towards or away from the corner where the angle θ is specified.

Five different instability modes are recognized in the above parameter range. Two of these modes are identified to be of centrifugal nature while the remaining three are of elliptic nature. The physical mechanisms driving the instability are explained by discussing representative cases for each of the modes. The analogies of the perturbation modes to those occurring in one and two-sided driven rectangular cavities are discussed.

Kurzfassung

In dieser Arbeit werden Strömungen in einseitig angetriebenen Dreiecksbehältern mit inkompressiblen, Newtonschen Fluiden untersucht. Das Auffinden des Übergangs zweidimensionaler stationärer in dreidimensionale Strömungen und die Identifikation der dafür verantwortlichen, physikalischen Mechanismen sind Hauptziele dieser Arbeit. Die neutralen Stabilitätskurven und die Störströmungen werden numerisch durch eine lineare Stabilitätsanalyse berechnet. Um einen Einblick in die physikalischen Mechanismen zu bekommen wird eine kinetische Energieanalyse durchgeführt. Das Problem wird in folgenden Parameterbereichen untersucht

- Verhältnis der Längen der bewegten Wand zu einer der ruhenden Wände $\Gamma \in [0, 2 - 4, 0]$.
- Winkel zwischen der bewegten Wand zu einer der ruhenden Wände $\theta \in [15^\circ - 135^\circ]$.
- Die Wand bewegt sich zur Ecke in der der Winkel angegeben ist hin oder von ihr weg.

Fünf verschiedene instabile Moden werden im obengenannten Parameterbereich gefunden. Zwei davon werden als zentrifugale, die anderen drei als elliptische Instabilitäten identifiziert. Die physikalischen Mechanismen der fünf Moden werden anhand von repräsentativen Fällen erklärt. Analogien zwischen den in dieser Arbeit gefundenen Moden mit solchen in ein- oder zweiseitig angetriebenen Rechtecksbehältern werden diskutiert.

Contents

Contents	v
1 Introduction	1
2 Problem Definition	5
2.1 Formulation of the problem	5
2.2 Energetics	9
2.3 Instability Mechanisms	10
2.3.1 Centrifugal Instability	10
2.3.2 Elliptic Instability	11
3 Numerical Methods	12
3.1 Basic state calculation	12
3.1.1 Equations for a single element	15
3.1.2 Newton-Raphson Method	16
3.2 Linear stability analysis	18
3.2.1 Equations for a single element	19
3.2.2 Krylov Subspace Iteration	20
3.2.3 Secant Method	22
3.2.4 Resolving Wave-Number	23
3.3 Solution Strategies	25
3.3.1 An Example	27
4 Validation of the Numerical Code	30
4.1 Validation of Basic State	30

4.2	Validation Linear Stability Analysis	35
5	Results and Discussion	39
5.1	Lid moving in positive x -direction	39
5.1.1	Result for right angled cavity	39
5.1.1.1	Mode 1: $\Gamma \leq 0.397$	41
5.1.1.2	Mode 2 and 3: $0.397 < \Gamma < 0.43$	46
5.1.1.3	Mode 4: aspect ratios $0.43 < \Gamma < 0.73$	51
5.1.1.4	Mode 5: aspect ratio $\Gamma > 0.73$	53
5.1.2	Variations of results with angle θ	55
5.1.3	Summary of results	61
5.2	Lid moving in negative x -direction	64
5.2.1	Mode 1	66
5.2.2	Mode 2 & mode 3	69
5.2.3	Mode 4 & mode 5	72
5.2.4	Summary of results	77
6	Conclusions	79
	References	81

Chapter 1

Introduction

Flow in lid-driven cavities served as a bench mark for validation of numerical methods and understanding of complex flows for decades. Relatively less work is available in three dimensional cavities of complex cross-section in comparison to the simple rectangular cavities. This work addresses the lid-driven cavity of triangular cross-section. A short review of some of the known and new results are presented to place the present work in proper context.

Two-dimensional steady-state flow in an equilateral triangular cavity was studied by [Ribbens et al. \[1994\]](#), where it was concluded that mean-square law on boundary velocities for the interior vorticity is not successful. [Jyotsna and Vanka \[1995\]](#) used triangular grid and multi-grid method to solve the Navier–Stokes equation and to overcome the problem of singularities associated with the corners of moving wall for isosceles cavity. [Li and Tang \[1996\]](#) further reported the flow topologies in triangular cavities with Reynolds number in the range of $Re \in [1 - 1500]$. [Gaskell et al. \[1999\]](#) used analytical specification of the vorticity near the singular corners while using the vorticity-stream-function formulation for the triangular cavity. [Erturk and Gokcol \[2007\]](#) employed the vorticity-stream-function formulation for triangular cavity and was able to obtain steady solutions at higher Reynolds numbers for different shapes of triangular cavities. The limit of Reynolds number to which such a steady-state two dimensional solution of the flow is valid is of primary interest. It is known that the flow eventually becomes three dimensional as the Reynolds number is increased beyond a certain critical value. More important is the physical Mechanism by which such

a two-dimensional flow in a container, unbounded in third direction, becomes three-dimensional. Objective of present work is to point out the limits of validity of two-dimensional solution of the flow and the underlying physical mechanism by which the flow become three dimensional in lid-driven triangular cavities. A short review of related physical mechanisms and some recent results are presented below.

Based on classical Rayleigh centrifugal instability theory Bayly [1988] derived that sufficient conditions for the centrifugal instability in inviscid flows are that the stream line shall be convex closed curves in some part of the flow with magnitude of circulation decreasing outward. Their results show that centrifugal instability is generic property of the circulating flows regardless of the symmetry or antisymmetry and degree of distortion from circularity. Sipp and Jacquin [2000] described the sufficient criterion for centrifugal instability in an inviscid flow based on the local magnitude of velocity, vorticity and local radius of curvature of a closed stream line. Kerswell [2002] discussed the elliptic instability of inviscid flows also showing the detuning and stabilization due to presence of viscosity. It was concluded that this instability is due parametric resonance of normal mode or a pair of normal modes of the undistorted rotating flow with the underlying strain field.

A closely related problem of flow in lid-driven rectangular cavity is extensively studied. The first known numerical results for non-linear solution of flow in a square lid-driven cavity in the Reynolds number range $Re \in [0 - 128]$, are that of Kawaguti [1961]. Simuni [1964] Extended the idea to rectangular cavities solving the unsteady Navier-Stokes equations up to $Re = 1000$. Burggraf [1966] showed that the later solutions were under resolved at $Re > 400$ by providing the first accurate solutions of the two-dimensional equations of motion in a square domain up to $Re = 400$. The results were used to discuss the earlier theories of Moffat [1963] and Batchelor [1956], regarding the development of corner vortices at finite Reynolds numbers and the centre vortex in the limit $Re \rightarrow \infty$. Flow visualization for finite aspect-ratio cavities were presented in the experimental work of Pan and Acrivos [1967] for $Re \in [20 - 4000]$. The range of two-dimensional numerical solutions in lid-driven square cavities were extended to $Re \leq 10000$ by Ghia et al. [1982] and Schreiber and Keller [1983]. It was observed that the numerical

solutions of flow becomes unsteady even in the strictly two-dimensional rectangular cavity. The unsteadiness and transition to three-dimensional flow were also observed experimentally and numerically for three-dimensional, span-wise homogeneous flow in a container of rectangular cross-section. The results of [Ding and Kawahara \[1998\]](#) provided the description of oscillating unstable mode in a square lid driven cavity. The missing modes were later found by complete parametric studies of three-dimensional instability in the rectangular cavities independently by [Theofilis \[2000\]](#) and [Albensoeder et al. \[2001\]](#), where the instability map of the flow by discovering the leading eigenmodes of the flow was completed. In the latter work a complete study of the effect of aspect ratio is also presented. In the work of [Albensoeder et al. \[2001\]](#) centrifugal instabilities were reported in one side driven cavities of rectangular cross-section where the instability was characterized by the kinetic energy budget and the inviscid criterion of [Sipp and Jacquin \[2000\]](#). In subsequent investigations [Kuhlmann and Albensoeder \[2004\]](#) reported the presence elliptic, quadripolar, centrifugal and cooperative instabilities in two-lid driven rectangular cavities. [Siegmann-Hegerfeld et al. \[2008\]](#), gave further experimentation and discussions of the different classes of instabilities in the rectangular two-lid driven cavity by establishing a close correspondence between linear-stability calculations and detailed LDV measurements.

The first three-dimensional flow structure that appears commonly in rectangular cavities as the Reynolds number is increased are the longitudinal Taylor-Görtler-like (TGL) vortices, as is obvious from the experimental results of [Koseff and Street \[1984a\]](#); [Koseff et al. \[1983\]](#), [Rhee et al. \[1984\]](#) and [Prasad and Koseff \[1989\]](#). The size of the TGL vortices was found to scale with the boundary layer thickness, which is usually small compared to the linear dimensions of the container. At further increase of the Reynolds number these vortices become time-dependent and start to meander [[Koseff and Street, 1984b](#)].

As for as the instabilities in triangular cavities is concerned [Kühnen \[2006\]](#) reported the experimental observations of instabilities occurring in a right-angled triangular cavities with the lid motion directed either away or towards the right angled corner. [González et al. \[2007\]](#) analysed the three dimensional (BiGlobal) instability of flows in different geometries including lid-driven equilateral triangular cavity. Some of the results to be presented in this thesis were also included

in [GONZÁLEZ et al. \[2011\]](#).

This thesis is organised in a way such that the problem to be investigated is presented in chapter [2](#), along with the governing equations and related boundary conditions, numerical methods employed are summarized in chapter [3](#), Validations of the numerical code are outlined in chapter [4](#), results are presented and discussed in chapter [5](#), finally some conclusive remarks are given in chapter [6](#).

Chapter 2

Problem Definition

We consider a Newtonian, incompressible fluid bounded in a prismatic cavity with a triangular cross-section as sketched in figure 2.1(a). The invariant cross section in the (x, y) -plane is made by three walls s_i , $i = 1, 2, 3$, of which s_1 and s_2 enclose an angle θ . While s_2 and s_3 are at rest, the side wall s_1 moves with a constant velocity $\pm U \mathbf{e}_x$ either in positive or negative x -direction with unit vector \mathbf{e}_x , i.e. either towards or away from the corner where the angle θ is specified and in the plane defining the triangle. To further characterize the geometry an aspect ratio is defined such that $\Gamma = s_2/s_1$ as the ratio between the length of the side wall s_2 and the length s_1 of the moving lid. The cavity length in the axial z -direction orthogonal to the (x, y) -plane is denoted by l . The corresponding span-wise aspect ratio is defined as $\Lambda = l/s_1$. The non dimensional geometry and coordinate system is shown in figure 2.1(b), where the lid of the cavity is taken as length scale.

2.1 Formulation of the problem

The motion of an incompressible Newtonian fluid with density ρ and kinematic viscosity ν is governed by the Navier–Stokes and continuity equations

$$\frac{\partial \mathbf{u}}{\partial t} + \mathbf{u} \cdot \nabla \mathbf{u} = -\nabla p + \frac{1}{\text{Re}} \nabla^2 \mathbf{u}, \quad (2.1a)$$

$$\nabla \cdot \mathbf{u} = 0 \quad (2.1b)$$

2. Problem Definition

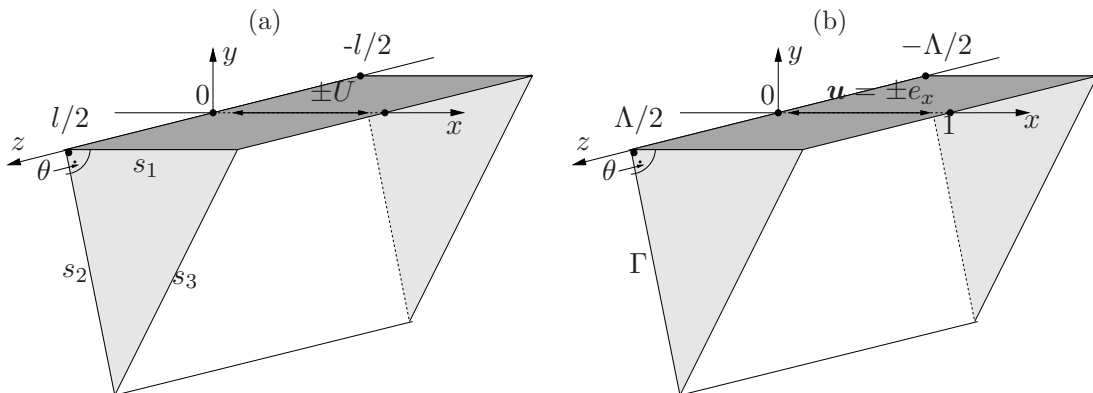


Figure 2.1: Sketch of the triangular cavity with dimensional (a) and non-dimensional variables (b). The black arrow indicates the motion of the lid.

where \mathbf{u} is the velocity vector and p the pressure field. Here we have used the scales s_1 , s_1/U , U , and ρU^2 for length, time, velocity and pressure. The Reynolds number is defined as

$$\text{Re} = \frac{U s_1}{\nu}. \quad (2.2)$$

The equations must be solved inside the prism defined above and subjected to no-slip boundary conditions on the three side walls, using Cartesian coordinates as sketched in figure 2.1(b)

$$\mathbf{u}(y = 0) = \pm \mathbf{e}_x, \quad (2.3a)$$

$$\mathbf{u}[y = -x \tan(\theta)] = 0, \quad (2.3b)$$

$$\mathbf{u} \left[y = \frac{-\Gamma \sin(\theta)}{\Gamma \cos(\theta) - 1.0} (x - 1.0) \right] = 0. \quad (2.3c)$$

For cavities with finite length the above boundary conditions must be supplied with the rigid boundary conditions on the side walls at $z = \pm \Lambda/2$. Since we are interested in the bulk-flow instabilities, we assume distant end walls corresponding to $\Lambda \rightarrow \infty$ and consider periodic boundary conditions in z -direction

$$[\mathbf{u}, p](z = \Lambda/2) = [\mathbf{u}, p](z = -\Lambda/2). \quad (2.4)$$

In the absence of side walls, for $\Lambda \rightarrow \infty$ the problem is characterized by four

2. Problem Definition

parameters, the Reynolds number Re , the aspect ratio Γ , the angle θ , and the direction of motion of lid.

From the periodic boundary conditions 2.4 it follows that the equations 2.1 have a steady two-dimensional solution (\mathbf{u}_0, p_0) at moderate Reynolds number. It is assumed that the steady solution is unique as there has been no evidence of multiplicity of two-dimensional flow in such a one-sided driven cavity.

As the primary interest here is the linear stability of the two-dimensional steady basic flow, we consider the perturbations $(\tilde{\mathbf{u}}, \tilde{p})$ such that the total flow field can be written as

$$\mathbf{u} = \mathbf{u}_0(x, y) + \tilde{\mathbf{u}}(x, y, z, t), \quad (2.5a)$$

$$p = p_0(x, y) + \tilde{p}(x, y, z, t). \quad (2.5b)$$

Substituting (2.5) into (2.1), linearising with respect to $\tilde{\mathbf{u}}$ and subtracting the basic steady-state flow from the resulting equations, the perturbation equations become

$$\frac{\partial \tilde{\mathbf{u}}}{\partial t} + \mathbf{u}_0 \cdot \nabla \tilde{\mathbf{u}} + \tilde{\mathbf{u}} \cdot \nabla \mathbf{u}_0 = -\nabla \tilde{p} + \frac{1}{\text{Re}} \nabla^2 \tilde{\mathbf{u}}, \quad (2.6a)$$

$$\nabla \cdot \tilde{\mathbf{u}} = 0. \quad (2.6b)$$

The perturbation flow must satisfy the no-slip boundary conditions $\tilde{\mathbf{u}} = 0$ at all boundaries. The coefficients of (2.6) do not depend on z and t which allows an ansatz in form of normal modes

$$\tilde{\mathbf{u}} = \hat{\mathbf{u}}(x, y) e^{\gamma t + i k z} + \text{c.c.}, \quad (2.7a)$$

$$\tilde{p} = \hat{p}(x, y) e^{\gamma t + i k z} + \text{c.c.} \quad (2.7b)$$

where the complex conjugate (c.c) render the perturbations real. The wave number k in \Re is assumed to be real while $\gamma = \sigma + i\omega$ is the complex growth rate with real growth rate σ and oscillation frequency ω . Substituting the ansatz (2.7) into

2. Problem Definition

the perturbation equations (2.6) yield

$$\left(\mathcal{L} + \frac{\partial u_0}{\partial x}\right) \hat{u} + \hat{v} \frac{\partial u_0}{\partial y} + \frac{\partial \hat{p}}{\partial x} = -\gamma \hat{u}, \quad (2.8a)$$

$$\left(\mathcal{L} + \frac{\partial v_0}{\partial x}\right) \hat{v} + \hat{u} \frac{\partial v_0}{\partial y} + \frac{\partial \hat{p}}{\partial y} = -\gamma \hat{v}, \quad (2.8b)$$

$$\mathcal{L} \hat{w} + ik \hat{p} = -\gamma \hat{w}, \quad (2.8c)$$

$$\frac{\partial \hat{u}}{\partial x} + \frac{\partial \hat{v}}{\partial y} + ik \hat{w} = 0. \quad (2.8d)$$

with \mathcal{L} the linear advection-diffusion operator

$$\mathcal{L} = u_0 \frac{\partial}{\partial x} + v_0 \frac{\partial}{\partial y} - \frac{1}{\text{Re}} \left(\frac{\partial^2}{\partial x^2} + \frac{\partial^2}{\partial y^2} - k^2 \right). \quad (2.9)$$

Equations 2.8 represent a complex singular eigenvalue problem. Following the transformation of [González et al., 2007] $\hat{w} \rightarrow -i\hat{w}$, it is possible to deduce a real eigenvalue problem

$$A \cdot \mathbf{X} = -\gamma B \cdot \mathbf{X}. \quad (2.10)$$

From a heuristic point of view it can be stated the the overall flow consists of a unique steady-state basic flow plus a series of perturbation modes (eigenmodes) with variable wave numbers k_i and growth rates σ_i . An eigenmode can now either grow ($\sigma_i > 0$), decay ($\sigma_i < 0$) or remain the same ($\sigma_i = 0$). For the flow to be stable all the eigenmodes need to be decaying. So for a given geometry and certain wave number k one has to find an eigenmode with largest growth rate and trace it until $\sigma = 0$ by varying the Reynold number Re . The Re obtained is the neutral Reynolds number Re_n . In order to obtain the critical Reynolds number Re_c one has to find the neutral Reynolds number for all the physical wave numbers, and take the minimum. Symbolically it can be stated as

$$\text{Re}_c = \min_i (\text{Re}_{n,i}(k_i)). \quad (2.11)$$

2.2 Energetics

Having obtained the normal modes the local transfer of kinetic energy between the basic flow and the perturbations provides insight into the instability mechanism. To that end we consider the Reynolds–Orr equation similar as, e.g., in [Albensoeder et al. \[2001\]](#). It is obtained by multiplying the perturbation equation [2.6a](#) with $\tilde{\mathbf{u}}$ and integrating over the finite prism V with span-wise length of $\lambda = 2\pi/k$ corresponding to one period of the flow in z -direction.

$$\frac{1}{D_*} \frac{dE_{\text{kin}}}{dt} = -1 + \sum_{i=1}^4 \int_V I_i dV. \quad (2.12)$$

where we normalized the rate of change of energy by the dissipation in the volume $D_* = \int_V (\nabla \times \tilde{\mathbf{u}})^2 dV$. The local energy production can be decomposed in Cartesian coordinates

$$I_1 = -\frac{1}{D_*} \left(\tilde{u} \frac{\partial u_0}{\partial x} \right) \tilde{u}, \quad (2.13a)$$

$$I_2 = -\frac{1}{D_*} \left(\tilde{v} \frac{\partial u_0}{\partial y} \right) \tilde{u}, \quad (2.13b)$$

$$I_3 = -\frac{1}{D_*} \left(\tilde{u} \frac{\partial v_0}{\partial x} \right) \tilde{v}, \quad (2.13c)$$

$$I_4 = -\frac{1}{D_*} \left(\tilde{v} \frac{\partial v_0}{\partial y} \right) \tilde{v}. \quad (2.13d)$$

Note that the local pressure work $-\tilde{\mathbf{u}} \cdot \nabla \tilde{p}$ and advection term $-\tilde{\mathbf{u}} \cdot (\mathbf{u}_0 \cdot \nabla \tilde{\mathbf{u}})$ vanishes on integration over the volume for the present boundary conditions. The physical interpretation of I_1 , for example, is the rate of change of kinetic energy density of the perturbation caused by basic state momentum u_0 being transported in x direction by the action of the perturbation flow component \tilde{u} . For the energy analysis those regions in space where the energy transfer is positive can be identified and in case of the relative dominance of certain terms allows the identification of the physical mechanisms involved.

In certain situations it is better to use a decomposition into coordinates aligned with the local basic flow \mathbf{u}_0 . If the perturbation velocity is decomposed

into $\tilde{\mathbf{u}} = \tilde{\mathbf{u}}_{\perp} + \tilde{\mathbf{u}}_{\parallel}$ with

$$\tilde{\mathbf{u}}_{\parallel} = \frac{(\tilde{\mathbf{u}} \cdot \mathbf{u}_0)\mathbf{u}_0}{u_0^2} \quad \text{and} \quad \tilde{\mathbf{u}}_{\perp} = \tilde{\mathbf{u}} - \tilde{\mathbf{u}}_{\parallel} \quad (2.14)$$

the terms I_i in (2.12) must be replaced by I'_i given by

$$I'_1 = -\frac{1}{D_*} \tilde{\mathbf{u}}_{\perp} \cdot (\tilde{\mathbf{u}}_{\perp} \cdot \nabla \mathbf{u}_0), \quad (2.15a)$$

$$I'_2 = -\frac{1}{D_*} \tilde{\mathbf{u}}_{\parallel} \cdot (\tilde{\mathbf{u}}_{\perp} \cdot \nabla \mathbf{u}_0), \quad (2.15b)$$

$$I'_3 = -\frac{1}{D_*} \tilde{\mathbf{u}}_{\perp} \cdot (\tilde{\mathbf{u}}_{\parallel} \cdot \nabla \mathbf{u}_0), \quad (2.15c)$$

$$I'_4 = -\frac{1}{D_*} \tilde{\mathbf{u}}_{\parallel} \cdot (\tilde{\mathbf{u}}_{\parallel} \cdot \nabla \mathbf{u}_0). \quad (2.15d)$$

2.3 Instability Mechanisms

Besides determining the critical parameters for stability, the purpose of the present work is to analyse the mechanism of instability and relate them with the known mechanisms of instability. In this section a brief introduction of two types of instability mechanisms will be given that occur in the triangular cavities.

2.3.1 Centrifugal Instability

One of the earliest mechanisms recognised for instability is centrifugal instability. The necessary condition for the such an instability is the existence of convex streamlines in a flow with decreasing angular momentum outward from the center. So that exchange of fluid element with high angular momentum at small radii with a fluid element with low angular momentum at higher radii will results in an energy gain. The first sufficient criterion for centrifugal instability of inviscid rotating flow was given by [Rayleigh, Lord \[1917\]](#), according to which instability could evolve when the Rayleigh circulation criterion

$$\frac{d}{dr}(\Omega r^2)^2 < 0 \quad (2.16)$$

2. Problem Definition

is fulfilled, where $\Omega = \Omega(r)$ is the angular velocity of rotating fluid $\mathbf{u} = \Omega r \mathbf{e}_\phi$. Bayly [1988] generalized the criterion for any close streamline in a flow. An equivalent local criterion for centrifugal instability of inviscid fluid was given by Sipp and Jacquin [2000], which can be stated as an inviscid flow could become unstable if

$$\frac{V_0}{R}(\varpi_0) < 0 \quad (2.17)$$

all along a closed streamline, where ϖ_0 being the vorticity of the basic state, $V_0 = |\mathbf{u}_0|$ the velocity magnitude and R the local radius of curvature of the closed streamline. R can be evaluated as

$$R = \frac{V_0^3}{(\nabla\psi) \cdot (\mathbf{u}_0 \cdot \nabla \mathbf{u}_0)} \quad (2.18)$$

ψ being the stream function. It shall be noted that this criterion is valid for inviscid flow only. However it will be used as an indication of centrifugal instability if the maximum of local energy transfer occurs at a location where this criterion also holds.

2.3.2 Elliptic Instability

The elliptic instability mechanism in contrast to centrifugal mechanism of instability was recognized in the mid 1970's. The linear instability mechanism by which three-dimensional flows can be generated in the region of two-dimensional, elliptic streamlines is now known as elliptic instability mechanism. Kerswell [2002] gave a detailed discussion of the elliptic instability mechanism, where it was concluded that the instability is primarily a parametric resonance of normal mode or pair of normal modes of undistorted rotating flows with underlying strain field. It was Sipp and Jacquin [1998] who stated that the amplification of the modes are higher at the center of deformed vortex. The criterion which will be used for detection of such instability is that the local energy transfer takes maximum near the center of some elliptically deformed vortex. Generally the criterion (2.17) for centrifugal instability does not hold at the center of a vortex.

Chapter 3

Numerical Methods

In this chapter the numerical methods and information necessary to solve the mathematical formulation presented in chapter 2 will be discussed. Initially the methods necessary to calculate the basic state are discussed in section 3.1. The techniques related to the perturbation flow field and the eigenvalue problem are presented in section 3.2. Finally the computational strategies are discussed in section 3.3.

3.1 Basic state calculation

The natural choice for solution of the steady Navier–Stoke equations in the present geometry is the finite element method. The variational formulation of the Navier–Stoke equations had been intensively discussed in literature, a few examples are Ben [2006]; Chung [1978]; Dick [2009]; Zienkiewicz et al. [2008]. In the following only the present implementation procedure will be discussed starting from the weak form of the equations which can be stated as

$$(\mathbf{u} \cdot \nabla \mathbf{u} + \nabla p - \frac{1}{\text{Re}} \nabla^2 \mathbf{u}) \Phi_i = 0, \quad (3.1a)$$

$$(\nabla \cdot \mathbf{u}) \Psi_j = 0. \quad (3.1b)$$

where Φ_i and Ψ_j are the velocity and pressure basis functions respectively. The next step is to integrate these equations in the domain Ω . Any strong solution

will obey the following equations.

$$\int (\mathbf{u} \cdot \nabla \mathbf{u} + \nabla p - \frac{1}{\text{Re}} \nabla^2 \mathbf{u}) \Phi_i d\Omega = 0, \quad (3.2a)$$

$$\int (\nabla \cdot \mathbf{u}) \Psi_j d\Omega = 0. \quad (3.2b)$$

The 2nd order viscous term can be integrated by parts

$$- \int \left(\frac{d^2 \mathbf{u}}{dx^2} \right) \Phi_i d\Omega = - \frac{d}{dx} \left(\frac{d\mathbf{u}}{dx} \Phi_i \right) |_{\partial\Omega} + \int \frac{d\mathbf{u}}{dx} \frac{d\Phi_i}{dx} d\Omega, \quad (3.3a)$$

$$- \int \left(\frac{d^2 \mathbf{u}}{dy^2} \right) \Phi_i d\Omega = - \frac{d}{dy} \left(\frac{d\mathbf{u}}{dy} \Phi_i \right) |_{\partial\Omega} + \int \frac{d\mathbf{u}}{dy} \frac{d\Phi_i}{dy} d\Omega. \quad (3.3b)$$

As a usual practice the basis function Φ_i is assumed in a way that it vanishes on the boundary $\partial\Omega$, where the velocity is defined. So the boundary terms disappear and the final set of equations can be written as

$$\int ((\mathbf{u} \cdot \nabla \mathbf{u} + \nabla p) \Phi_i + \frac{1}{\text{Re}} \nabla \mathbf{u} \cdot \nabla \Phi_i) d\Omega = 0, \quad (3.4a)$$

$$\int (\nabla \cdot \mathbf{u}) \Psi_j d\Omega = 0. \quad (3.4b)$$

It should be noted that the boundary terms will not vanish if the boundary conditions are of Neumann or Robin type for the velocity. However such boundary conditions don't occur in the present problem. For the present study velocity and pressure are approximated by quadratic and linear interpolation polynomials respectively, where triangular elements of Taylor–Hood type as shown in figure 3.1 are employed. A single element consists of 6 nodes, 3 nodes at the vertices and 3 mid-side nodes. As such pressure is approximated only at the vertices of the element. The linear basis interpolation functions for such an element can be written as

$$\Psi_1 = \frac{1}{2A} \begin{vmatrix} x & y & 1 \\ x_2 & y_2 & 1 \\ x_3 & y_3 & 1 \end{vmatrix}, \quad \Psi_2 = \frac{1}{2A} \begin{vmatrix} x_1 & y_1 & 1 \\ x & y & 1 \\ x_3 & y_3 & 1 \end{vmatrix}, \quad \Psi_3 = 1 - \Psi_1 - \Psi_2 \quad (3.5)$$

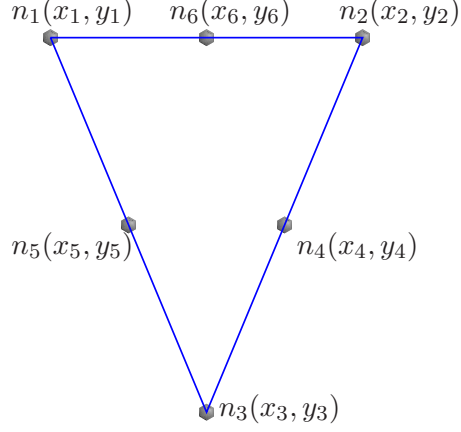


Figure 3.1: Taylor–Hood type of triangular element.

where A is the area of the element $A = \frac{1}{2} \begin{vmatrix} x_1 & y_1 & 1 \\ x_2 & y_2 & 1 \\ x_3 & y_3 & 1 \end{vmatrix}$. The quadratic interpolation functions for the velocities can be expressed in terms of linear pressure basis interpolation functions by the relations

$$\begin{aligned} \Phi_1 &= \Psi_1(2\Psi_1 - 1), & \Phi_4 &= 4\Psi_2\Psi_3, \\ \Phi_2 &= \Psi_2(2\Psi_2 - 1), & \Phi_5 &= 4\Psi_1\Psi_3, \\ \Phi_3 &= \Psi_3(2\Psi_3 - 1), & \Phi_6 &= 4\Psi_1\Psi_2. \end{aligned} \tag{3.6}$$

Velocity and pressure in an element can be approximated as

$$\begin{aligned} u^h(x, y) &= \sum_{i=1}^6 \Phi_i(x, y)u_i, \\ v^h(x, y) &= \sum_{i=1}^6 \Phi_i(x, y)v_i, \\ p^h(x, y) &= \sum_{i=1}^3 \Psi_i(x, y)p_i. \end{aligned} \tag{3.7}$$

The superscript h represents the element h . u_i, v_i and p_i are the nodal values of the velocities and pressure. Both the velocities are approximated with same degree of polynomials.

3.1.1 Equations for a single element

Substitution of the velocity and pressure interpolation functions 3.7 and the basis function 3.5 and 3.6 in the so called weak integral equation 3.4 will yield a non-linear equation for a single element. The equation for a single element can be written in scalar form symbolically as

$$A_{NRxM}u_M u_R + A_{NRyM}v_M u_R + B_{NQx}p_Q + C_{NM}u_M = 0, \quad (3.8a)$$

$$A_{NRxM}u_M v_R + A_{NRyM}v_M v_R + B_{NQy}p_Q + C_{NM}v_M = 0, \quad (3.8b)$$

$$D_{MxQ}u_M + D_{MyQ}v_M = 0. \quad (3.8c)$$

with $N, M, R = 1, 2, \dots, 6$ the quadratic nodal points and $Q = 1, 2, 3$ the linear nodes (vertices). The coefficients appearing in equation 3.8 are given by

$$\begin{aligned} A_{NRiM} &= \int \left(\Phi_N \Phi_M \frac{\partial \Phi_R}{\partial i} \right) d\Omega \quad (\text{convective matrix}), \\ B_{NQi} &= \int \left(\Phi_N \frac{\partial \psi_Q}{\partial i} \right) d\Omega \quad (\text{Pressure matrix}), \\ C_{NM} &= \frac{1}{\text{Re}} \int \left(\frac{\partial \Phi_N}{\partial x} \frac{\partial \Phi_M}{\partial x} + \frac{\partial \Phi_N}{\partial y} \frac{\partial \Phi_M}{\partial y} \right) d\Omega \quad (\text{dissipation matrix}), \\ D_{MiQ} &= \int \left(\frac{\partial \Phi_M}{\partial i} \Psi_Q \right) d\Omega \quad (\text{continuity matrix}). \end{aligned} \quad (3.9)$$

with $i = [x, y]$ and Ω now represent the domain of a single element. The integrands in equation 3.9 are polynomials and can be evaluated either numerically or analytically such as e.g

$$\int (\Psi_1^a \Psi_2^b) d\Omega = \frac{a!b!}{(a+b+2)!} 2A_e \quad (3.10)$$

where A_e is the area of element. The remaining basis functions can be written in terms of (Ψ_1, Ψ_2) using relations 3.5 and 3.6. Equations 3.8 is still non-linear in terms of the nodal values due to convective terms. It will yield a non-linear global system of equation, which can either be solved with iterative methods or any non-linear method of algebraic system such as Newton-Raphson method. An alternative is to apply the Newton-Raphson method to the equations on element

basis and then form the global system of equations.

3.1.2 Newton-Raphson Method

Equations 3.8 are set of fifteen non-linear algebraic equations more precisely 2×6 equations from momentum and 3 from continuity equation. The equations can be rewritten as

$$A(X)X = b \quad (3.11)$$

where X represents the nodal unknowns. The Newton-Raphson method can now be employed on an element to form global linear system of equations as following.

1. Calculate the residual on element base

$$r^k = A(X^k)X^k - b \quad (3.12)$$

For the first iteration $k = 0$ nodal values X^0 can be chosen randomly.

2. Assemble the global residual vector r_{global}^k by adding the element terms at proper locations corresponding to the connectivity of elements and apply the boundary conditions such that $r_{global}^k[i] = 0$ at boundary nodes i
3. Compute the Jacobian for the nodal values

$$J_{j,i}^k = \left. \frac{\partial r_j}{\partial X_i} \right|_{X=X^k} \quad (3.13)$$

4. Assemble the global Jacobian Matrix J_{global}^k by adding the element terms at proper locations corresponding to the connectivity of elements and apply the boundary conditions such that $J_{global}^k[i, j] = 0$ and $J_{global}^k[i, i] = 1.0$ for the equation of boundary nodes i
5. Solve the linear system of equations

$$J_{global}^k Y^k = -r_{global}^k \quad (3.14)$$

6. Calculate new vector $X^{k+1} = X^k + Y^k$

7. Calculate new residual r_{global}^{k+1} as in step 1 and 2 using the new vector X^{k+1}
- a) If the norm of the residual is sufficiently small along with maximum difference between any nodal value at present iteration and previous iteration is sufficiently small or the maximum number of iteration is exceeded i.e.

$$\|r_{global}^{k+1}\|_2 < \epsilon_1 \text{ and } Max(|r_{global}^{k+1} - r_{global}^k|) < \epsilon_2 \quad \text{or} \quad k > k_{max} \quad (3.15)$$

the iteration is stopped, X^{k+1} is solution vector.

- b) other wise resume the process at step 3

The above process suffers from two major drawbacks. If the initial guess X^0 is too far from the solution the iteration may diverge. A remedy is to start calculations at low Reynolds number and to increase the Reynolds number to the desired value in steps, using the solution of low Reynolds number as the initial guess for the next calculation. The second drawback is the overshooting of the iterative process over the original solution which can be cured by application of modified Armijo rule in step 7(b). The modified Armijo rule can be stated as

1. $\alpha = 0.50$
2. for $i = 1, 2, ..n_{Armijo}$
3. If $\|r_{global}^{k+1}\|_2 > \|r_{global}^k\|_2$
 $X^{k+1} = \alpha X^{k+1}$
 $\alpha = \frac{\alpha}{2.0}$

The resulting algebraic equations in step 5 were solved using the open source software SuperLU [Demmel et al. \[1999\]](#). The exact integrations 3.10 was used to reduce the numerical noise. The convergence criterion in step 7 were set to

$$\epsilon_1 = 10^{-30}, \quad \epsilon_2 = 10^{-15} \quad (3.16)$$

It takes normally 5-10 iteration depending on mesh size with a nominal step of 500 in Reynolds number to achieve this convergence criterion fulfilled.

3.2 Linear stability analysis

Using the velocity basis functions as weights for the momentum and pressure basis functions as weights for the continuity of the perturbation equations 2.8, the weak form of the system can be written as

$$\begin{aligned}
\left(\left(u_0 \frac{\partial}{\partial x} + v_0 \frac{\partial}{\partial y} - \frac{1}{\text{Re}} \left(\frac{\partial^2}{\partial x^2} + \frac{\partial^2}{\partial y^2} - k^2 \right) + \frac{\partial u_0}{\partial x} \right) \hat{u} + \hat{v} \frac{\partial u_0}{\partial y} + \frac{\partial \hat{p}}{\partial x} \right) \Phi_i &= -\gamma \hat{u} \Phi_i, \\
\left(\left(u_0 \frac{\partial}{\partial x} + v_0 \frac{\partial}{\partial y} - \frac{1}{\text{Re}} \left(\frac{\partial^2}{\partial x^2} + \frac{\partial^2}{\partial y^2} - k^2 \right) + \frac{\partial v_0}{\partial y} \right) \hat{v} + \hat{u} \frac{\partial v_0}{\partial x} + \frac{\partial \hat{p}}{\partial y} \right) \Phi_i &= -\gamma \hat{v} \Phi_i, \\
\left(\left(u_0 \frac{\partial}{\partial x} + v_0 \frac{\partial}{\partial y} - \frac{1}{\text{Re}} \left(\frac{\partial^2}{\partial x^2} + \frac{\partial^2}{\partial y^2} - k^2 \right) \right) \hat{w} + k \hat{p} \right) \Phi_i &= -\gamma \hat{w} \Phi_i, \\
\left(\frac{\partial \hat{u}}{\partial x} + \frac{\partial \hat{v}}{\partial y} - k \hat{w} \right) \Psi_j &= 0.
\end{aligned} \tag{3.17}$$

$i = 1, 2, \dots, n_V$ and $j = 1, 2, \dots, n_p$ where n_V is the total number of velocity nodes and n_p is the total number of pressure nodes in the element. It shall be noted that a transformation $\hat{w} \rightarrow -i\hat{w}$ was used in the above equation to deduce the coefficients of system as real. The basis functions are the same as before, and the perturbation variables on a Taylor-Hood element figure 3.1 are approximated by

$$\begin{aligned}
\hat{u}^h(x, y) &= \sum_{i=1}^6 \Phi_i(x, y) \hat{u}_i, \\
\hat{v}^h(x, y) &= \sum_{i=1}^6 \Phi_i(x, y) \hat{v}_i, \\
\hat{w}^h(x, y) &= \sum_{i=1}^6 \Phi_i(x, y) \hat{w}_i, \\
\hat{p}^h(x, y) &= \sum_{i=1}^3 \Psi_i(x, y) \hat{p}_i.
\end{aligned} \tag{3.18}$$

Again the superscript h denotes the element h . \hat{u}_i , \hat{v}_i , \hat{w}_i and \hat{p}_i are the nodal values of velocities and pressure.

3.2.1 Equations for a single element

Substitution of the interpolation function 3.18 and the basis functions 3.5 and 3.6 into the perturbation equations 3.17 and integrating over the element will yield the system of equations for single element, which symbolically can be written as

$$\begin{aligned}
& \left(A_{MNRx}u_0^N + A_{MNRy}v_0^N + \frac{k^2}{\text{Re}}B_{MR} + F_{MR} + A_{MRNx}u_0^N \right) \hat{u}_R + \\
& \quad A_{MRNy}u_0^N \hat{v}_R + D_{MQx}\hat{p}_Q = -\gamma B_{MR}\hat{u}_R, \\
& \left(A_{MNRx}u_0^N + A_{MNRy}v_0^N + \frac{k^2}{\text{Re}}B_{MR} + F_{MR} + A_{MRNy}v_0^N \right) \hat{u}_R + \\
& \quad A_{MRNx}v_0^N \hat{u}_R + D_{MQy}\hat{p}_Q = -\gamma B_{MR}\hat{v}_R, \\
& \left(A_{MNRx}u_0^N + A_{MNRy}v_0^N + \frac{k^2}{\text{Re}}B_{MR} + F_{MR} \right) \hat{w}_R + kC_{MQ}\hat{p}_Q = \\
& \quad -\gamma B_{MR}\hat{w}_R, \\
& G_{MxQ}\hat{u}_M + G_{MyQ}\hat{v}_M - kC_{MQ}\hat{w}_M = 0.
\end{aligned} \tag{3.19}$$

With $N, M, R = 1, 2, \dots, 6$ the velocity nodes and $Q = 1, 2, 3$ the pressure nodes. u_0^N and v_0^N represents the basic state at node N . The definitions of the individual terms are

$$\begin{aligned}
A_{MNRi} &= \int \Phi_M \Phi_N \frac{\partial \Phi_R}{\partial i} d\Omega, \quad B_{MR} = \int \Phi_M \Phi_R d\Omega, \\
C_{MQ} &= \int \Phi_M \Psi_Q d\Omega, \quad D_{MQi} = \int \Phi_M \frac{\partial \Psi_Q}{\partial i} d\Omega, \\
F_{MR} &= \frac{1}{\text{Re}} \int \left(\frac{\partial \Phi_M}{\partial x} \frac{\partial \Phi_R}{\partial x} + \frac{\partial \Phi_M}{\partial y} \frac{\partial \Phi_R}{\partial y} \right) d\Omega, \quad G_{MiQ} = \int \frac{\partial \Phi_M}{\partial i} \Psi_Q d\Omega.
\end{aligned} \tag{3.20}$$

with $i = x, y$. Again the second order derivative terms are integrated by parts. The terms in equation 3.20 are evaluated analytically using the relation 3.10. Equations 3.19 represent a system of 21 equations and unknowns for the present Taylor-Hood triangular element, with eighteen equations from the momentum and three from the continuity equations.

When the individual element equations 3.19 are assembled into the global system through the connectivity of the elements, yields an eigenvalue problem

which can be written as

$$A\hat{X} = -\gamma B\hat{X} \quad (3.21)$$

where A and B are real with B singular, which will have a solution either real or in form of complex conjugate pair.

3.2.2 Krylov Subspace Iteration

The important eigenvalues for the linear stability theory are those which lie close to $\gamma_r = \sigma = 0$. An iterative method "Arnoldi algorithm", originally proposed by Saad [1980] and discussed in detail by Theofilis [2003], is used to determine these eigenvalues in present study. As this algorithm yields eigenvalues with largest modulus, and the requirement for our study is to find the eigenvalues with largest real part, the original problem 3.21 has to be transformed such that the required eigenvalues will have the largest modulus near the imaginary axis. Defining

$$\mu = -\gamma^{-1} \quad (3.22)$$

will convert the problem to

$$A^{-1}B\hat{X} = \mu\hat{X}, \quad A^{-1}B = C, \quad C\hat{X} = \mu\hat{X}. \quad (3.23)$$

The generalized eigenvalue problem is now converted to a standard EVP. A finite number of eigenvalues m (m being the number of Krylov subspaces which is small compared to the dimensions of A) for a certain wave-number k and basic flow at a certain Reynolds number Re can be determined with the Arnoldi algorithm as:

1. choose an initial random vector v_1 apply the boundary conditions and normalize it to 1.
2. repeat for $i = 2, 3, ..m$
 - a) calculate $v_i = Cv_{i-1}$ which is equivalent to solve $Av_i = Bv_{i-1}$
 - b) for j from 1 to $i - 1$
 - * $h_{j,i-1} = (v_j, v_i)$
 - * $v_i = v_i - h_{j,i-1}v_j$

c) $h_{i,i-1} = \|v_i\|$

d) $v_i = \frac{v_i}{h_{i,i-1}}$

The algorithm yields an orthonormal basis $V_m = [v_1, v_2, \dots, v_m]$ of the Krylov subspace $K_m = \text{span}\{v_1, Cv_1, \dots, C^{m-1}v_1\}$ and an upper Hessenberg matrix $H_m = \{h_{i,j}\}$. The eigenvalues of the matrix H_m are approximation of the m largest eigenvalues of the problem 3.23, from which the eigenvalues of the original problem 3.21 can be evaluated through relation 3.22. The eigenvectors associated with these eigenvalues can be obtained by

$$\hat{X}_i = V_M \hat{y}_i \tag{3.24}$$

where \hat{y}_i is an eigenvector of H_m associated with the eigenvalue μ_i . The open source `SupelU` Demmel et al. [1999] is used for the LU decomposition of the system in step 2a of the algorithm. The decomposed matrices can be used for the subsequent iterations where as the eigenvalues of the upper Hessenberg matrix H_m are computed through LAPACK Anderson et al. [1999]. It should be noted that the eigenvalues evaluated through the above Arnoldi algorithm are the approximate eigenvalue with the smallest modulus of the original problem 3.21, which lie close to the imaginary axis. Therefore it is necessary to step from low Reynolds number to higher values, so that none of the positive eigenvalue is missed.

Cayley Validation

Eigenvalues with moderate or even largest real part, that have a large imaginary part might be missed by the Arnoldi algorithm described above. It is necessary to check that such eigenvalues are not missed. Cayley transformation of the problem as was proposed by Meerbergen et al. [1994] can be applied to validate the eigenvalues evaluated through subspace iteration. The original problem 3.21 can be written as

$$(A - \alpha_1 B)\hat{X} - \eta(A - \alpha_2 B)\hat{X} = 0. \tag{3.25}$$

The relation between the eigenvalues γ_i of the original problem 3.21 and the new eigenvalues η_i of equation 3.25 can be stated as

$$\gamma_i = \frac{\eta_i \alpha_2 - \alpha_1}{1 - \eta_i}. \quad (3.26)$$

The parameters (α_1, α_2) for the Cayley transformation can be computed from the subspace eigenvalues already evaluated. If the eigenvalues from the Arnoldi method are ordered with decreasing real parts such that $(\sigma_1 > \sigma_2 \dots > \sigma_m)$ then the parameters can be evaluated as

$$\begin{aligned} \alpha_1 &= \frac{(-1 - \rho_{user})\sigma_1 - 2\sigma_{ref}}{1 - \rho_{user}}, \\ \alpha_2 &= 2\sigma_{ref} - \alpha_1. \end{aligned} \quad (3.27)$$

where σ_{ref} is the real part of a reference eigenvalue γ_{ref} which can be taken any of the eigenvalues evaluated with acceptable degree of confidence in the subspace iteration. The parameter ρ_{user} can be taken between 1.2 and 1.5 as was reported by Meerbergen et al. [1994]. The largest eigenvalues of problem 3.25 shall be evaluated either by the Arnoldi or implicitly restarted Arnoldi method such that at least two of the eigenvalues used in parameters evaluation e.g. γ_1, γ_{ref} appears from the relation 3.26 with an acceptable degree of tolerance. The Cayley transformation acts as validation of the eigenvalues evaluated by the shift invert with zero shift, and will deliver eigenvalues in the neighbourhood of the eigenvalue with largest real part from the shift invert step having high imaginary parts, if those were missed in the initial step.

3.2.3 Secant Method

The Arnoldi algorithm augmented optionally with the Cayley transformation stated above will yield the eigenvalue with the largest real part for a certain Reynolds number Re at a certain wave-number k . To obtain the neutral Reynolds number Re_n so that $\sigma_{max} = 0$ the secant method can be used. To this end the growth rate is assumed as a function of Reynolds number $\sigma = \sigma(Re)$. Suppose we already computed the eigenvalues for at least two Reynold numbers in the

neighbourhood of the neutral curve for a certain wave-number k , a new Reynolds number can be computed by secant method as

$$\text{Re}^{n+1} = \text{Re}^n - \sigma_{max}(\text{Re}^n) \frac{\text{Re}^n - \text{Re}^{n-1}}{\sigma_{max}(\text{Re}^n) - \sigma_{max}(\text{Re}^{n-1})} \quad (3.28)$$

The method depicts the Newton method with respect to convergence. The only requirement is to know the function values $\sigma_{max}(\text{Re})$ at two points $\text{Re}^n, \text{Re}^{n-1}$ to start the iteration. The iteration is stopped as soon as the variation of Re is smaller than some tolerance ϵ_{Re} for two consecutive steps i.e

$$|\text{Re}^{n+1} - \text{Re}^n| < \epsilon_{\text{Re}}. \quad (3.29)$$

3.2.4 Resolving Wave-Number

The secant method will yield the neutral Reynolds number for a specific wave-number k . One way to get the critical Reynolds number Re_c for a specific geometry is to repeat the process of finding Re_n for a number of wave-numbers k and then take the minimum of the curve $\text{Re}_n(k)$. However the wave-number will still be a discrete quantity and the approximation will be very rough. To fully resolve the wave-number an optimization problem is imposed on the overall process. To this end the Re_n is taken as a quadratic function of k , such that $\text{Re}_n(k) = ak_n^2 + bk + c$ with some arbitrary constants a, b, c . The quadratic interpolation needs at least three points initially to calculate the constants and start the iterative process. The new wave-number k_{new} and neutral Reynolds number Re_n^{new} can be estimated as

$$\begin{aligned} k_{new} &= -\frac{b}{2a}, \\ \text{Re}_n^{new} &= ak_{new}^2 + bk_{new} + c. \end{aligned} \quad (3.30)$$

The new guess for the wave number k_{new} shall now replace one of the old guesses depending on its value. The process of finding Re_n is repeated for this new k in an iterative manner using the new guess of Re as initial guess. The iteration

process is stopped as soon as the variation of the k is sufficiently small i.e.

$$|k_{new} - k_{old}| < \epsilon_k. \quad (3.31)$$

The above process will deliver the critical parameters (Re_c, k_c) for a specified geometry. The process may also converge to the maxima without any check. The main check with such a quadratic approximation is the value of the quadratic constant a , which for a minimum shall be greater than zero.

Triangulation

Although we derived all the element equations in this chapter for a Taylor-Hood triangular element, nothing has been said on the process of grid generation or triangulation until now. An iso-parametric grid can be implemented for the triangular cavity by meshing the boundaries with an equal number of nodes and joining the corresponding nodes on the boundaries with lines parallel to the boundaries to get triangular elements exactly of the shape of the cavity. Similarly domains of other simple shape such as rectangles and polygons could be initially divided into coarse triangles and then meshed. However if the main triangular domain is skewed the property will be inherited to each triangle and as such may give rise to numerical difficulties. A second drawback of the approach is the difficulty to stretch the grid at certain points where needed. An alternative is to use the available software's for mesh generation such as "Triangle" [Shewchuk \[1996\]](#), "Gmsh" [Geuzaine and Remacle \[2003\]](#), "NETGEN" [Schöberl \[1997\]](#). In the present study we use iso-parametric grids as well as "Gmsh" because of its fine integration with the programming language "C++" and ease of use. For more details about the software the reader is referred to [Geuzaine and Remacle \[2003\]](#). To have an idea about the mesh a very coarse mesh generated by the iso-parametric approach and by "Gmsh" is presented in figure 3.2 for an isosceles right-angled triangular cavity. For iso-parametric grid each of the boundaries was meshed with equal number $n = 5$ nodes, whereas the mesh generated by "Gmsh" was controlled by maximum length of any side of the resulting element $l_c = 0.25$. The mid-side nodes of elements are not shown in 3.2. It should be noted that these meshes

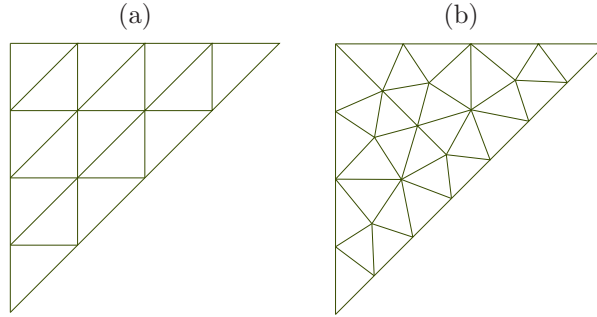


Figure 3.2: Triangular meshes (a) iso-parametric mesh, (b) mesh from "Gmsh"

are meant to just have an idea of the resulting elements and will not be used for computation as they are very coarse.

3.3 Solution Strategies

The numerical methods described in the previous sections will give accurate solution if the initial guesses used are in the neighbourhood of the critical or neutral parameters. The natural questions which arises are

- What shall be the initial guess for Re_n to be used for the given physical conditions?
- What shall be the initial guess for k_c to be used for the given physical conditions?

It is the aim of this section to somehow answer the above questions with an example at the end. Suppose we don't have any idea of the critical parameters, then one could start in the following way to get a rough idea of the values of critical parameters.

1. start with a low Re and define a moderate step size δRe in Re and initialize a step counter $i = 1$
2. Calculate the basic state for Re .
3. define a coarse step-size in k equal to δk and maximum number of steps n_k in k so that $n_k \delta k$ covers the range of physical wave-numbers.

4. repeat for $j = 1$ to n_k

$$k = j \cdot \delta k$$

Compute the eigenvalues q_m through Krylov subspace iteration and the Arnoldi algorithm.

Optionally compute the transformed eigenvalues η_m through Krylov subspace iteration and Arnoldi algorithm using the eigenvalues from the previous step.

Store the eigenvalue with largest real part q_j^{max} in a vector *eig* i.e $eig_j = q_j^{max}$.

5 If any entry in vector *eig* is sufficiently small or greater than zero stop iteration.

6 $Re = Re + \delta Re$

$$i = i + 1$$

Resume iteration from step 2.

From the above process we will get the eigenvalues with the largest real parts at discrete wave-numbers for different Reynolds numbers. From the data obtained the critical wave-number k_c and Reynolds number can be roughly estimated as the points where maximum growth rate occurs. Once we have a guess of the critical parameters they can be used for the full computational process as initial guesses. The full algorithm is stated as

1. start with initial guess for Re, k , define a moderate step-size δRe and a fine step-size δk in Re and k respectively, initialize counters $i=1, j=1$.
2. Calculate the basic state for Re .
- 3a. Compute the eigenvalues q_m through Krylov subspace iteration and the Arnoldi algorithm using the computed basic state.
- 3b. Optionally compute the transformed eigenvalues η_m through Krylov subspace iteration and the Arnoldi algorithm using the eigenvalues from the previous step.

4. $eig_i = q_i^{max}$ where q_i^{max} is the eigenvalue with largest real part.
5. if $i < 2$
 - Re = Re + δ Re
 - $i = i + 1$
 - Resume iteration at step 2.
6. Apply the secant method to compute a new Re
7. If the convergence criterion of the secant method is not fulfilled resume iteration at step 2.
8. if $j < 3$
 - $k = k + \delta k$
 - $j = j + 1$
 - $i = 1$
 - Resume the iteration at step 2.
9. Apply the quadratic optimization to compute a new Re and k
10. If convergence criterion of optimization is fulfilled stop iteration the Re and k are the critical parameters, otherwise reset the counter $i = 1$ and resume the iteration from step 2.

The above algorithm will deliver the critical parameters. However if we are interested in getting neutral curve the last two steps may be omitted. The quadratic optimization is used because it can be implemented easily, however it could also be replaced by some higher order scheme.

3.3.1 An Example

As an example let us consider an isosceles right-angled triangular cavity of unit aspect ratio. We want to determine the critical parameters for this cavity when the lid moves away from the right angle. Applying the first algorithm with an

Table 3.1: Output of the full algorithm for the isosceles cavity

Iteration	Re_n	k_n	σ
1	540.403311	2.800000	$-7.643836e - 12$
2	540.198052	2.900000	$6.852125e - 12$
3	541.940419	3.000000	$-5.999636e - 11$
4	540.048332	2.860539	$-1.372007e - 10$

initial Reynolds number of 100 and step-sizes of 100 in Re , and 0.25 in k , and keeping the range of $k = 0 - 10$ will need $n_k = 40$. The resulting growth rates at different wave-numbers k for different Re are shown graphically in figure 3.3. From these results it can be seen that the critical parameters lie in the range

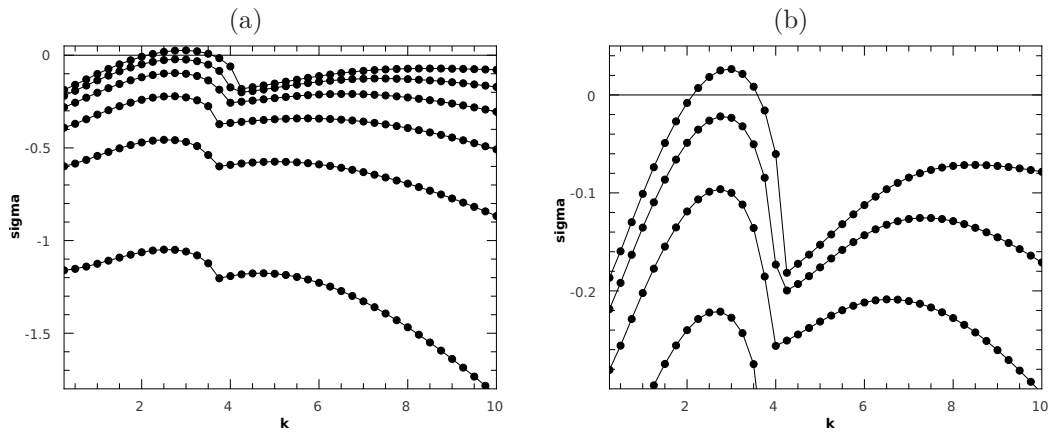


Figure 3.3: Growth-rates for the isosceles cavity (a) $Re \in [100 - 600]$, lowest curve corresponds to $Re = 100$ and increasing in steps of 100 for upper curves, (b) Zoom of (a) with the lowest curve representing $Re = 300$ and the upper most $Re = 600$ in steps of 100.

$[500 - 600]$ for Re and $2.75 - 3.25$ for k . Also note a discontinuity in all the curves near $k = 3.75 - 4.25$ which represent a change of mode.

These values can be used as initial guess for the full algorithm to determine the the critical parameters. Taking the initial guesses as $Re = 550$, $k = 2.8$, $\delta Re = 25$, and $\delta k = 0.2$ for the full algorithm yields the critical parameters for this geometry as $(Re_c, k_c) = (540.048, 2.860)$ with a tolerance limit of 0.0001 in k . The neutral Reynolds number Re_n computed during each iteration at different k is represented in table 3.1. The quadratic interpolation converged to the critical

3. Numerical Methods

values in only one iteration. Once the critical parameters are evaluated for a certain geometry, they can be used as initial guess for a slightly varied geometry.

Chapter 4

Validation of the Numerical Code

In order to validate the numerical code, results must be compared with those available in the literature. A comparison of results for the steady-state two-dimensional basic flow with some of the available data will be carried out in section 4.1. Results from the stability analysis will be compared with some of the available data in section 4.2.

4.1 Validation of Basic State

As a first verification of the basic state we consider an isosceles right-angled triangular cavity at different Re . The values of the stream function and vorticity at the center of the primary eddy along with its position are compared to the results of [Erturk and Gokcol \[2007\]](#), for the motion of the lid directed away from the right-angled corner. It shall be noted that [Erturk and Gokcol \[2007\]](#) used the stream function-vorticity formulation with a coordinate transformation to solve the problem in contrast to present finite-element approach. The data tabulated in table 4.1 show good agreement with a maximum deviation of less than the 1.03%. The grid used for the present results in table 4.1 consists of 29161 quadratic velocity nodes, and 7381 linear pressure nodes in a total of 14400 iso-parametric triangular elements. For a qualitative comparison of the overall flow, streamlines of basic two-dimensional flows for various Re are shown in figure 4.1, where the results of [Erturk and Gokcol \[2007\]](#) are also reproduced. An excellent agreement

Table 4.1: Stream function (ψ_C) and vorticity (ϖ_C) at the center (x_C, y_C) of the primary vortex. The data in parentheses are taken from [Erturk and Gokcol \[2007\]](#).

Re	$-\psi_C$	$-\varpi_C$	x_C	y_C
100	0.06452 (0.06451)	5.02972 (5.01902)	0.4472 (0.4473)	0.8520 (0.8516)
500	0.06072 (0.06065)	5.75854 (5.73737)	0.5486 (0.5469)	0.8482 (0.8496)
1000	0.05325 (0.05306)	6.99701 (7.02235)	0.6081 (0.6094)	0.8678 (0.8691)
1500	0.04795 (0.04765)	8.15992 (8.20570)	0.6554 (0.6582)	0.8852 (0.8848)
2000	0.04396 (0.04353)	9.23088 (9.32624)	0.6931 (0.6953)	0.8946 (0.8965)

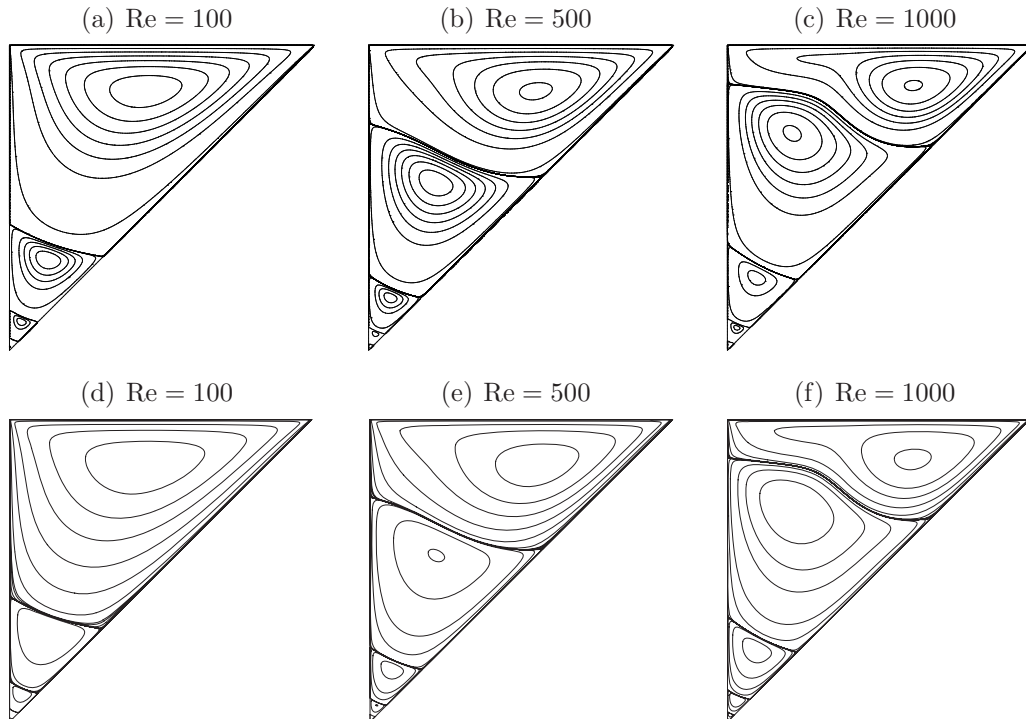


Figure 4.1: Streamlines of the basic flow at various Re, the lid moves away from the right angle. Results of [Erturk and Gokcol \[2007\]](#) are reproduced here in the lower row (d), (e) and (f).

between the profiles can be observed for different Re in figure 4.1.

A comparison between streak lines of experimental results of [Kühnen \[2006\]](#) for an isosceles right-angled triangular cavity with the present numerical results are shown in figure 4.2. The cavity used in the experiment has a finite size

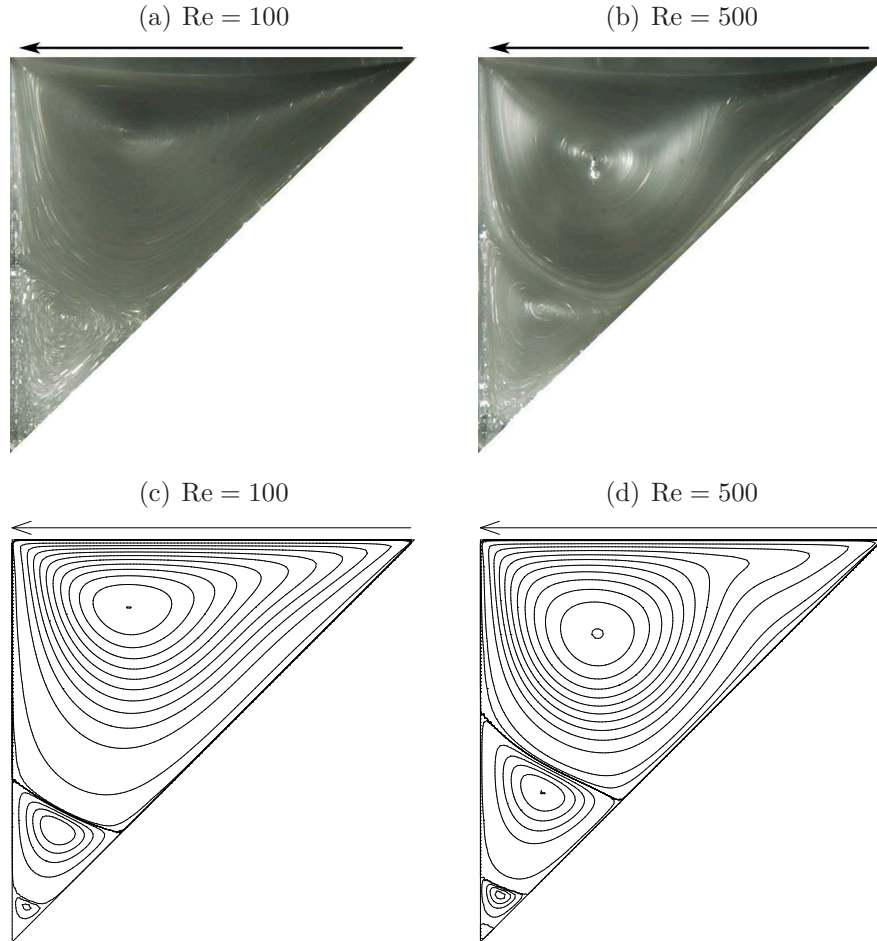


Figure 4.2: Wall motion towards the rectangular corner. The photographs show streak lines in the (x, y) -plane at $z = -1$ for $\text{Re} = 100$ (a) and $\text{Re} = 500$ (b). The numerically computed contours of the stream function are shown in (c,d).

in the z -direction with a span-wise aspect ratio of $\lambda = 10.85$, and the lid was a circular cylinder of radius $R = 3.375 \Gamma$. As can be seen the numerically computed streamlines agree satisfactorily to the experimental results with the exception that only two of the vortices are clearly visible in the experiment. In-fact the strength of the tertiary and subsequent eddies from the numerical results are of order 10^{-7} , and therefore may not be prominently visible in the experiment.

To check the influence of grid resolution computations were made on different grids, with the resolution of the grids controlled by a parameter l_c , such that

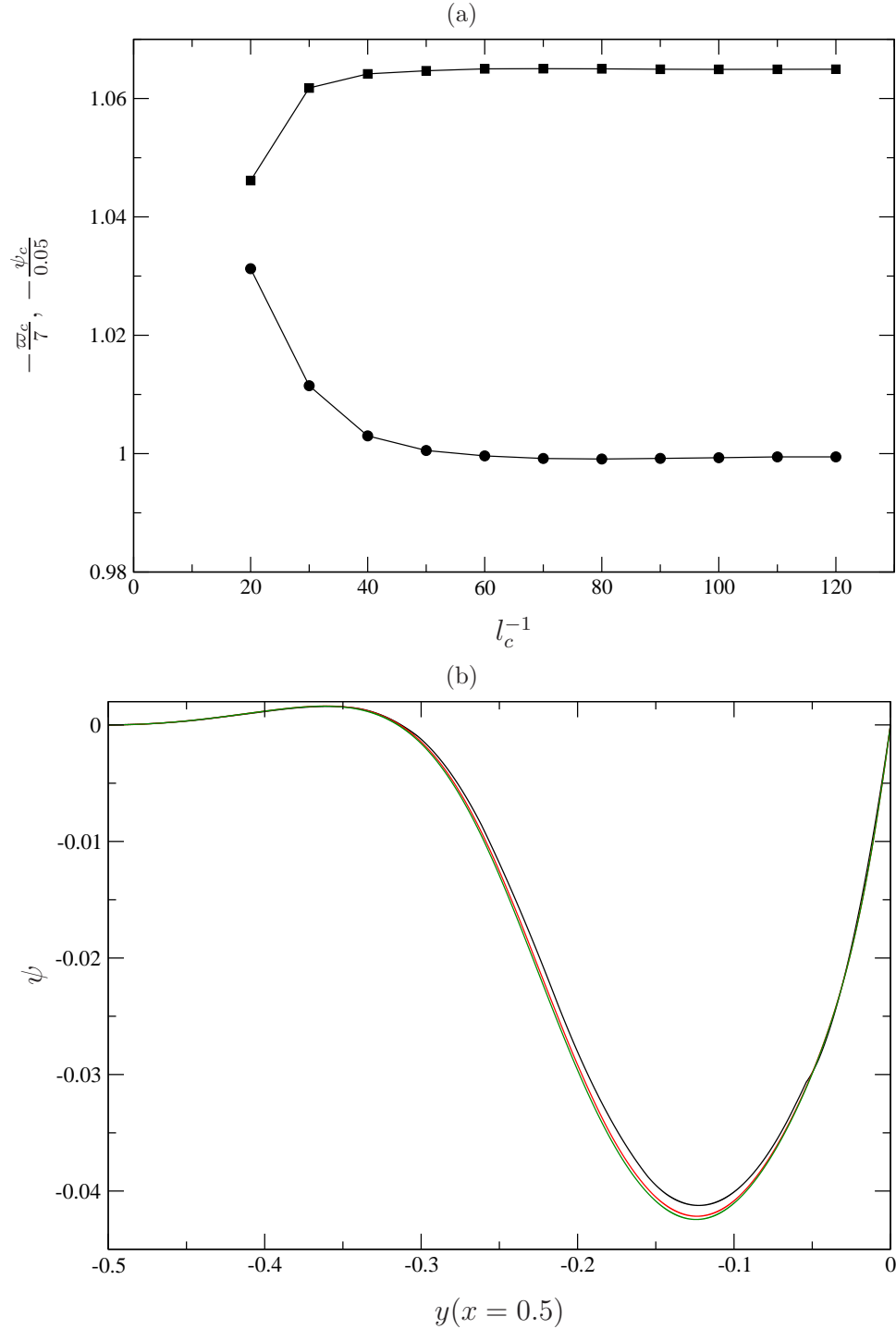


Figure 4.3: Grid convergence check for an isosceles right-angled triangular cavity with lid moving away from rectangular corner and $\text{Re} = 1000$. (a) at center of primary eddy value of stream function ψ_c (squares) and vorticity ϖ_c (circles) as a function of grid parameter l_c^{-1} , (b) stream function ψ shown along the line $x=0.5$, for grid parameter $l_c = \frac{1}{20}$ (black), $l_c = \frac{1}{40}$ (red) and $l_c = \frac{1}{120}$ (green).

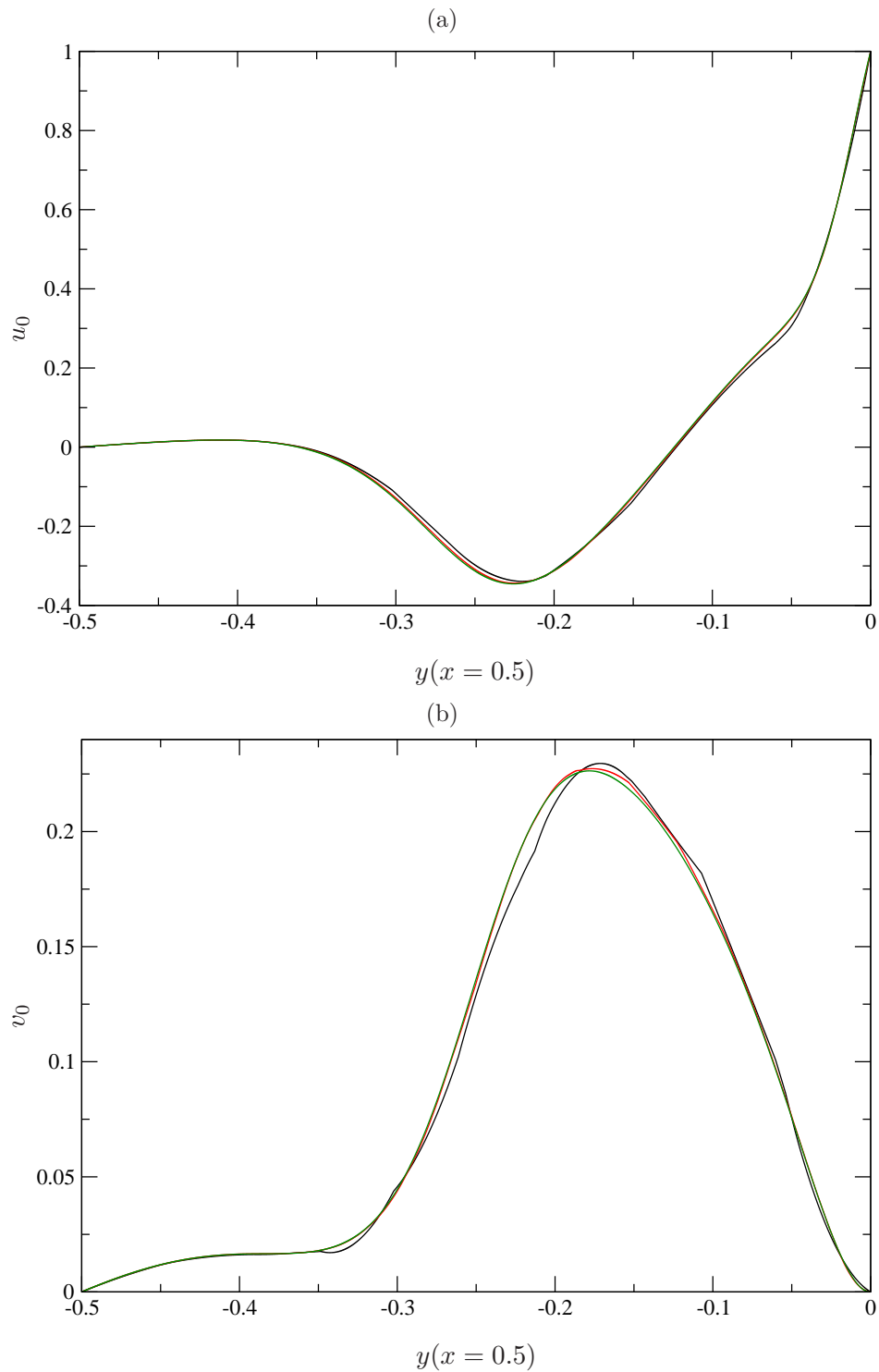


Figure 4.4: Grid convergence check for an isosceles right-angled triangular cavity with lid moving away from rectangular corner and $\text{Re} = 1000$. (a) x -velocity u_0 , (b) y -velocity v_0 are shown along the line $x=0.5$, for grid parameter $l_c = \frac{1}{20}$ (black), $l_c = \frac{1}{40}$ (red) and $l_c = \frac{1}{120}$ (green).

Γ	Re_c	k_c	$\pm\omega_c$
0.25	1149.9 (1152.7)	20.69 (20.63)	2614.1 (2619.6)
0.50	703.74 (706.1)	10.63 (10.63)	818.0 (819.9)
0.75	647.62 (650.6)	7.262 (7.258)	480.9 (482.1)
1.00	784.22 (786.3)	15.44 (15.43)	0.000 (0.000)
1.20	726.58 (730.4)	6.692 (6.680)	350.3 (350.1)
1.50	485.97 (490.4)	1.754 (1.750)	0.000 (0.000)
2.00	442.28 (446.3)	1.720 (1.715)	0.000 (0.000)

Table 4.2: Results for the rectangular cavity of different aspect ratios data in parentheses are from [Albensoeder et al. \[2001\]](#).

none of the edges of any of the resulting triangular elements is greater than l_c . Results are shown in figures 4.3 and 4.4. It can be seen from figure 4.3(a) that the stream function and vorticity at center of the primary eddy reach the asymptote at $l_c \approx \frac{1}{70}$. Similarly there is only a minor difference between the results for stream function, and the velocities, along a line $x = 0.5$ for $l_c = \frac{1}{40}$ and $l_c = \frac{1}{120}$. In-fact the respective curves of data for $l_c = \frac{1}{120}$ almost exactly overlap the curves for $l_c = \frac{1}{60}$ (not shown for clarity). It can be stated that the solution is well converged for the $l_c \leq \frac{1}{70}$ for the basic state. However if the geometry or Re is changed this resolution may not be enough and as such the resolution shall be checked again. For the present study such checks were performed randomly for different shapes and Re to be sure that the basic state calculated was well converged with respect to the grid resolution. Another point to be mentioned is that all the computations were performed in the present study with $l_c \leq \frac{1}{110}$.

4.2 Validation Linear Stability Analysis

To verify the results from the linear stability analysis comparison with the critical data of [Albensoeder et al. \[2001\]](#) for rectangular one-sided lid-driven cavity flow is shown in table 4.2. The grid controlling parameter used for the tabulated data was $l_c = \frac{1}{100}$ whereas the number of Krylov subspaces employed were $m = 100$. It can be seen that the critical data for different aspect ratios Γ are in excellent agreement, despite of the difference in the numerical methods employed and the

4. Validation

Γ	<i>Ref</i>	$\text{Re}(d/a)^{1/2}$	α
0.75	Present Result	49.52	3.14
	Roberts [1960]	49.52	3.14
	Sparrow et al. [1964]	49.53	3.14
0.5	Present Result	68.17	3.16
	Roberts [1960]	68.19	3.16
	Sparrow et al. [1964]	68.19	3.16
	Walowit et al. [1964]	68.18	3.16

Table 4.3: Critical values of $\text{Re}(d/a)^{1/2}$ and dimensional wave number $\alpha = 2\pi d/\lambda$ at aspect ratio $\Gamma = a/b$ for Taylor-Couette flow between concentric cylinder with a rotating inner cylinder of radius a and a stationary outer cylinder of radius b .

<i>Motion</i>	<i>Ref</i>	Re_c	k_c	ω_c
(a)	Present Result	540.2	2.86	0.00
	Kühnen [2006]	570 ± 20	2.89 ± 0.11	0.00
(b)	Present Result	777.9	10.3	1.14
	Kühnen [2006]	730 ± 20	11.2 ± 0.6	1.121 ± 0.05

Table 4.4: Comparison of the critical data for right-angled isosceles triangular cavity for (a) lid motion directed away from the right-angled corner (b) lid motion directed towards the right-angled corner.

overall approach used to solve the eigenvalue problem.

As a next step of verification the Taylor-Couette flow between concentric circular cylinders of indefinite length with the outer cylinder at rest, is analysed with the present numerical code. The critical data for two values of aspect ratio Γ are tabulated in table 4.3, along with results cited in the literature. It shall be noted that Γ in this type of flow is the ratio of the radii of inner cylinder a to outer cylinder b , with a gap-width of $d = b - a$ between them. The Reynolds number is defined in the same way as by Di Prima and Swinney [1985] i.e. $\text{Re} = \frac{u_t d}{\nu}$, u_t being the tangential velocity of the inner cylinder. It can be observed from table 4.3 that the critical data are in excellent agreement with those cited in literature, despite the fact that the Cartesian formulation was used for the problem in the present study.

A comparison of the critical data with the experiments of Kühnen [2006] is

l_c^{-1}	Re_n	σ
20	540.879376	$-5.187237 \times 10^{-14}$
30	539.517538	2.894572×10^{-11}
40	540.007489	$-6.194745 \times 10^{-14}$
50	540.076282	$-8.035942 \times 10^{-14}$
60	539.982469	9.241060×10^{-14}
70	540.046705	$-7.555110 \times 10^{-14}$
80	540.021811	7.127308×10^{-15}
90	540.039644	4.231025×10^{-9}
100	540.048381	4.246143×10^{-9}
110	540.045784	5.947313×10^{-10}
120	540.041487	9.842830×10^{-10}

Table 4.5: Neutral Reynolds number Re_n and growth rate σ delivered by different grids at wave number $k = 2.86$ and for subspaces used $m = 100$, resolution of grid is controlled by parameter l_c .

shown in table 4.4 for the two cases of lid motion for the isosceles right-angled triangular cavity. It can be seen that the critical data for the case of lid motion directed away from the right angled corner are in excellent agreement, whereas there is good agreement when the motion of the lid is directed towards the right-angled corner. The minor discrepancies may be due to the fact that three dimensional flow cannot be measured exactly at the onset of instability. Moreover the effects of stationary side walls of the cavity of finite size used in the experiments could not be ruled out completely.

The effect of grid resolution on the results for the neutral Reynolds number Re_n , was studied for an isosceles right-angled cavity with the lid motion directed away from the right angle while keeping a constant wave number $k = 2.86$ and number of Krylov subspaces $m = 100$. The results are tabulated in table 4.5 along with the maximum growth rate at criticality. The grid resolution is controlled by parameter l_c as was in section 4.1. The maximum deviation in Re_n is less than 0.26%. It can be observed that even for a very coarse grid $l_c^{-1} = 30$ the result for $\text{Re}_n = 539.52$ is pretty close to $\text{Re}_n = 540.04$ computed at the finer mesh with $l_c^{-1} = 120$. So, the numerical solution can be considered as converged on a grid with resolution $l_c^{-1} \geq 100$.

4. Validation

m	σ_1	σ_2	σ_3	σ_4	σ_5
20	-0.02173788	-0.4117038	-0.4925273	-0.6142544	-0.7999152
25	-0.02173788	-0.4117037	-0.4923752	-0.6130966	-0.8029302
30	-0.02173788	-0.4117037	-0.4923752	-0.6130973	-0.8029664
35	-0.02173788	-0.4117037	-0.4923752	-0.6130973	-0.8029665
40	-0.02173788	-0.4117037	-0.4923752	-0.6130973	-0.8029666
50	-0.02173788	-0.4117037	-0.4923752	-0.6130973	-0.8029665
100	-0.02173788	-0.4117037	-0.4923752	-0.6130973	-0.8029665
120	-0.02173788	-0.4117037	-0.4923752	-0.6130973	-0.8029665

Table 4.6: Effect of the number of Krylov subspaces m on the growth rate for the first five eigenvalues σ_i , $i = 1, 2, \dots, 5$ for constant wave number $k = 2.86$ and Reynolds number $\text{Re} = 500$ and same grid with $l_c^{-1} = 120$.

m	ω_4	ω_5	ω_6
20	1.639179×10^{-2}	8.355618×10^{-1}	2.517639×10^{-1}
30	1.617602×10^{-2}	8.343197×10^{-1}	2.706329×10^{-1}
35	1.617601×10^{-2}	8.343215×10^{-1}	2.708480×10^{-1}
40	1.617601×10^{-2}	8.343215×10^{-1}	2.708495×10^{-1}
50	1.617601×10^{-2}	8.343215×10^{-1}	2.708495×10^{-1}
100	1.617601×10^{-2}	8.343215×10^{-1}	2.708495×10^{-1}
120	1.617601×10^{-2}	8.343215×10^{-1}	2.708495×10^{-1}

Table 4.7: Effect of number of Krylov subspaces m on frequencies for first three complex eigenvalues ω_i , $i = 4, 5, 6$ for constant wave number $k = 2.86$, same grid with $l_c^{-1} = 120$ and $\text{Re} = 500$.

To check the effect of the number of Krylov subspaces m on the resulting eigenvalues, computations were performed for an isosceles right angled cavity by varying the number of subspaces while keeping the wave number $k = 2.86$ and Reynolds number $\text{Re} = 500$ constant on a grid with a grid controlling parameter $l_c^{-1} = 120$. The results for the growth rates of the first five eigenvalues are tabulated in table 4.6. It can be seen that the growth rate for even the fifth eigenvalue is converged at $m = 35$. Similarly the frequencies of the complex eigenvalues is converged at $m = 40$ for the sixth eigenvalue as can be seen in table 4.7. So it can be stated that $m \geq 50$ subspaces will deliver converged eigenvalues for this type of cavity.

Chapter 5

Results and Discussion

In this chapter the results will be presented and discussed. Results for the case when lid moves away from the the specified angle θ i.e. for lid motion in positive x -direction are presented in section 5.1, where as results for the reverse motion of the lid are documented in section 5.2

5.1 Lid moving in positive x -direction

In this section results for a right-angled cavity will be presented first and the variation of the results with variation of angle θ will be discussed on the basis of these results for the right-angled cavity.

5.1.1 Result for right angled cavity

An overview on the neutral Reynolds Re_n and wave numbers k_n is provided in fig. 5.1 which shows the dependence of the neutral data on the aspect ratio Γ . The critical curve is given by the envelop of all neutral Reynolds numbers $Re_n(k)$ shown. The oscillation frequencies of the non-stationary modes are shown in fig. 5.2.

Depending on the aspect ratio Γ different modes become critical. We find 5 different modes.

- Mode 1: A low frequency oscillatory mode with $0.5 < \omega_c < 1.0$ appearing

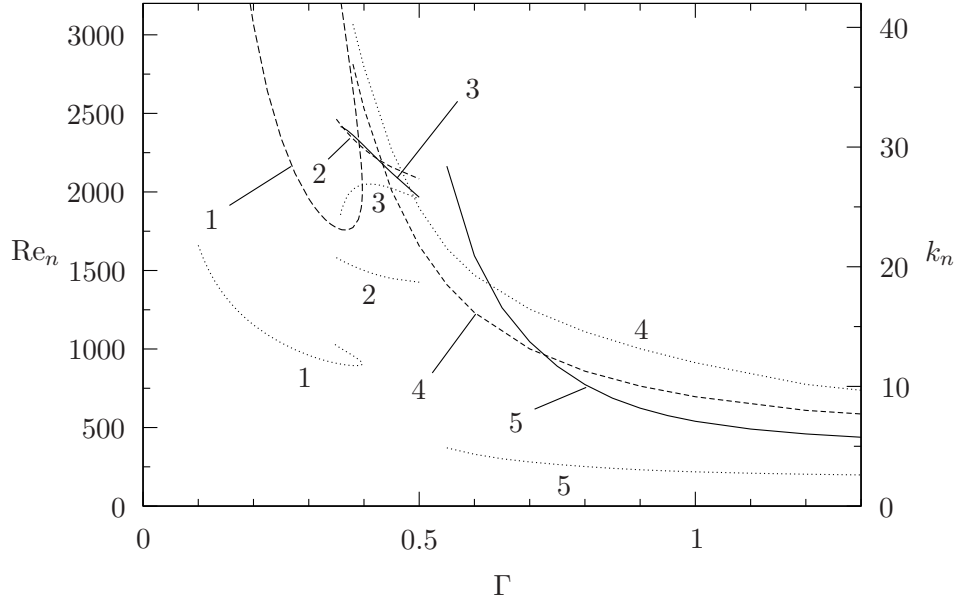


Figure 5.1: Neutral Reynolds number Re_n (solid lines: stationary modes, dashed lines: oscillatory modes) and wave number k_n (dotted lines) as functions of the aspect ratio Γ . Modes are indicated by numbers.

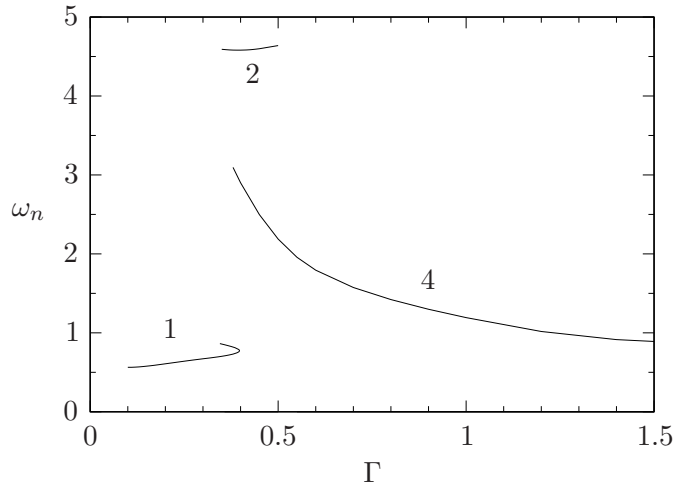


Figure 5.2: Oscillation frequency ω_n of the oscillating neutral modes as functions of aspect ratio Γ . The numbers refer to the different modes.

at an aspect ratio range of $\Gamma \leq 0.397 \pm 0.0005$ with critical wave numbers in the range of $11.7 < k_c < 15.1$,

- Mode 2: A high frequency oscillatory mode with $4.5 < \omega_c < 4.6$ appearing

at an aspect ratio range of $0.397 < \Gamma < 0.42 \pm 0.005$ with critical wave numbers in the range of $18.7 < k_c < 20.8$,

- Mode 3: A stationary mode overlaying and very close to the above oscillatory mode in the same aspect ratio range of $0.397 < \Gamma < 0.43$ and becomes critical mode in range $0.42 < \Gamma < 0.43 \pm 0.005$,
- Mode 4: A medium-frequency oscillatory mode $1.2 < \omega_c < 3.0$ appearing at an aspect ratio range of $0.43 < \Gamma < 0.75 \pm 0.005$ with critical wave numbers range of $15.0 < k_c < 30.0$,
- Mode 5: A stationary mode appearing at an aspect ratio range of $\Gamma > 0.75$ with critical wave numbers range of $k_c < 3.5$.

Two out of the five modes are stationary. Moreover, modes 2 and 3 have very close neutral Reynolds numbers. Both become critical only in a very small range of aspect ratios. In the following each of the modes will be analyzed by discussing their properties for representative aspect ratios. The energy production terms integrated over the volume and normalized with the dissipation term are given in table 5.1 for the representative cases at critical conditions. For shallow cavities (modes 1 and 2) $\int I_1 dV$ and $\int I_2 dV$ represent the dominant contributions to the energy production rates. For modes 3 and 5 $\int I_2 dV$ makes the dominant contribution to the overall energy production rate, whereas $\int I_1 dV$ is the major contributor for mode 4. In streamline coordinates the dominant energy production term is always $\int I_2' dV$.

5.1.1.1 Mode 1: $\Gamma \leq 0.397$

Mode 1 is the most dangerous mode for $\Gamma \leq 0.397$. A close-up of the neutral curve for mode 1 is shown in figure 5.3. Note that the neutral curve turns back at $\Gamma \approx 0.397$.

As an example we consider $\Gamma = 0.365$. Figure 5.4a shows the flow fields and the kinetic energy production rates at the critical point $(Re_c, k_c, \omega_c) = (1756.66, 11.8, 0.715)$. The moving lid drives a primary vortex whose center is located closed to the downstream end of the moving lid. Near the upstream end of the moving lid and next to the rigid corner made by the two stationary

5. Results and Discussion

Table 5.1: Different energy production terms integrated over volume for representative cases of different instability modes at criticality.

	$\Gamma = 0.365$	$\Gamma = 0.42$	$\Gamma = 0.425$	$\Gamma = 0.7$	$\Gamma = 1.0$
Re_c	1756.66	2220.66	2206.87	1000.71	540.20
$\int I_1 dV$	0.590	0.555	0.214	0.842	-0.040
$\int I_2 dV$	0.503	0.505	0.896	0.021	1.299
$\int I_3 dV$	-0.054	-0.043	-0.101	0.149	-0.252
$\int I_4 dV$	-0.039	-0.016	-0.010	-0.011	-0.006
$\int I'_1 dV$	-0.075	0.090	0.101	0.008	-0.062
$\int I'_2 dV$	0.703	0.705	0.785	0.686	0.913
$\int I'_3 dV$	0.032	0.002	-0.030	0.121	-0.078
$\int I'_4 dV$	0.340	0.201	0.145	0.185	0.227

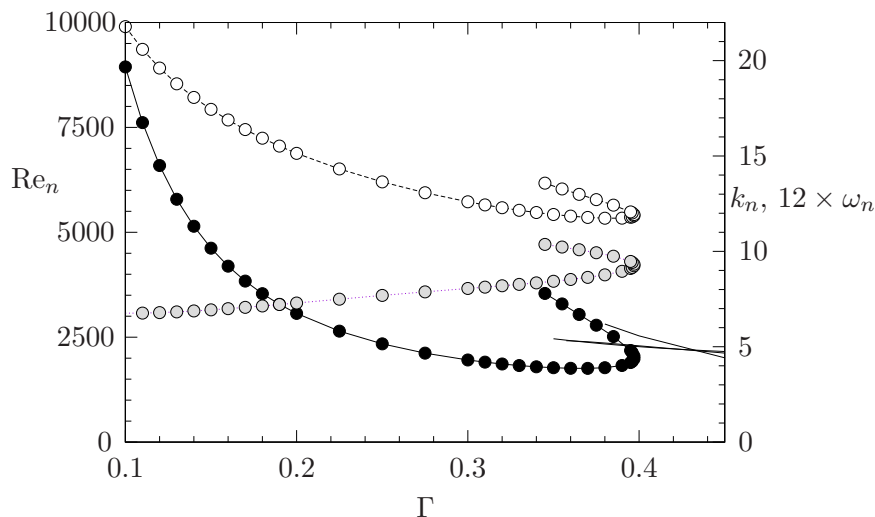


Figure 5.3: Neutral Reynolds number Re_n for mode 1 (solid line and dots), neutral wave number k_n (dashed line and circles) and neutral frequencies $12 \times \omega_n$ (dotted line and grey circles) as functions of aspect ratio Γ . Part of the neutral curves of mode 2 and 3 are visible as lines entering from the right.

walls separated secondary vortices are found which transform into a sequence of Moffatt eddies as the rigid corner is approached.

The total local energy transfer $\sum_i I_i$ has a global maximum and a weaker global minimum near the center of the primary vortex (fig. 5.4a). Likewise, the flow field of the critical mode has a large relative amplitude in the region of

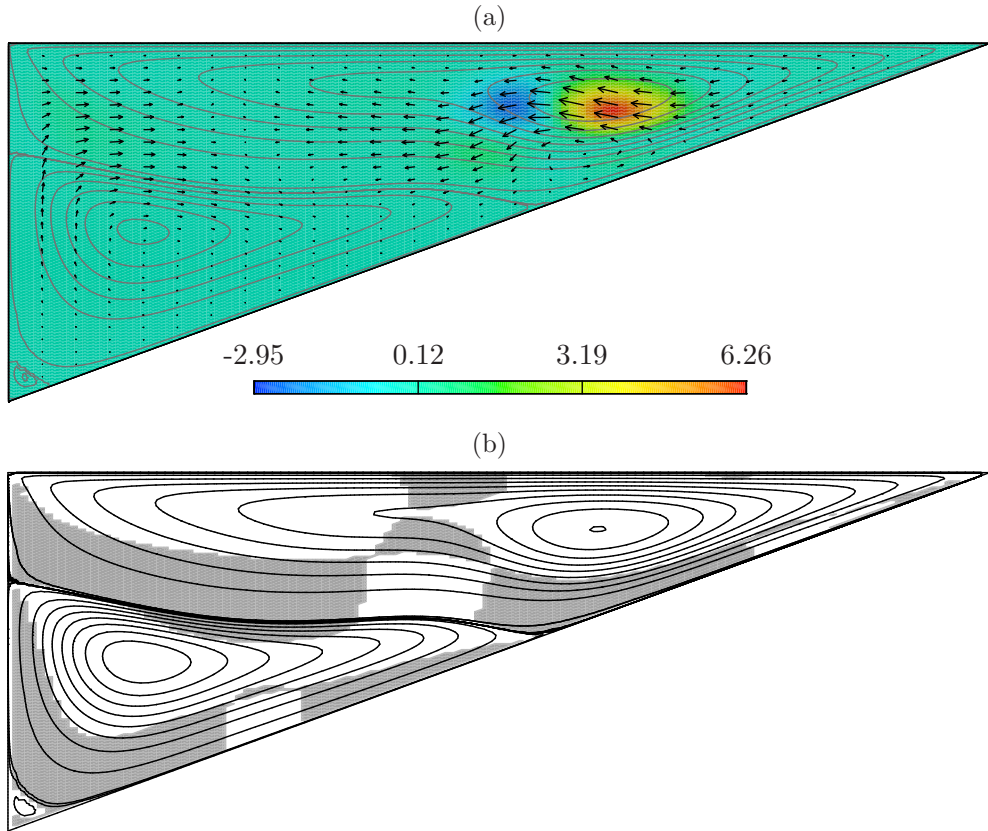


Figure 5.4: (a) Basic state streamlines at $\text{Re}_c = 1756.66$ for $\Gamma = 0.365$ (different levels of isolines are used to show the secondary and tertiary eddies) along with the critical mode (arrows) and the total local energy production rate $\sum_i I_i$ (coloured) in a plane $z = \text{const.}$ in which $\sum_i I_i$ takes its absolute maximum. (b) Basic flow overlaid with the areas in which the inviscid criterion (2.17) for a centrifugal instability holds.

the primary eddy, apart from a small region near the upstream wall where no significant energy production takes place. We conclude that the properties of the primary vortex are of key importance for the instability of mode 1. The primary vortex has an elliptic shape due to the driving mechanism and the geometric constraints. The maximum energy production is located close to the center of the strained vortex. In this region the perturbation flow is approximately aligned with the bisection of the major and the minor half axes of the nearly elliptic streamlines. These characteristics indicate an elliptic instability mechanism [Eloy

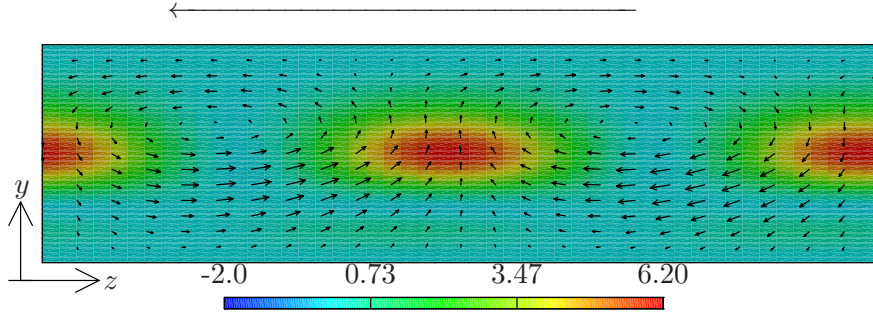


Figure 5.5: Critical mode 1 over one wavelength in z -direction for $\Gamma = 0.365$ shown at $x = 0.62$ (arrows) and total local energy production (coloured). The arrow indicates the direction of propagation of the wave.

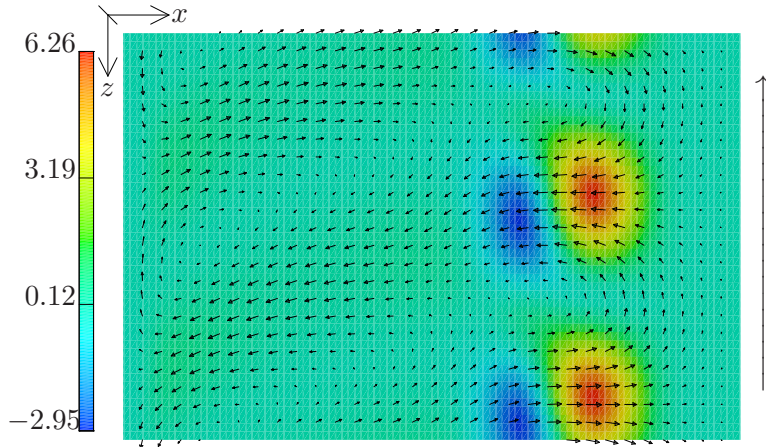


Figure 5.6: Critical mode 1 over one wavelength in z -direction for $\Gamma = 0.365$ shown at $y = -0.07$ (arrows) and total local energy production (coloured). The arrow indicates the direction of propagation of the wave.

and Le Dizès, 2001; Kerswell, 2002; Kuhlmann et al., 1998]. In fact, the evaluation of the local Rayleigh criterion (fig. 5.4b) shows that the energy transfer occurs outside of the region in which (2.17) holds. This confirms that centrifugal effects are not the cause of the instability.

The perturbation flow field for a wave propagating in the negative z -direction is shown in fig. 5.5 for a cross section at $x = 0.62$. The wavelength of the wave $\lambda = 2\pi/k = 0.534$ is comparable to the maximum depth $\Gamma = 0.365$ of the cavity. A view through the moving lid is shown in fig. 5.6 at $y = -0.07$. The absence of any mirror symmetry indicates that the mode is propagating in z direction.

5. Results and Discussion

A similar basic flow arises in shallow rectangular lid-driven cavities [Albensoeder et al., 2001]. Even though some energy transfer occurs in the center of the vortex as well, the major contribution to the energy transfer arises, via a centrifugal effect, near the bottom of the rectangular cavity. The centrifugal process is absent in the prismatic cavity with $\Gamma = 0.365$, since the fluid which separates from the bottom wall can expand into a much wider space owing to widening of the cavity in the negative x direction. This effect slows down the separated basic flow, thereby suppressing centrifugal effects.

The question arises whether or not an asymptotic limit for the critical Reynolds and wave numbers exists for $\Gamma \rightarrow 0$. In that limit, the only available length scale is the length s_2 of the stationary side wall making the right angle with the moving lid. If the flow instability would occur in the vicinity of the 90° -upstream corner of the cavity, s_2 would be the relevant length scale and an asymptotic behaviour of the critical data could be expected. However, the flow near the 90° -rectangular corner is similar to an entrance flow and it is stable [see e.g. Albensoeder et al., 2001; Laure et al., 1990]. For the rectangular cavity the instability occurs further downstream near the concentrated vortex which forms in front of the downstream stationary wall. Such a downstream wall, however, is absent in the prismatic case. Here the flow enters a wedge which becomes ever sharper for $\Gamma \rightarrow 0$. Even though we find a vortex in the downstream half of the prismatic cavity for $\Gamma = 0.365$ which is the cause of the instability, the basic flow changes in the limit $\Gamma \rightarrow 0$. Owing to the diminishing height of the cavity the basic flow will be viscously dominated as the downstream corner is approached. Hence, inertial effects near the downstream corner will be completely suppressed. Moreover, the basic flow in the bulk approaches the Couette–Poiseuille profile $\mathbf{u}_0 = U \left[3(y/\tilde{\Gamma}) + 2 \right] (y/\tilde{\Gamma}) \mathbf{e}_x$ with $\tilde{\Gamma} = \Gamma(x - 1)$ which is linearly stable. Hence, we expect a stable basic flow in the limit $\Gamma \rightarrow 0$. To check this hypothesis we apply the scaling based on s_2

$$\text{Re}^* = \Gamma \text{Re}, \quad k^* = \Gamma k, \quad \omega^* = \text{Re}^* \omega, \quad (5.1)$$

suitable for the limit considered. The correspondingly scaled critical data are shown in fig. 5.7. It can be seen that this scaling is appropriate for a certain range of intermediate small aspect ratios. However, the neutral Reynolds number

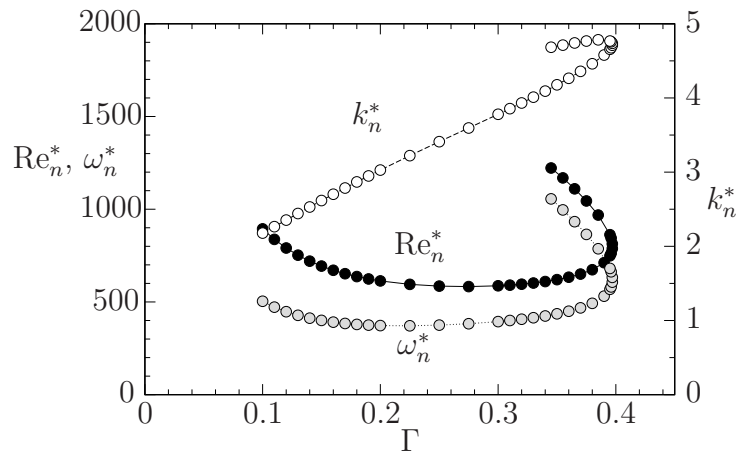


Figure 5.7: Critical data for mode 1 using the scaling (5.1) for shallow cavities.

Re_n^* for mode 1 shows a tendency to diverge as $\Gamma \rightarrow 0$ indicating a stabilization of the basic flow.

5.1.1.2 Mode 2 and 3: $0.397 < \Gamma < 0.43$

Figure 5.8 shows a close-up of the neutral curves in the aspect-ratio range $0.375 < \Gamma < 0.45$. In the range $0.397 < \Gamma < 0.43$ two distinct modes may become critical and their neutral curves are very close to each other. Mode 2 is oscillatory with the oscillation frequency of in the range $4.55 < \omega_n < 4.65$ and with a wave number in the range $19 < k_n < 20$. The other mode, mode 3, is stationary with a wave number ranging in $25 < k_n < 27$. The maximum difference between the neutral Reynolds number of the two modes is less than 20 at any Γ in the range $0.397 < \Gamma < 0.43$ considered.

As an example for the oscillatory mode 2 we consider $\Gamma = 0.42$. The critical condition are $(Re_c, k_c, \omega_c) = (2220.66, 19.37, 4.58)$. As shown in fig. 5.9 the basic flow at criticality is similar to the one at $\Gamma = 0.365$ considered above, with a primary strained vortex in the upper downstream half of the cavity and a large but weak secondary eddy in the lower left part of the cavity. The perturbation flow field is most pronounced in the region of the primary eddy. Contrary to mode 1 where the perturbation flow is essentially unidirectional across the center of the basic vortex, the perturbation flow for mode 2 is directed towards or away from the center of the vortex. The region of maximum energy production shifted

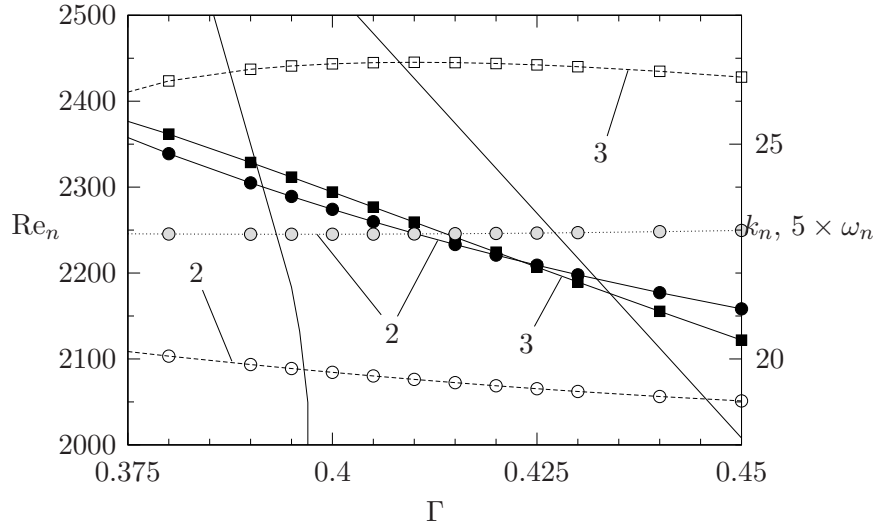


Figure 5.8: Neutral Reynolds number Re_n (solid lines and bold symbols), neutral wave numbers k_n (dotted lines and open symbols) and neutral frequencies $5 \times \omega_n$ (dotted line and grey symbols) for the oscillatory mode 2 (circles) and the stationary mode 3 (squares). The neutral curves for mode 1 and 4 are shown as lines without symbols.

slightly away from the center of the basic vortex. Yet, the energy production takes place in a region where the basic flow is expected to be stable regarding centrifugal mechanisms. This can be seen by evaluation the criterion (2.17) (not shown) which yields a very similar pattern as for $\Gamma = 0.365$ shown in fig. 5.4b. We conclude, therefore, that the instability is due to a resonance of Kelvin-waves on the concentrated vortex, similar as for $\Gamma = 0.365$, The resonance being communicated by the strain field contained in the deformed vortex [Eloy and Le Dizès, 2001; Kerswell, 2002].

Further characteristics of the critical mode 2 can be recognized from figs. 5.10 and 5.11. The latter figure shows the critical flow field in the (y, z) plane for wave propagating in the negative z -direction. The wavelength of the wave $\lambda = 2\pi/k = 0.324$ is comparable to the depth of the cavity. The different structures in the vicinity of the basic vortex of mode 2 as compare to mode 1 is evident. A particular feature of mode 2 is the plane-wave-like structure that extends upstream the moving lid in the left half of the cavity (fig. 5.10). The wave propagated away from the upstream wall. This regular wave structure may

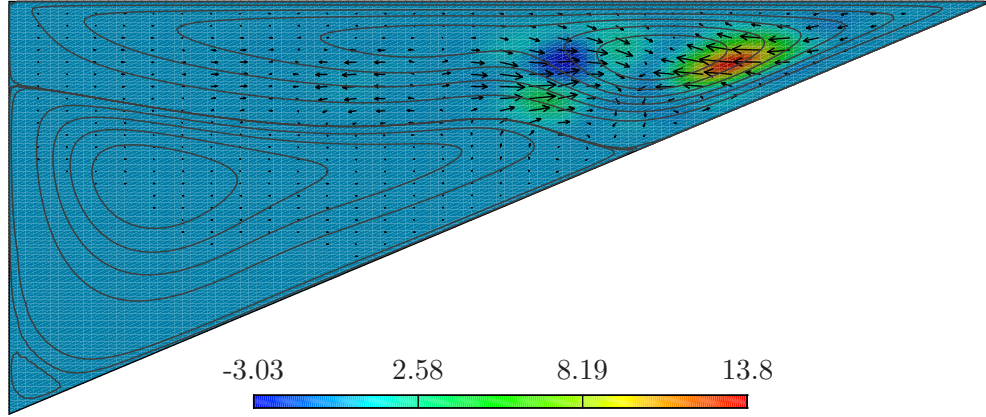


Figure 5.9: Streamlines of basic flow at $Re_c = 2220.66$ for $\Gamma = 0.42$ (different scales are used to show the secondary and tertiary eddies) along with the critical mode 2 (arrows) and the sum $\sum_i I_i$ of all local energy production rates (coloured) in a plane $z = \text{const.}$ in which $\sum_i I_i$ takes its maximum.

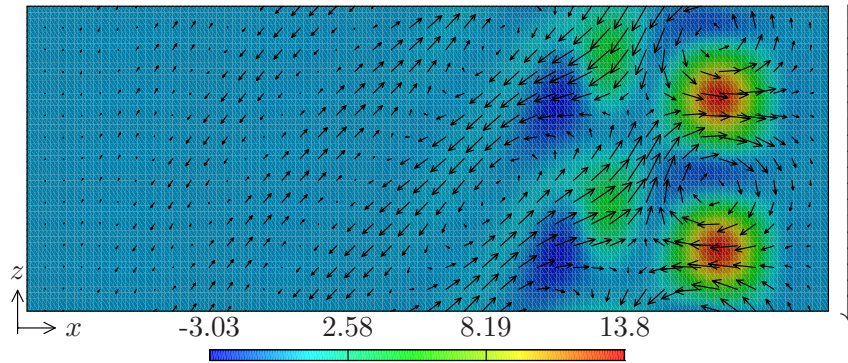


Figure 5.10: Critical mode 2 (arrows) over one wavelength in z -direction for $\Gamma = 0.42$ shown at $y = -0.062$ and total local energy production (coloured). The arrow indicates the direction of propagation of the wave.

reflect a spatial mode of the underlying entrance flow, the mode being damped in upstream direction. A similar behaviour has been found in rectangular thermocapillary cavities where the unstable hydrothermal waves existing far away from the lateral boundaries are modified by strong effects due to the primary vortex localized in front of the downstream wall [see e.g. fig. 17 of [Kuhlmann and Albensoeder, 2008](#)].

As an example for the stationary mode 3 we consider $\Gamma = 0.425$. The stream-

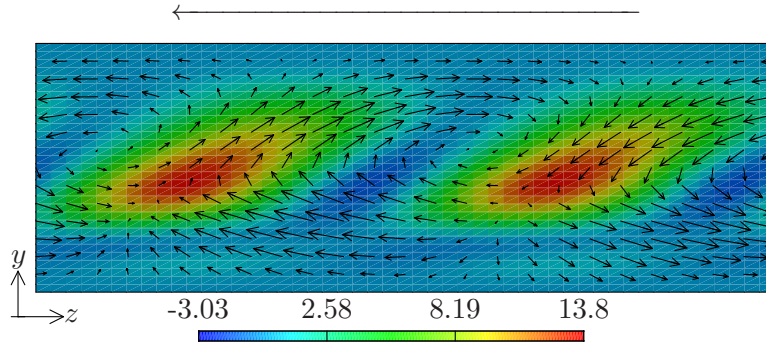


Figure 5.11: Critical mode 2 over one wavelength in z -direction for $\Gamma = 0.42$ shown at $x = 0.74$ (arrows) and total local energy production (color). The arrow indicates the direction of propagation of the wave.

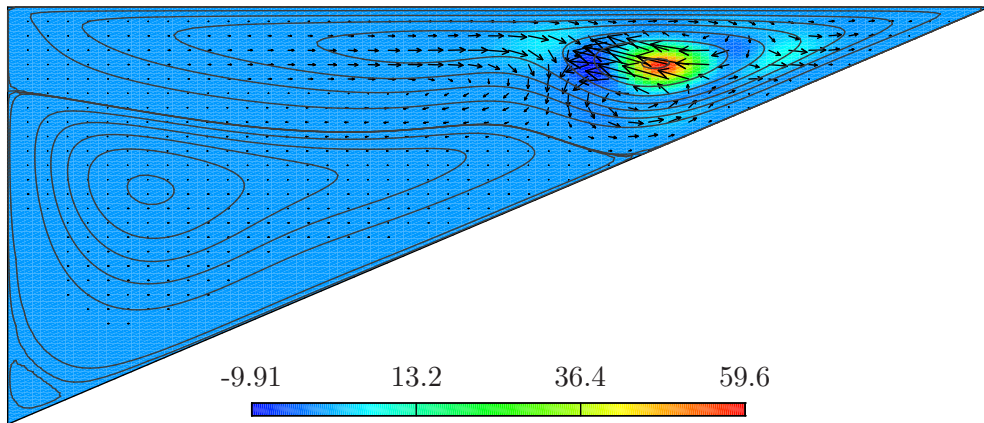


Figure 5.12: Streamlines of basic flow at $\text{Re}_c = 2206.87$ for $\Gamma = 0.425$ (different scales are used to show the secondary and tertiary eddies) along with the critical mode 3 (arrows) and the sum $\sum_i I_i$ of all local energy production rate (coloured) in a plane $z = \text{const.}$ in which $\sum_i I_i$ takes its maximum.

lines of basic steady flow along with the local energy transfer rate are shown in figure 5.12 at the critical condition $(\text{Re}_c, k_c) = (2206.87, 26.84)$. The nearly perfect coincidence of the energy production peak with the center of the vortex together with the alignment of the perturbation flow in direction of the bisection of the major and minor half axis of the elliptic streamlines of the strained vortex strongly suggest the elliptic instability mechanism. The distribution of the energy production is similar as in the two-sided lid-driven cavity [see, e.g., fig. 9 of

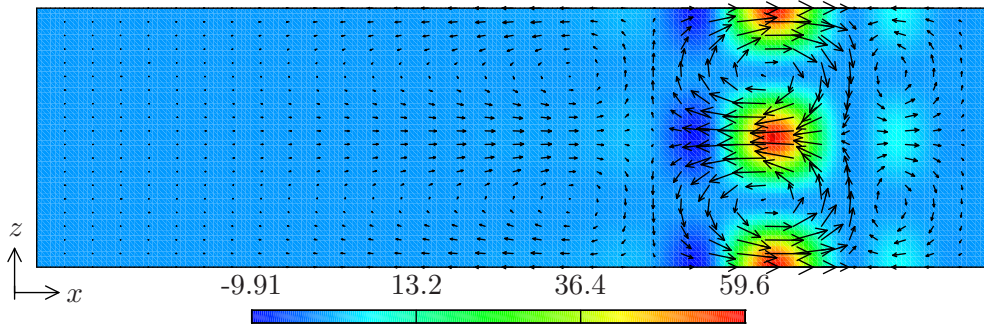


Figure 5.13: Critical mode 3 over one wavelength in z -direction for $\Gamma = 0.425$ shown at $y = -0.059$ (arrows) and total local energy production (color).

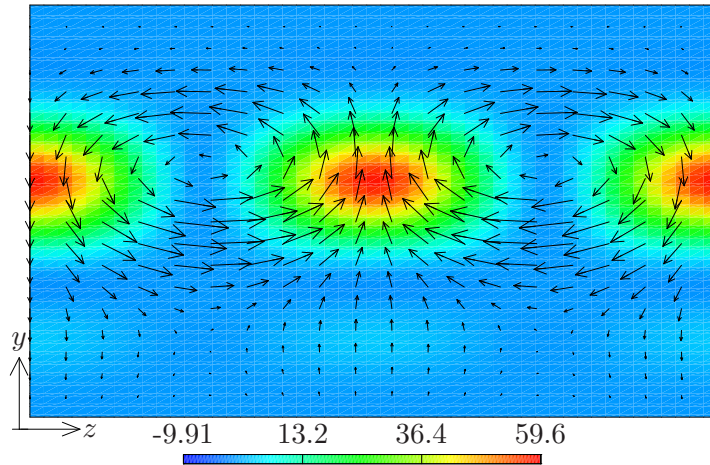


Figure 5.14: Critical mode 3 over one wavelength in z -direction for $\Gamma = 0.425$ shown at $x = 0.67$ (arrows) and total local energy production (coloured).

[Albensoeder and Kuhlmann, 2002](#)].

The structure of the critical mode in the two other orthogonal planes is shown in figs. 5.13 and 5.14. The perturbation flow is clearly restricted to the region of the basic vortex. The vortical structures of the critical mode are very similar to the elliptic instability mode that has been found in rectangular cavities with two facing lids moving in opposite directions (compare fig. 5.13 with fig. 8c of [Kuhlmann et al. \[1997\]](#) and fig. 8 of [Albensoeder and Kuhlmann \[2002\]](#)).

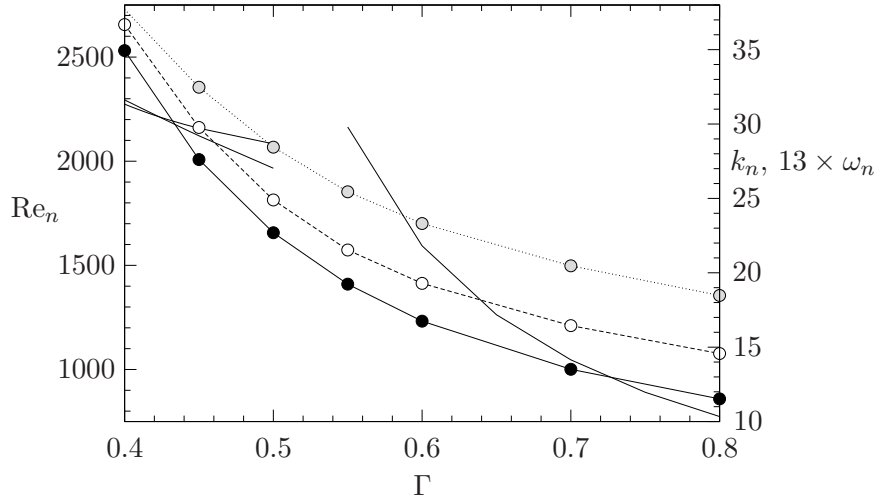


Figure 5.15: Neutral Reynolds number Re_n (solid line and dots), neutral wave number k_n (dashed line and circles) and neutral frequencies $13 \times \omega_n$ of the medium frequency mode 4 as functions of aspect ratio Γ . Part of the neutral curves for modes 2, 3 and 5 are shown as lines without symbols.

5.1.1.3 Mode 4: aspect ratios $0.43 < \Gamma < 0.73$

A close-up of the neutral curve for mode 4 is shown in fig. 5.15. Mode 4 is critical in the aspect-ratio range $0.43 < \Gamma < 0.73$. Within this range of Γ the oscillation frequency varies within $\omega_c \in [1.3, 2.5]$.

We consider the critical mode 4 for $\Gamma = 0.7$ at the critical condition $(Re_c, k_c, \omega_c) = (1000.71, 16.4, 1.572)$. Figure 5.16a shows basic-flow streamlines, the total local energy production rate, and the perturbation flow field, all in the plane $z = \text{const.}$ in which the energy production rate takes its global maximum. For mode 4 the energy production is not peaked near the center of the vortex. The region of largest energy transfer from the basic state to the critical mode is located between the center of the vortex and the point of basic-flow separation from the oblique wall. The basic-state streamlines are curved in this region and the velocity decreases radially outward from center of the vortex. Figure 5.16b shows that the region of substantial energy production is contained well inside the region in which the centrifugal instability indicator (2.17) holds. We conclude that mode 4 is due to a centrifugal instability. Apparently, the change of the instability mechanism is caused by a change of the basic flow: for aspect ratio $\Gamma = 0.7$ the basic vortex

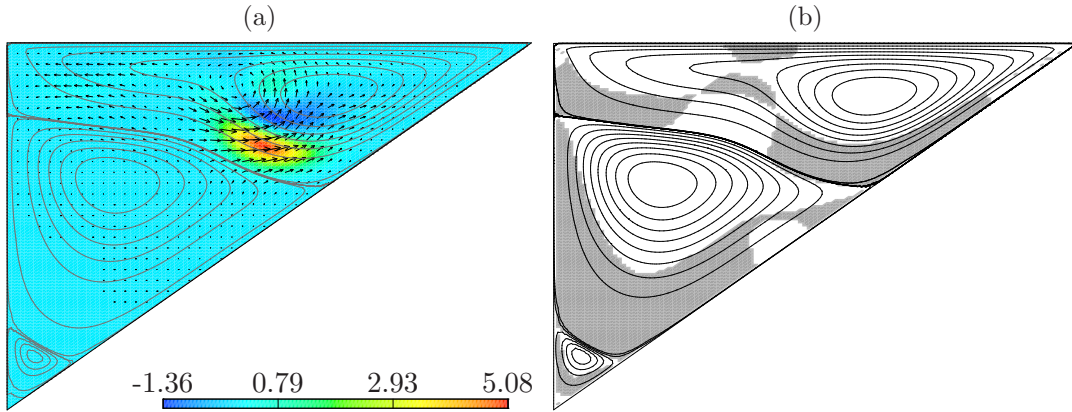


Figure 5.16: (a) Streamlines of basic flow at $Re_c = 1000.71$ for $\Gamma = 0.7$ (different scales are used to show the secondary and tertiary eddies) along with critical mode (arrows) and the total local energy production rate $\sum_i I_i$ of all (coloured) in a plane $z = \text{const.}$ in which $\sum_i I_i$ takes its global maximum. (b) Basic flow overlaid with the areas in which the inviscid criterion (2.17) for a centrifugal instability holds.

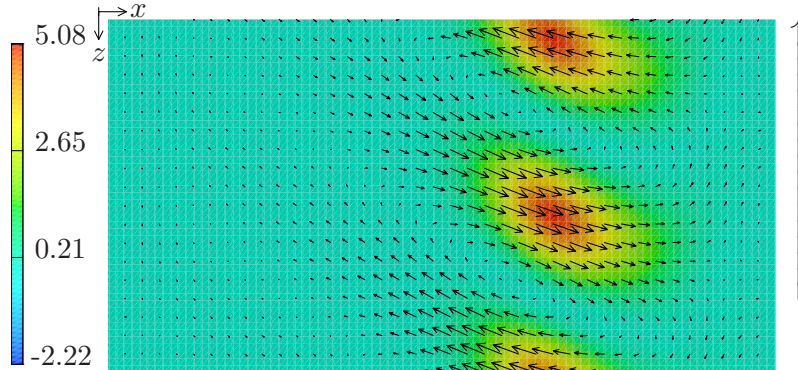


Figure 5.17: Critical mode 4 over one wavelength in z -direction for $\Gamma = 0.7$ shown at $y = -0.193$ (arrows) and total local energy production (coloured). The arrow indicates the direction of propagation of the wave.

experiences less strain as compared to those for smaller aspect ratios for which the wedge is sharper. Hence, the elliptic instability mechanism should not be as effective. Moreover, the basic vortex is more intense and the outer streamlines of the basic vortex near the separation point experience a larger curvature.

The perturbation velocity field in the (x, z) -plane for wave propagating in

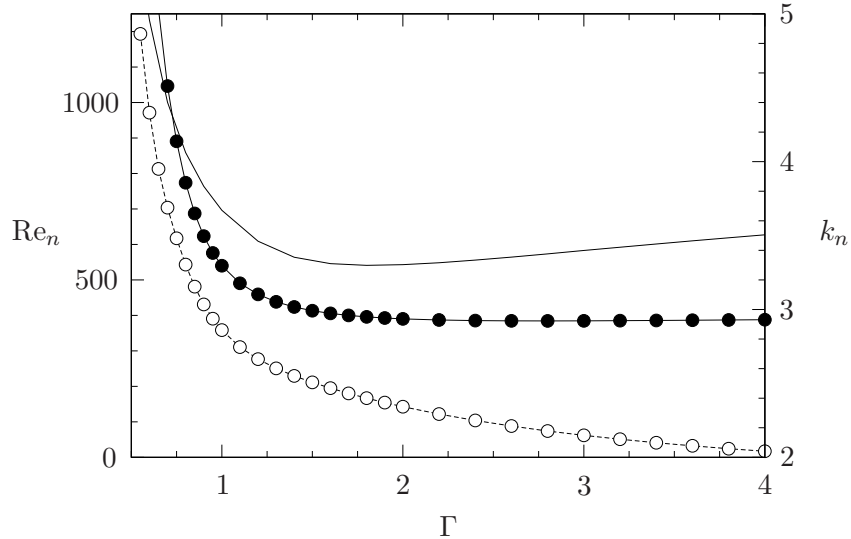


Figure 5.18: Neutral Reynolds number Re_n (solid line and dots) and neutral wave number k_n (dashed line and circles) of the stationary mode 5 as functions of aspect ratio Γ . The neutral curve for mode 4 is shown as a line without symbols.

negative z -direction is shown in fig. 5.17 over one period. The wavelength $\lambda = 2\pi/k = 0.383$ is relatively short in comparison to the depth of the cavity. A slightly supercritical flow could be visualized as a spiral wave propagating in z -direction along the basic vortex. A similar centrifugal mode also arises in the classical rectangular lid-driven cavity [Albensoeder et al., 2001], however, the location of energy production near the outer streamlines of the basic vortex differs.

5.1.1.4 Mode 5: aspect ratio $\Gamma > 0.73$

The neutral curve $Re_n(\Gamma)$ and $k_n(\Gamma)$ for the stationary mode 5 are shown in fig. 5.18. As an example we consider $\Gamma = 1$. Basic flow, neutral mode and the total local energy production are shown in fig. 5.19 in a plane in which the local energy production takes its global maximum. For $\Gamma = 1$ the basic vortex is even less strained as for $\Gamma = 0.7$. The location of maximum energy transfer is arises in a similar region as for mode 4, namely near the separation point and slightly upstream of it. Also the structure of both critical modes in the cross sections $z = \text{const.}$ shown in figs. 5.19a and 5.16a are similar. For that reason and by

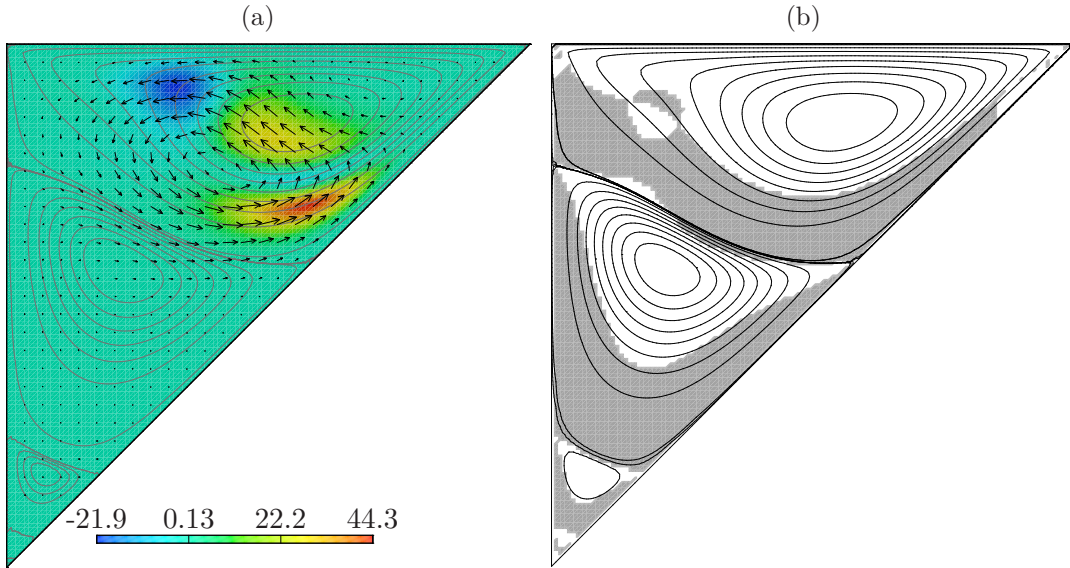


Figure 5.19: (a) Streamlines of basic flow at $Re_c = 540.2$ for $\Gamma = 1.0$ (different scales are used to show the secondary and tertiary eddies) along with critical mode (arrows) and the $\sum_i I_i$ of the total local energy production rate (color) in a plane $z = \text{const.}$ in which $\sum_i I_i$ takes its global maximum. (b) Basic flow overlaid with the areas in which the inviscid criterion (2.17) for a centrifugal instability holds.

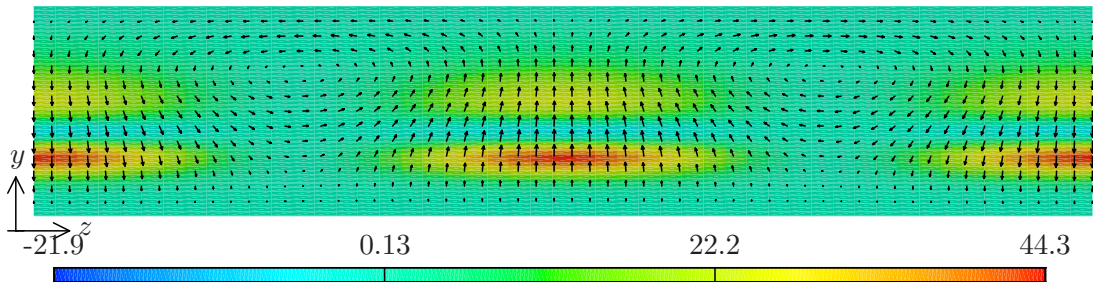


Figure 5.20: Critical mode 5 over one wavelength in z -direction for $\Gamma = 1.0$ shown at $x = 0.57$ (arrows) and total local energy production (color).

comparison of figs. 5.19a and b we conclude that the instability mechanism of mode 5 is as well of centrifugal nature. However, a second region of weak energy transfer can be identified in the center of the slightly stained basic vortex, an effect which contributes to the destabilization of this mode 5.

The perturbation velocity field at critical conditions in the (y, z) -plane is shown in fig. 5.20. The perturbation flow in this plane consists of co-rotating

vortices. The vortices superimposed to the basic flow would result in a supercritical flow in form of a basic vortex which is periodically displaced towards and away from the moving lid.

A similar critical mode is also found deep rectangular cavities [see e.g. figs. 20 and 21 of [Albensoeder et al., 2001](#)]. In fact, the asymptotic limit for $\Gamma \rightarrow \infty$ should be the same for both systems, the rectangular and the prismatic cavity. We find indications that the critical Reynolds number for mode 5 tends to an asymptotic value. While $\text{Re}_c(\Gamma)$ does not seem to vary much any-more for $\Gamma \gtrsim 2$, the critical wave number is still decreasing even beyond $\Gamma = 4$ (see fig. 5.18). For the largest aspect ratio $\Gamma = 4$ considered we get $(\text{Re}_c, k_c) = (387.9, 2.04)$. This must be compared with $(\text{Re}_c, k_c) = (420.3, 1.68) \approx (\text{Re}_c^\infty, k_c^\infty)$ which has been obtained for the rectangular cavity for $\Gamma = 4$ [[Albensoeder et al., 2001](#)]. In the rectangular cavity these values are already very close to the asymptotic limit $\Gamma \rightarrow \infty$. The slower convergence in the present prismatic case is attributed to the fact that even for $\Gamma = 4$ and larger the slope of the oblique rigid wall still has a sizeable effect on the primary lid-driven vortex, whereas such an effect is absent in the rectangular cavity. The oblique wall reduces the width in x -direction available for the basic vortex. Assuming a square vortex this width reduction would be on average $(\Gamma + 1)^{-1}/2$. For $\Gamma = 4$ this amounts to 0.1. These 10% roughly correspond to the relative difference in the two Reynolds numbers of 8% for $\Gamma = 4$.

5.1.2 Variations of results with angle θ

Variation of the angle would change the constraints on the basic flow in terms of boundary conditions and the properties of the primary eddy will change in response to these constraints. The perturbation modes may also change in response to this change in the properties of the basic flow. Variation of the modes with a decrease in angle θ from 90° for $\Gamma \leq 1.2$ is shown in figure 5.21. Neutral curves for all the modes occupy region of higher Re as θ decreases. Mode 3 takes the lead for being a neutral curve from other modes (mode 1 and mode 2) as θ decreases for small aspect ratios Γ , as is obvious from the neutral curves for $\theta = 45^\circ, 30^\circ$, and 15° . At $\theta = 15^\circ$ mode 3 is the most dangerous mode of

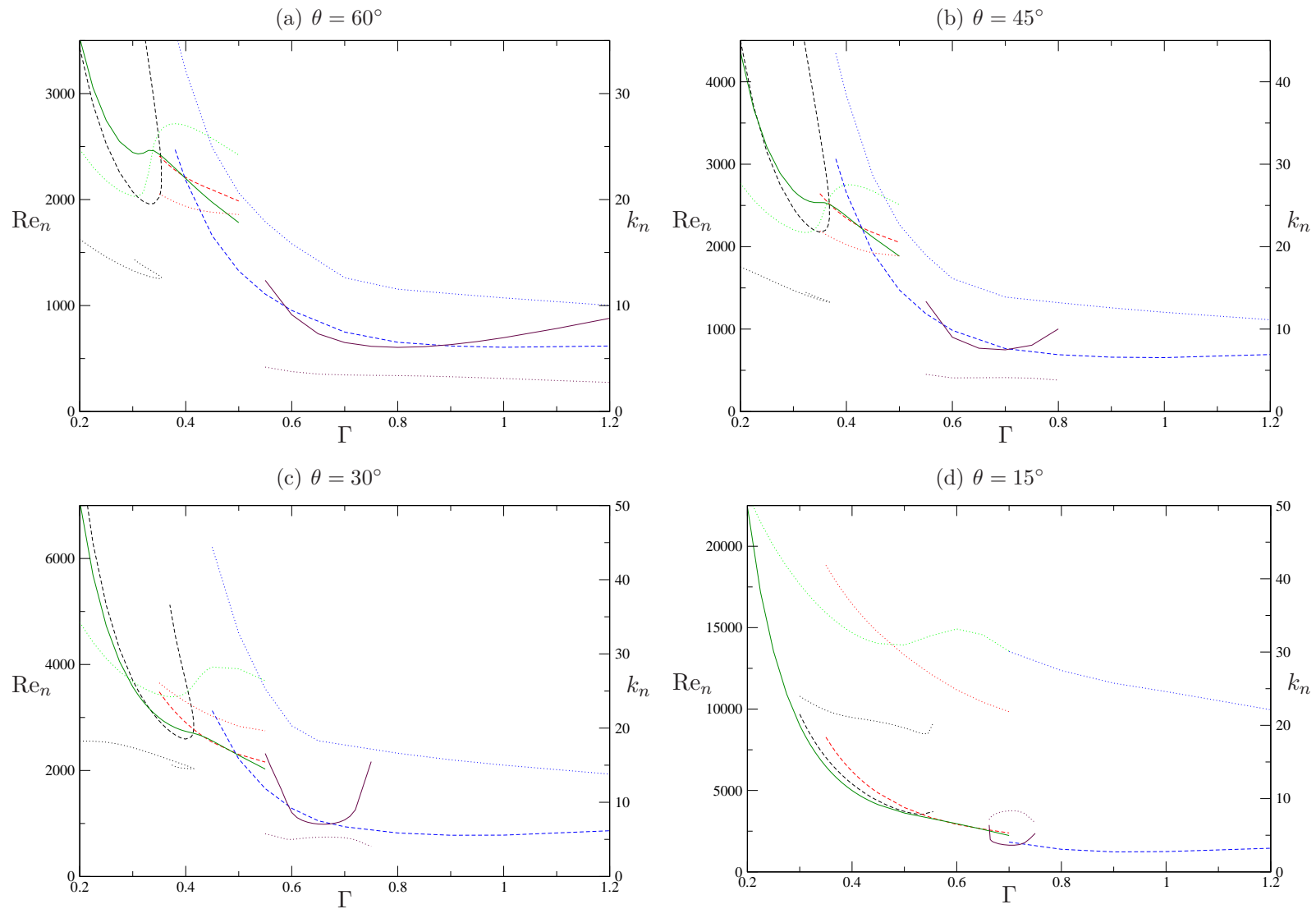


Figure 5.21: Neutral curves for different angles θ as indicated. Re_n for oscillatory modes (mode 1 (black), mode 2 (red), mode 4 (blue)) are represented by dashed lines, and for stationary modes (mode 3 (green), mode 5 (maroon)) by solid lines. Dotted lines represent corresponding wave number k .

elliptic nature for small aspect ratio $\Gamma \leq 0.65$ except for a very small range $0.57 < \Gamma < 0.63$ where mode 2 define the limits of marginal stability. The region

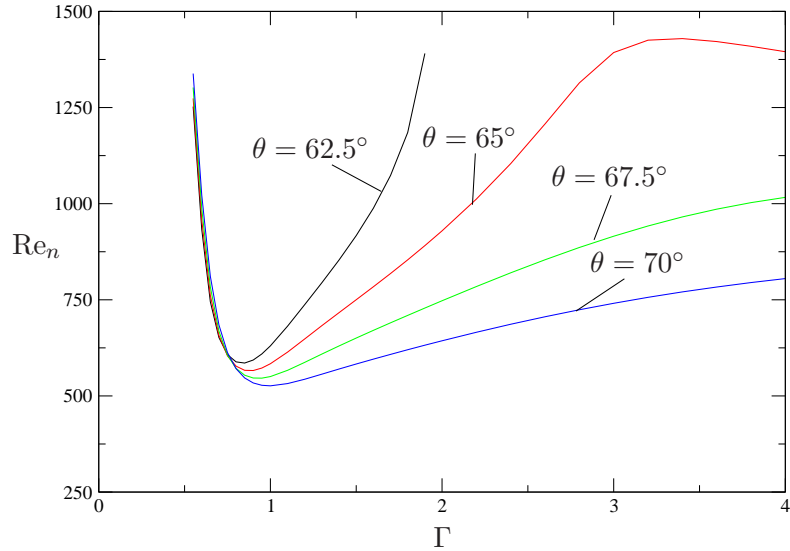


Figure 5.22: Qualitative changes in behaviour of the neutral curve for mode 5 with change of angle θ in the range shown.

occupied by stationary centrifugal mode (mode 5) as the most dangerous mode shrinks in term of Γ as θ decreases and at $\theta = 15^\circ$ it occupies a very small region of $0.66 < \Gamma < 0.73$ for being the most dangerous mode. The qualitative changes in behaviour of mode 5 occurring in the range $\theta = [70^\circ - 60^\circ]$ are shown in figure 5.22. It can be observed that the neutral curve for mode 5 is no more a continuous curve for $\theta < 65^\circ$ at higher aspect ratio $\Gamma > 1.7$.

Variation of the neutral curves with increase in θ from 90° are shown in figure 5.23. The region occupied by the mode 1 for being the most dangerous mode expands in Γ as the angle θ is increased from 90° , so that the turning point of the neutral curve shifts from $\Gamma \approx 0.397$ for $\theta = 90^\circ$ to $\Gamma \approx 0.96$ for $\theta = 135^\circ$. Accordingly the positions for mode 2 and mode 3 also changes with a shrinkage of region in Γ for mode 3 to be the most dangerous mode and finally at $\theta = 135^\circ$ mode 3 does not appear as the most dangerous mode at all. Similarly the first appearance of mode 4 as the most dangerous mode, is also displaced toward higher Γ as θ is increased. The first appearance of mode 4 as the most dangerous

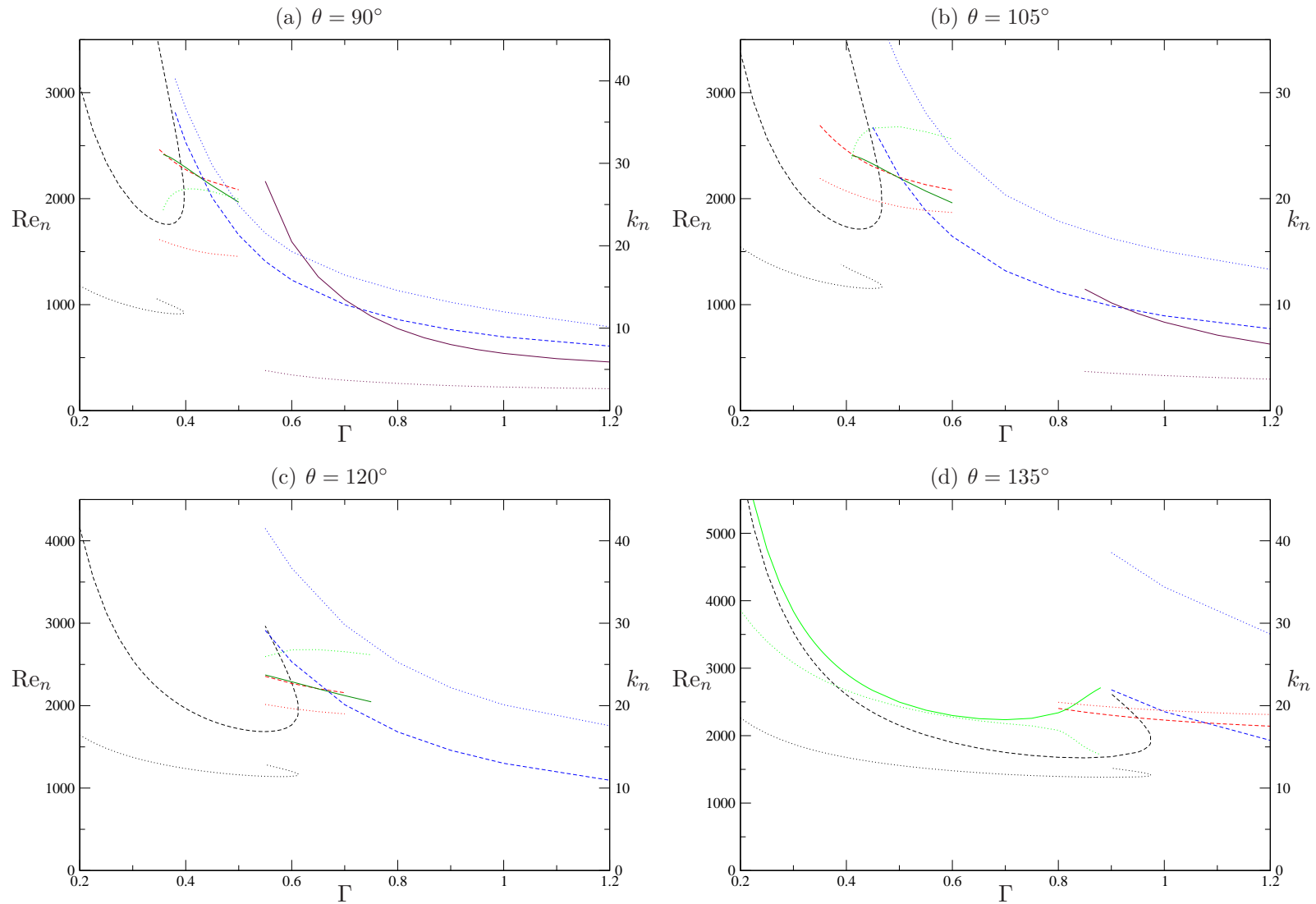


Figure 5.23: Neutral curves for different angles θ as indicated. Re_n for oscillatory modes (mode 1 (black), mode 2 (red), mode 4 (blue)) are represented by dashed lines, and stationary modes (mode 3 (green), mode 5 (maroon)) by solid lines. Dotted lines represent corresponding wave number k .

5. Results and Discussion

mode for $\theta = 90^\circ$ at $\Gamma \approx 0.43$ is shifted to $\Gamma \approx 1.15$ for $\theta = 135^\circ$. Once again a drastic change in the behaviour of mode 5 is observed, whose first appearance as the most dangerous mode for $\theta = 90^\circ$ at $\Gamma \approx 0.7$ is shifted to $\Gamma \approx 3.1$ (not visible in figures) for $\theta = 135^\circ$.

To get more clear picture about the variation of modes with change in angle θ , the neutral curves for small aspect ratios $\Gamma = [0.3, 0.35, 0.4, \text{ and } 0.5]$ are shown in figure 5.24. For $\Gamma = 0.3$ (figure 5.24(a)) mode 1 remains the most dangerous mode for $135^\circ > \theta > 35^\circ$. A cross over of the neutral curves for mode 1 and mode 3 occurs at $\theta \approx 35^\circ$, so for $\Gamma = 0.3$ and $\theta < 35^\circ$ mode 3 is the most dangerous mode for instability to evolve. Qualitatively the neutral curves for $\Gamma = 0.35$ (figure 5.24(b)) are same as for $\Gamma = 0.3$ with minor differences. The first difference is the shift of the cross over point of the two most dangerous modes (mode 1 and mode 3) to $\theta \approx 28^\circ$. A second observable difference is a minor kink in the neutral curve at $\theta \approx 60^\circ$, which gives an indication of breakdown of the neutral curve for mode 1 at higher Γ . It could be noted that for small aspect ratios $\Gamma < 0.35$ mode 1 and mode 3 are the only dangerous modes. For $\Gamma = 0.4$ (5.24(c)) the curve for mode 1 is not a continuous one as it return back at $\theta \approx 32.5^\circ$. Mode 1 however reappears at $\theta \approx 92^\circ$, where it forms a turning curve facing in reverse direction to the initial appearance at small θ . Mode 1 remains the most dangerous mode in the region $24^\circ < \theta < 32.5^\circ$ and $\theta > 92^\circ$ for $\Gamma = 0.4$. Mode 3 becomes the most dangerous mode in the region $\theta < 24^\circ$ and in a thin region of $33.5^\circ < \theta < 35.5^\circ$. Mode 2 becomes visible now as a dangerous mode for $\Gamma = 0.4$ and the two regions where it is most dangerous is $35.5^\circ \leq \theta \leq 57.5^\circ$ and $77.5^\circ \leq \theta \leq 92.5^\circ$. Once again the mode 3 and mode 2 are very close to each other in terms of Re. Mode 4 is also visible for $\Gamma = 0.4$ and it occupies the region $57.5^\circ \leq \theta \leq 77.5^\circ$ for being the most dangerous mode. It can be seen that in the region $57.5^\circ \leq \theta \leq 77.5^\circ$ the three modes (mode 2,3,4) are very close in terms of Re from figure 5.24(c). For $\Gamma = 0.5$ (figure 5.24(d)) in contrast to $\Gamma = 0.4$ the mode 1 does not appear at small θ , however it appear only at higher angles and is most dangerous for $\theta > 110^\circ$, where the neutral curve turns back with the upper bound on Re. At small angles $\theta < 21.5^\circ$ mode 3 remains the most dangerous mode for $\Gamma = 0.5$ as was the case for other small aspect ratios. Mode 2 once again becomes most dangerous mode in two regions with $21.5^\circ \leq \theta \leq 28.5^\circ$ and $105^\circ \leq \theta \leq 110.5^\circ$

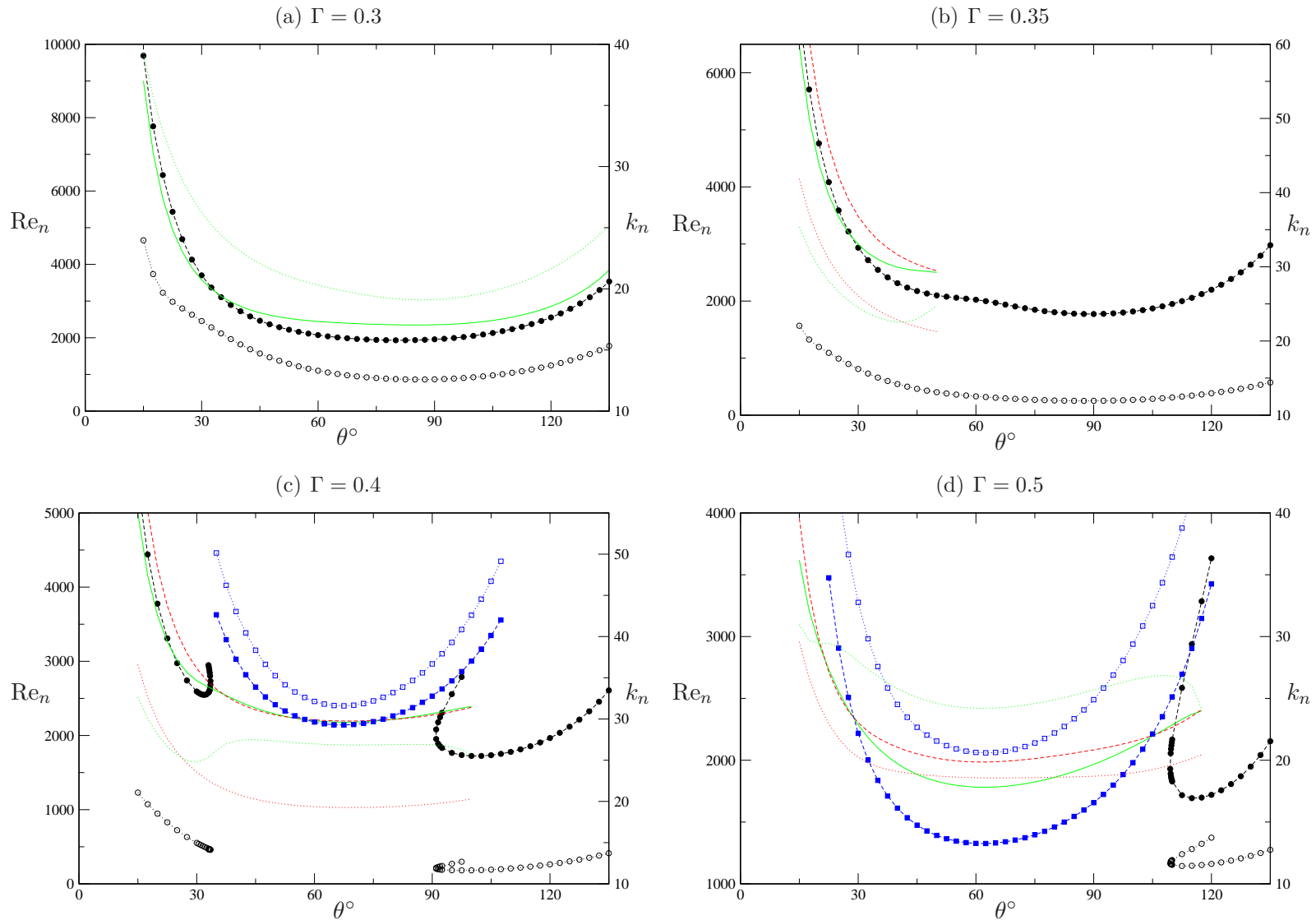


Figure 5.24: Neutral curves for different aspect ratios Γ as indicated. Re_n for oscillatory modes (mode 1 (black, circles), mode 2 (red), mode 4 (blue, squares)) are represented by dashed lines, mode 3 (green) by solid lines. Dotted lines (hollow symbols) represent corresponding wave number k .

for $\Gamma = 0.5$. Mode 4 occupies a large region $28.5^\circ \leq \theta \leq 105^\circ$ for being the most dangerous mode for $\Gamma = 0.5$.

As the aspect ratio is increased beyond 0.5 the straining of the primary eddy becomes weak due to increase of the available area for fluid flow. The elliptic instability mechanism gradually vanishes, and the centrifugal modes are dominant. The neutral curve for different aspect ratios $\Gamma = [1.0, 1.5, 2.0, \text{ and } 3.0]$ are shown in figure 5.25. It can be seen that only the centrifugal modes (mode 4 and 5) are the dangerous modes for this range of Γ . The zone where mode 5 is most dangerous is shifted towards higher angles for an increase in the Γ , as this mode is most dangerous in the range of $64^\circ \leq \theta \leq 107^\circ$ for $\Gamma = 1.0$ and shifted to $78^\circ \leq \theta \leq 133^\circ$ for $\Gamma = 3.0$. A turn or a jump in the curve for neutral wave number k_n could be observed for $\Gamma = 2$ and 3.0 at $\theta = 19^\circ$ and 36° respectively. This turning of the curve for neutral wave number could be explained by the curves for dangerous growth rate (real part of most dangerous eigenvalue) for a constant Re at different θ in the neighbourhood of the turning zone as shown in figure 5.26(a). It can be seen that for $\theta = [36^\circ - 38^\circ]$ the growth rate makes two peaks, without any discontinuity at $\text{Re} = 725$ (very close to criticality). The continuity in the oscillating frequency also suggests a jump in k but physically the same mode. the neutral curves (figure 5.26(b)) clearly shows the continuity of the mode in terms of oscillating frequency and the regions where the $\frac{\partial \text{Re}}{\partial k}$ vanishes.

5.1.3 Summary of results

The major observations for instability modes with the lid motion directed away from a specified angle between two sides of specified lengths of a triangular cavity could be summarized as

- For small aspect ratios $\Gamma < 0.36$ mode 1 and mode 3 are the dangerous modes, where as mode 3 is active at small angles θ the value of which depends on the Γ (figure 5.24(a & b)).
- At moderately small aspect ratios $0.36 \leq \Gamma \leq 0.39$ mode 2 becomes visible as a dangerous mode for moderate angles $32^\circ \leq \theta \leq 90^\circ$. The curve for mode 1 splits into two parts and the mode is dangerous only at the two

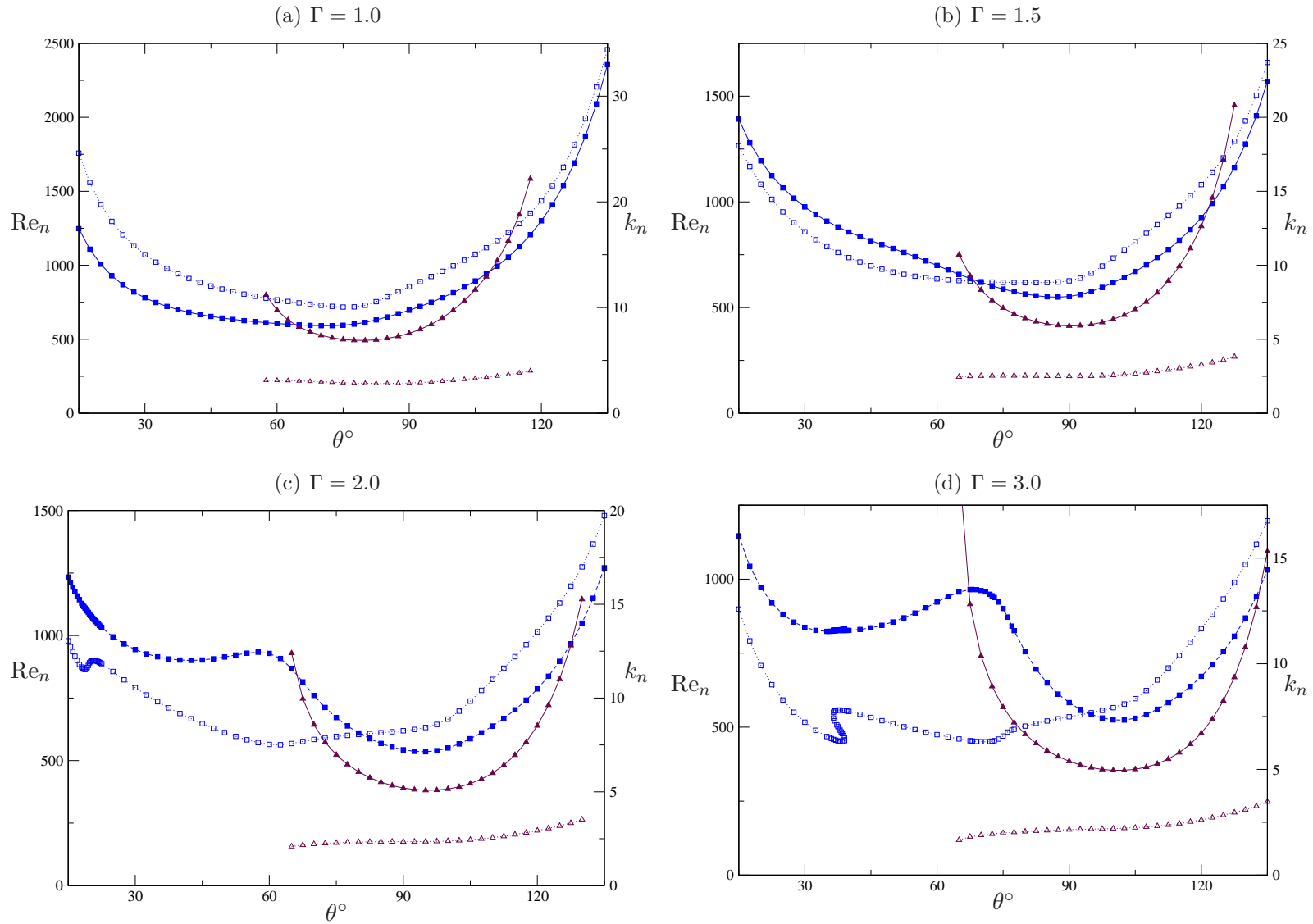


Figure 5.25: Neutral curves for different aspect ratios Γ as indicated. Re_n for mode 4 is represented by blue lines (squares), mode 5 is represented by maroon lines (triangles). Dotted lines (hollow symbols) represent corresponding wave number k_n .

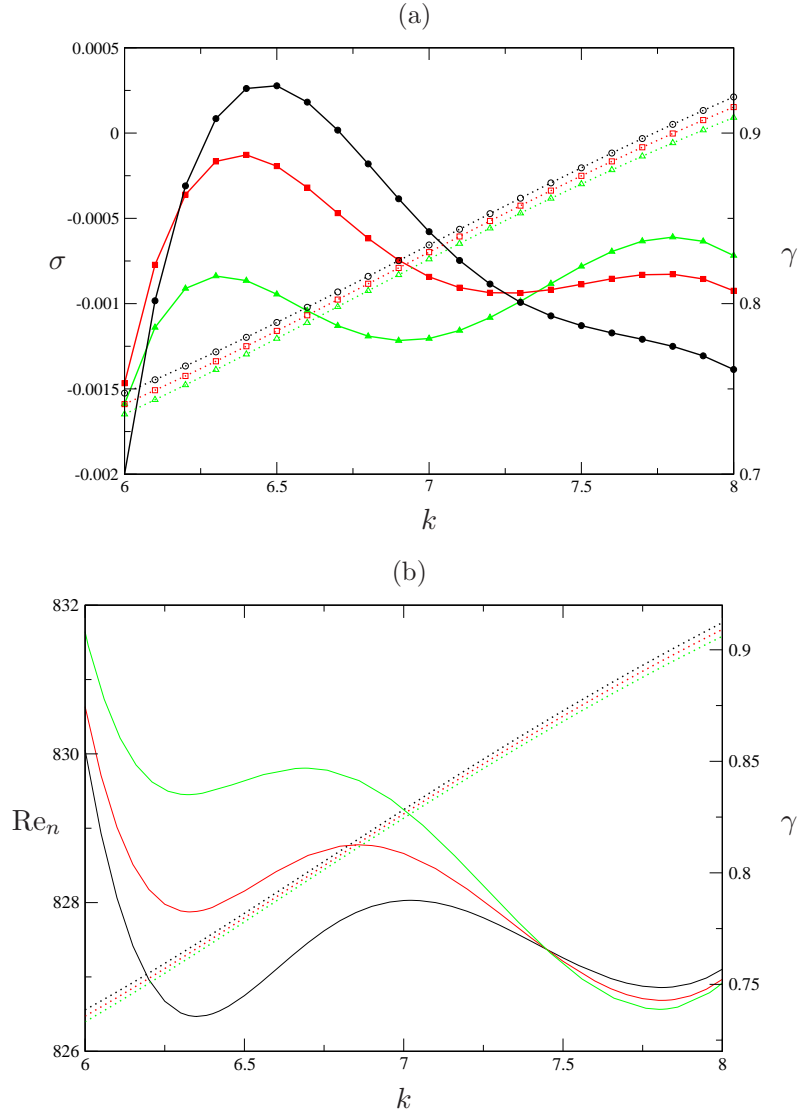


Figure 5.26: (a) Growth rate σ (full lines and symbols) and γ (dotted lines and hollow symbols) as a function of k for $\Gamma = 3.0$, $\text{Re} = 725$ and $\theta = 36^\circ$ (black, circles), $\theta = 37^\circ$ (red, squares) and $\theta = 38^\circ$ (green, triangles), (b) Re_n (full lines) and oscillating frequency γ (dotted lines) as a function of k for $\Gamma = 3.0$ and $\theta = 37.5^\circ$ (black), $\theta = 38^\circ$ (red) and $\theta = 38.5^\circ$ (green).

ends with respect to θ . Mode 3 remains the dangerous mode at small angles θ (figure 5.24(b & c)).

- For aspect ratio of $\Gamma = 0.4$ mode 4 appears as the dangerous mode at

$57.5^\circ \leq \theta \leq 77.5^\circ$ splitting the dangerous zone of mode 2 into two parts. As the aspect ratio is increased the region in θ where the mode 4 is most dangerous is enlarged covering the region $28^\circ \leq \theta \leq 105^\circ$ for $\Gamma = 0.5$, where as the portion of neutral curve for mode 1 at small angles shrinks and finally disappears at $\Gamma = 0.5$ (figure 5.24(c & d)).

- Mode 5 is never a dangerous mode for small aspect ratios $\Gamma \leq 0.5$ and is thus not visible in the figures for neutral curves of small aspect ratios(figures 5.24. However at higher aspect ratios $\Gamma > 0.6$ the mode appears as the most dangerous mode at $\theta \geq 62.5^\circ$ splitting the region of where mode 4 is most dangerous mode into two parts. the upper limit of θ for which mode 5 is most dangerous mode depends on Γ (figures 5.25).
- The appearance of certain mode as a dangerous mode depends on the structure of the primary vortex or primary eddy, which depends apart from other parameters strongly on the shape of the cavity.
- For small aspect ratio $\Gamma \ll 1.0$ where the downstream angle is small, the instability mechanism is elliptic in nature and the curve for appropriately rescaled Reynolds number Re_n^* shows a trend of divergence or in other words stabilization of basic flow.

The limits of aspect ratio Γ at which different modes act as the most dangerous mode are summarized in table 5.2 for representative cases of upstream angles θ .

5.2 Lid moving in negative x -direction

Although a general idea could be captured from the results in previous section regarding the results for motion of the lid directed towards the specified angle, by calculating the downstream angle and length of the third side for aspect ratio. However to get a complete picture the complete parameter variation is necessary. In this section the different modes will be discussed by their dominant occurrence in the parameter space.

Table 5.2: Limits of aspect ratio Γ in which different modes are most dangerous at specific upstream angles θ .

θ	Mode 1	Mode 2	Mode 3	Mode 4	Mode 5
15°		$0.577 \leq \Gamma \leq 0.63$	$\Gamma \leq 0.577$ & $0.63 \leq \Gamma \leq 0.667$	$\Gamma > 0.724$	$0.667 \leq \Gamma \leq 0.724$
30°	$0.33 \leq \Gamma \leq 0.41$	$0.434 \leq \Gamma \leq 0.48$	$\Gamma \leq 0.33$, $0.41 \leq \Gamma \leq 0.434$ & $0.48 \leq \Gamma \leq 0.495$	$0.495 \leq \Gamma \leq 0.593$ & $\Gamma \geq 0.675$	$0.595 \leq \Gamma \leq 0.675$
45°	$0.23 \leq \Gamma \leq 0.368$	$0.368 \leq \Gamma \leq 0.421$	$\Gamma \leq 0.23$, & $0.421 \leq \Gamma \leq 0.43$	$0.43 \leq \Gamma \leq 0.58$ & $\Gamma \geq 0.7$	$0.58 \leq \Gamma \leq 0.7$
60°	$\Gamma \leq 0.35$	$0.35 \leq \Gamma \leq 0.393$	$0.393 \leq \Gamma \leq 0.398$	$0.398 \leq \Gamma \leq 0.59$ & $\Gamma \geq 0.88$	$0.59 \leq \Gamma \leq 0.88$
75°	$\Gamma \leq 0.36$	$0.36 \leq \Gamma \leq 0.393$	$0.393 \leq \Gamma \leq 0.399$	$0.399 \leq \Gamma \leq 0.63$	$\Gamma \geq 0.63$
90°	$\Gamma \leq 0.391$	$0.391 \leq \Gamma \leq 0.422$	$0.422 \leq \Gamma \leq 0.434$	$0.434 \leq \Gamma \leq 0.726$	$\Gamma \geq 0.726$
105°	$\Gamma \leq 0.46$	$0.46 \leq \Gamma \leq 0.49$	$0.49 \leq \Gamma \leq 0.505$	$0.505 \leq \Gamma \leq 0.93$	$\Gamma \geq 0.93$
120°	$\Gamma \leq 0.61$	$0.61 \leq \Gamma \leq 0.645$	$0.645 \leq \Gamma \leq 0.67$	$0.67 \leq \Gamma \leq 1.41$	$\Gamma \geq 1.41$
135°	$\Gamma \leq 0.975$	$0.975 \leq \Gamma \leq 1.07$		$1.07 \leq \Gamma \leq 3.4$	$\Gamma \geq 3.4$

5.2.1 Mode 1

This mode occurs as a dangerous mode for $\Gamma > 0.5$ and $\theta \leq 22.25^\circ$ in the parameter space. As an example the neutral Reynolds Re_n and wave numbers

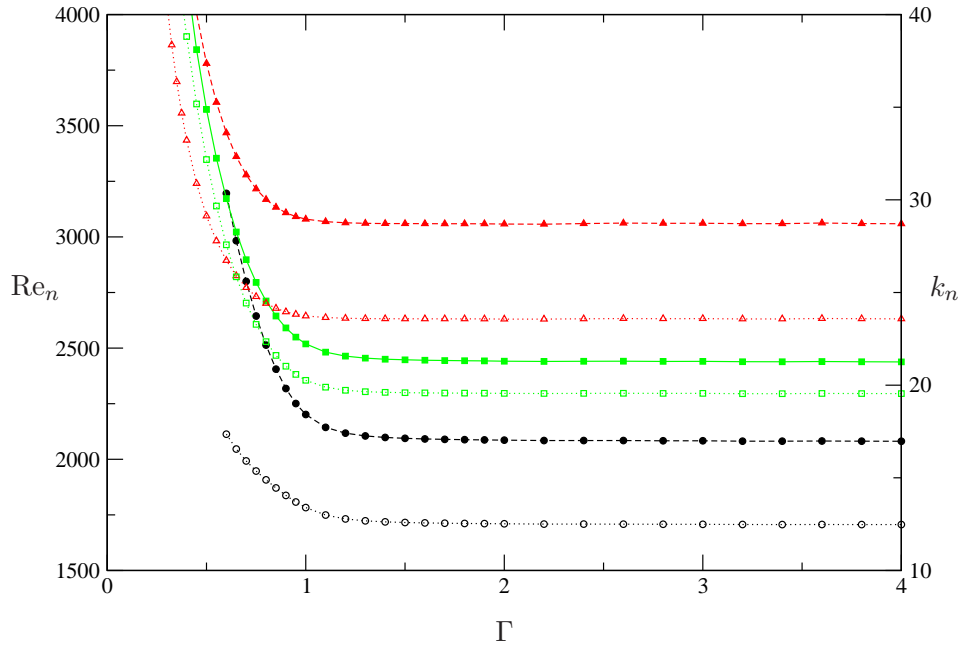


Figure 5.27: Neutral Reynolds number Re_n (full symbols and solid lines: stationary modes, dashed lines: oscillatory modes) and wave number k_n (hollow symbols with dotted lines) as functions of the aspect ratio Γ for $\theta = 15^\circ$. Modes are indicated by black circles (mode 1), red triangles (mode 2), green squares (mode 3).

k_n is provided in fig. 5.27 for a downstream angle $\theta = 15^\circ$, which shows the dependence of these data on the aspect ratio Γ . The neutral curves takes an asymptotic value of $Re_n \approx 2081$ and $k_n \approx 12.48$ for higher aspect ratios at $\Gamma \approx 1.5$. On the other side at small aspect ratios mode 3 crosses mode 1 at $\Gamma \approx 0.6$, and below an aspect ratio of 0.6 mode 1 is no more the most dangerous mode.

To get more en-sight about the variation of mode 1 the neutral curves for different aspect ratios $\Gamma = [0.5, 1.0, 2.0, \text{ and } 3.0]$ are presented in figure 5.28, which shows the dependence of Re_n and k_n on the downstream angle θ for these aspect ratios. It can be seen from figure 5.28(a) that mode 1 is not the most dangerous

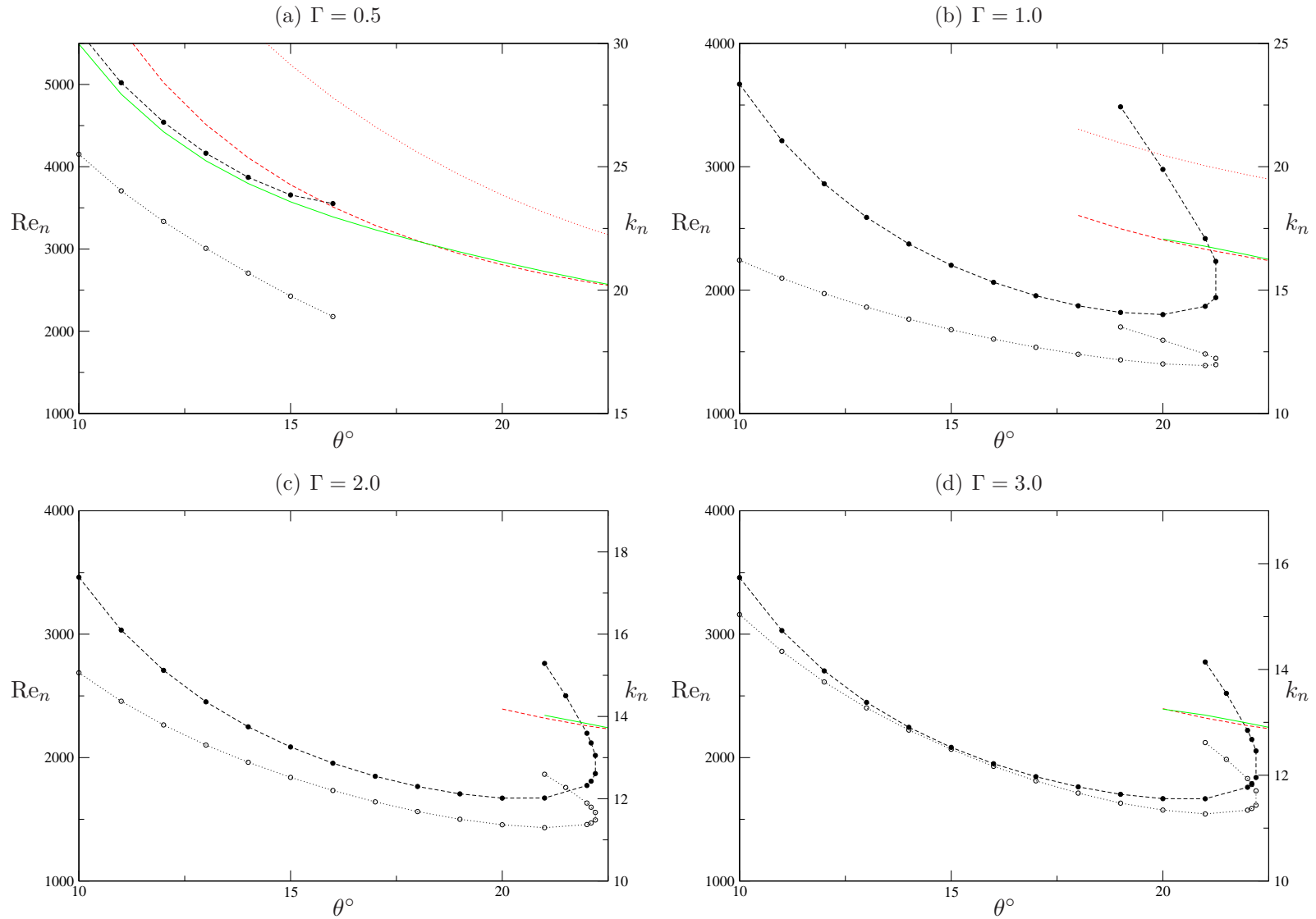


Figure 5.28: Neutral curves for different aspect ratios Γ as indicated. Re_n for mode 1 is represented by black dashed line (full circles), mode 2 and mode 3 are represented by red dashed line and green solid line respectively. Dotted lines (hollow symbols) represent corresponding wave number k_n .

Table 5.3: Limits of turning point of neutral curve for mode 1, when the lid moves away from a specified angle $\theta_{upstream}$ and the calculated corresponding downstream angles $\theta_{downstream}$.

Γ	$\theta_{upstream}$	$\theta_{downstream}$
0.363	75°	21.2°
0.397	90°	21.7°
0.467	105°	21.9°
0.612	120°	22.1°
0.974	135°	22.2°

mode for $\Gamma = 0.5$ at any angle. The neutral curves turns back at $\theta \approx 21.3^\circ$ for $\Gamma = 1.0$ and at $\theta \approx 22.25^\circ$ for $\Gamma = [2.0, 3.0]$. This turning behaviour of mode 1 was already seen at certain Γ for a fixed upstream angle θ in previous section such as figures (5.3, 5.21, 5.23). In fact if the downstream angle is calculated from aspect ratio and upstream angle in previous section it approximates the downstream angle to be $\theta \approx [21^\circ \text{ to } 22^\circ]$ as the limiting case for turning point. The data of such calculation is represented in table 5.3 for some cases. As a second

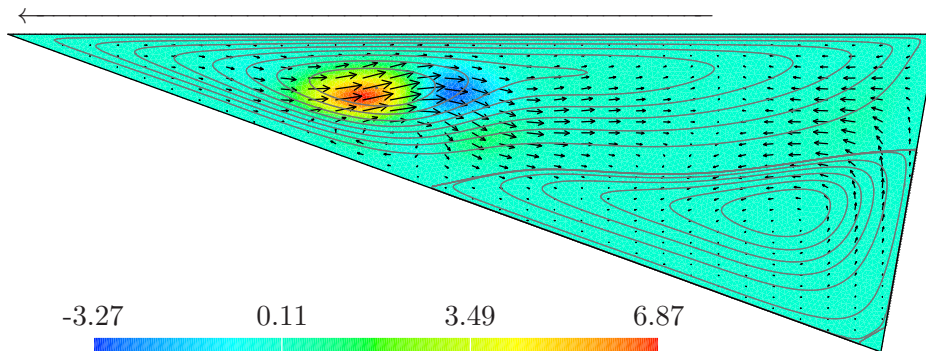


Figure 5.29: Basic state streamlines at $Re_c = 1801.93$ for $\Gamma = 1.0$ and $\theta = 20^\circ$ (different levels of isolines are used to show the secondary and tertiary eddies) along with the critical mode (arrows) and the total local energy production rate $\sum_i I_i$ (color) in a plane $z = \text{const.}$ in which $\sum_i I_i$ takes its absolute maximum. Long arrow at top indicates lid motion.

example of mode 1 in present context the streamlines, perturbation modes and energy production terms are presented for a cavity of unit aspect ratio and down-

stream angle $\theta = 20^\circ$ in a plan $z = \text{const}$ where the maxima of energy production occurs, in figure 5.29 at critical conditions of $\text{Re}_c = 1801.93$ and $k_c = 12.00$. It can be seen that figure 5.29 appears a reflection of figure 5.4 except a change in the upstream angle. All the qualitative similarities is a proof that it is the same mode 1 discussed in previous section. Discussion about the details will not be repeated here.

5.2.2 Mode 2 & mode 3

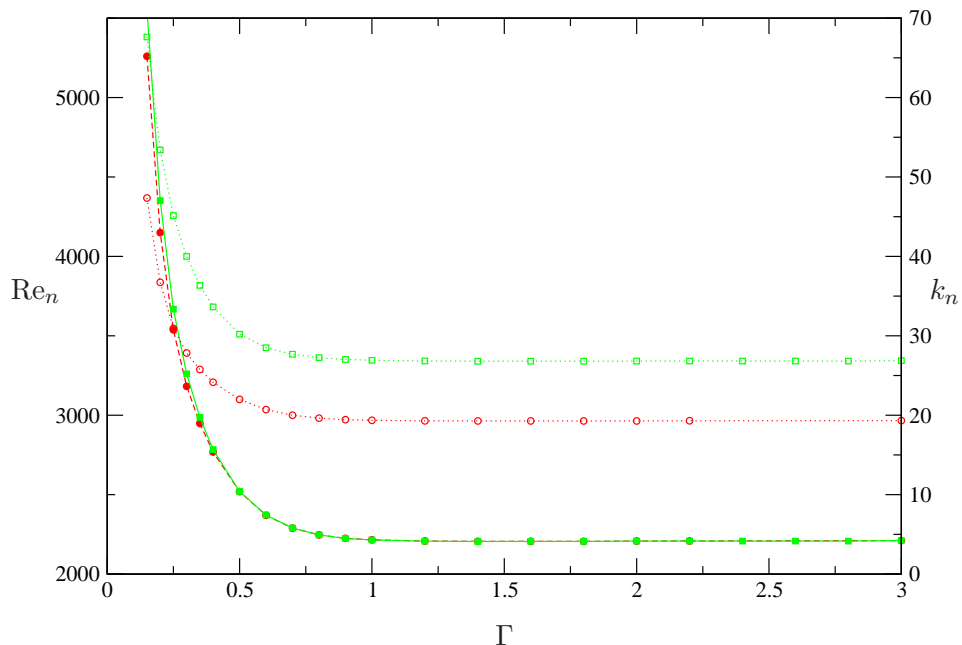


Figure 5.30: Neutral Reynolds number Re_n (full symbols and solid lines: stationary modes, dashed lines: oscillatory modes) and wave number k_n (hollow symbols with dotted lines) as functions of the aspect ratio Γ for $\theta = 23^\circ$. Modes are indicated by red circles (mode 2), green squares (mode 3).

The dominant region where these two close modes are the most dangerous modes are the upstream angle of $21^\circ \leq \theta \leq 24^\circ$ for the whole range of aspect ratios of $0.2 \leq \Gamma \leq 4.0$ for which calculations were made. Although the mode 3 also occupy the region $\Gamma \leq 0.6$ and upstream angle $\theta < 21^\circ$ as the most dangerous mode, an example of which is the $\theta = 15^\circ$ previously discussed, where mode 3 becomes the most dangerous mode at $\Gamma \leq 0.6$. As an example the neutral

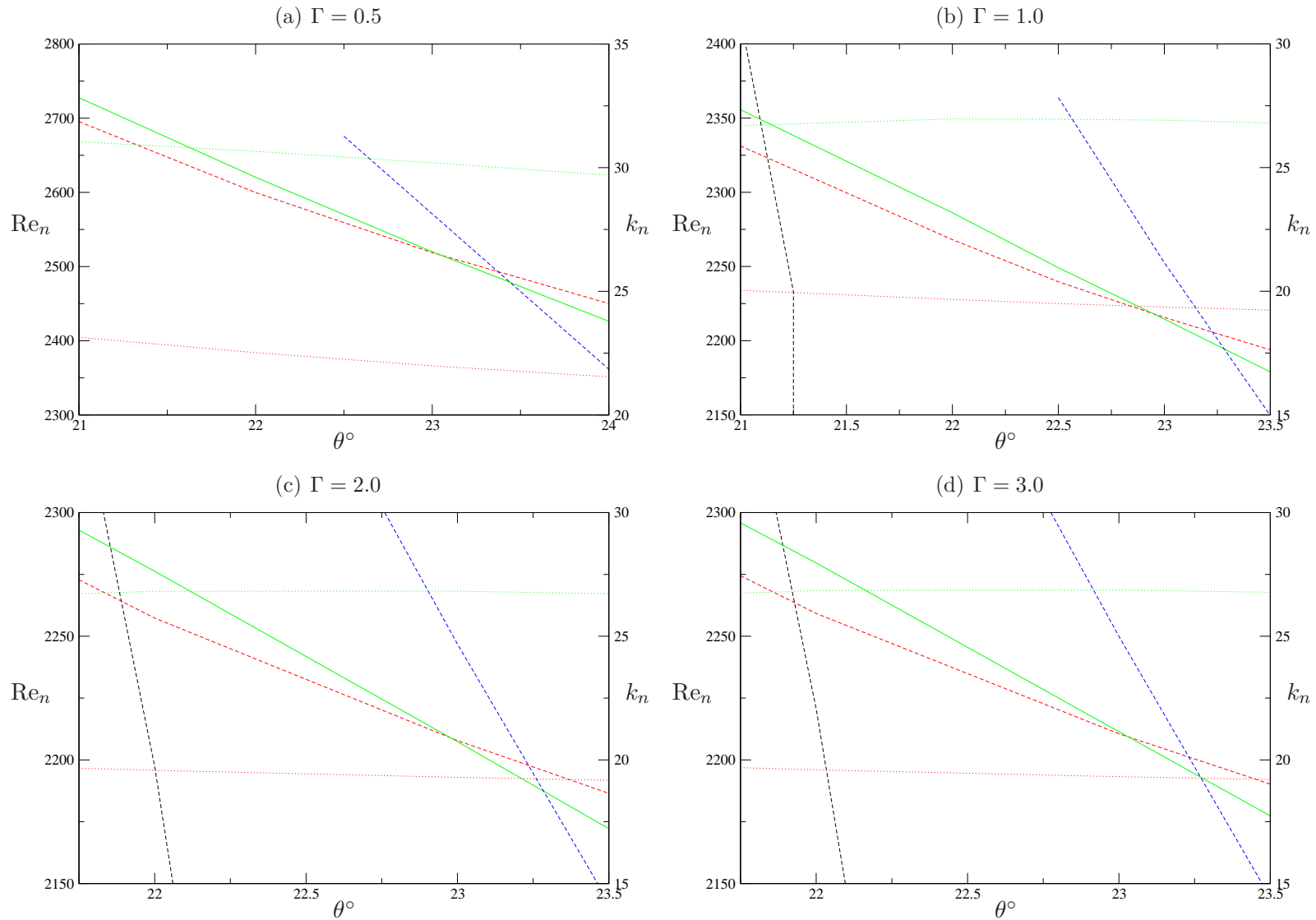


Figure 5.31: Neutral curves for different aspect ratios Γ as indicated. Re_n for mode 2 is represented by red dashed line, mode 3 is represented by green solid line. Dotted lines with same colour scheme represent corresponding wave number k_n . Black and blue dashed lines indicate mode 2 and mode 4 respectively.

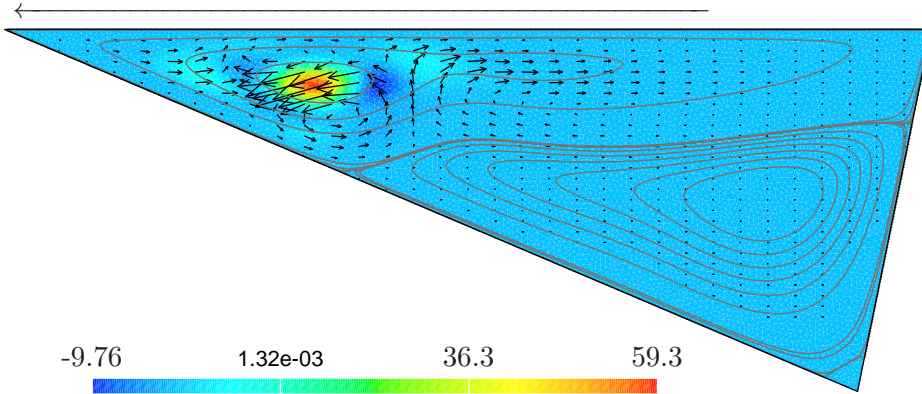


Figure 5.32: Basic state streamlines at $Re_c = 2214.5$, $k = 26.916$ for $\Gamma = 1.0$ and $\theta = 23^\circ$ (different levels of isolines are used to show the secondary and tertiary eddies) along with the critical mode (arrows) and the total local energy production rate $\sum_i I_i$ (color) in a plane $z = \text{const.}$ in which $\sum_i I_i$ takes its absolute maximum. Long arrow at top indicates lid motion.

Reynolds Re_n and wave numbers k_n is provided in fig. 5.30 for $\theta = 23^\circ$, which shows the dependence of these data on the aspect ratio Γ . The neutral curves takes an asymptotic value of $Re_n \approx 2206$ for both modes and $k_n \approx 19.27$ (mode 2) and $k_n \approx 26.81$ (mode 3) for higher aspect ratios at $\Gamma \approx 1.5$. The closeness of the neutral curves of the two modes for Re_n is obvious as they overlap each other for $\Gamma > 0.4$. However for $\Gamma \leq 0.4$ the curves for Re_n of the two modes are distinguishable. Interestingly mode 2 becomes the most dangerous mode at small aspect ratios $\Gamma < 0.4$ for $\theta = 23^\circ$ in contrast to $\theta = 15^\circ$ where mode 3 is the most dangerous mode for the same range of aspect ratios. This change in the behaviour of the neutral curve could be explained by revisiting the figure 5.28(a), where the behavioural change of the neutral curve for Re_n along upstream angle θ for an aspect ratio of $\Gamma = 0.5$ is shown. The crossover of mode 2 and mode 3 at an upstream angle of $\theta \approx 17.5^\circ$ indicates that for $\theta \leq 17.5^\circ$ mode 3 will be the more dangerous if compared with mode 2, and vice versa will be true for $\theta > 17.5^\circ$. So in the present case of $\theta = 23^\circ$ the occurrence of mode 2 as the most dangerous mode at small aspect ratios is analogous to the previous results.

To get more en-sight about the variation of these modes the neutral curves for different aspect ratios $\Gamma = [0.5, 1.0, 2.0, \text{ and } 3.0]$ are presented in figure 5.31,

which shows the dependence of Re_n and k_n on the θ for these aspect ratios. Once again the absence of mode 1 in figure 5.28(a) indicates that it is not the most dangerous mode for $\Gamma = 0.5$. The crossing of mode 1 and mode 2 for $\Gamma = 1.0$ at downstream angle of $\theta \approx 21.1^\circ$ is shifted to $\theta \approx 21.9^\circ$ for $\Gamma = 2.0$ which remains the same for $\Gamma = 3.0$, due to the fact that the neutral curves takes the asymptotic value at $\Gamma \approx 1.5$ for all the three modes involved (mode 1, 2 and 3). On the other limit these modes are succeeded by mode 4 as the most dangerous mode at $\theta \approx [23.4^\circ, 23.3^\circ, 23.25^\circ, \text{ and } 23.25^\circ]$ for $\Gamma = [0.5, 1.0, 2.0, \text{ and } 3.0]$.

As the details of perturbation flow field of these mode were already presented previously. Over here only a cut at $z = const$ at position of maximum energy production is presented in figure 5.32 for a unit aspect ratio cavity and downstream angle of $\theta = 23^\circ$ as a second example of mode 3 at critical conditions of $(Re_n, k_n) = (2214.5, 26.91)$. Once again figure 5.32 appears as a reflection of figure 5.12 except a change in the upstream angle.

5.2.3 Mode 4 & mode 5

These two modes occupy a large parameter space i.e $23.3^\circ \leq \theta \leq 135^\circ$ and $0.2 \leq \Gamma \leq 4.0$, as the most dangerous modes. As some representative examples of the neutral curves for Re_n and k_n are presented in figure 5.33 for $\theta = [30^\circ, 45^\circ, 60^\circ, 75^\circ]$ and figure 5.34 for $\theta = [90^\circ, 105^\circ, 120^\circ, 135^\circ]$, which shows the dependence of these data on aspect ratio Γ . It can be observed from these figures that for small aspect ratio (limit of which depends on the downstream angle θ), it is always mode 4 to be the most dangerous mode. The limit of aspect ratio below which mode 4 becomes the most dangerous mode varies from $\Gamma = 0.3$ for $\theta = 30^\circ$ to $\Gamma = 2.1$ for $\theta = 90^\circ$, where as this limit goes beyond $\Gamma = 4$ for $\theta = 105^\circ$ as mode 4 appears as the only dangerous mode for $\theta = 105^\circ$ in the space $\Gamma = [0.2 - 4.0]$ (figure 5.34(b)). For medium range of downstream angles $45^\circ \leq \theta \leq 90^\circ$ mode 5 appears as the most dangerous mode at some point of aspect ratio $\Gamma < 4.0$ and takes an asymptotic value at higher aspect ratio the limit of which depends on θ , as can be seen from figure 5.33, which shows an increase in the limit of Γ for the neutral curves to take asymptotic values with increase of angle θ . For higher downstream angles $\theta \geq 105^\circ$, the appearance of mode 5 is more delayed in

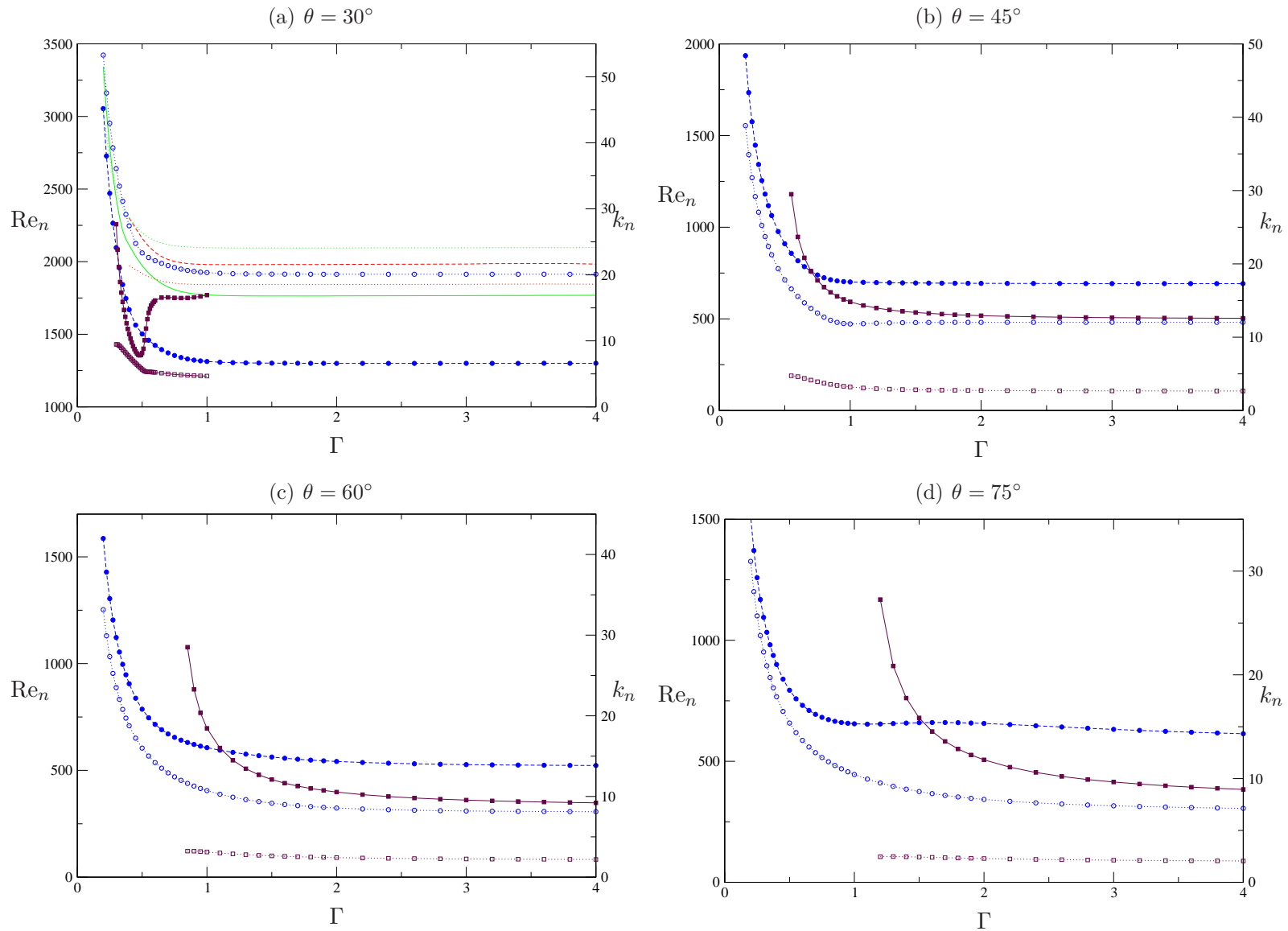


Figure 5.33: Neutral curves for different downstream angles θ as indicated. Re_n for modes (2,3,4 and 5) are represented by red dashed, green solid, blue dashed (circles) and maroon solid (squares) lines respectively. Dotted lines (hollow symbols, and same colour scheme) represent corresponding wave number k_n .

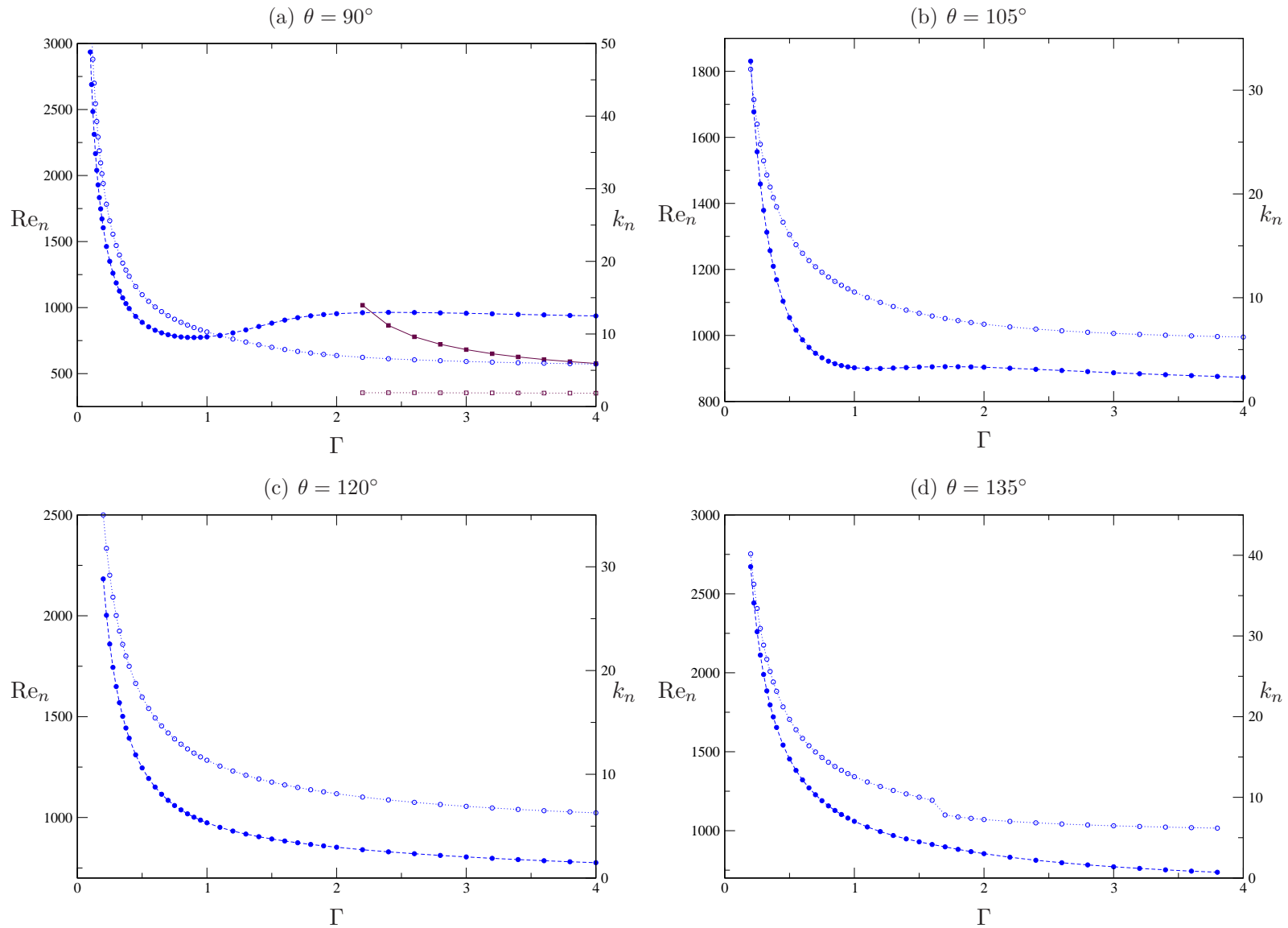


Figure 5.34: Neutral curves for different downstream angles θ as indicated. Re_n for modes (4 and 5) are represented by blue dashed (circles) and maroon solid (squares) lines respectively. Dotted lines (hollow symbols, and same colour scheme) represent corresponding wave number k_n .

terms of Γ and was not detected as the most dangerous mode even at $\Gamma = 4.0$ for $\theta = 105^\circ$. A change of trend of neutral curves for mode 5 occurs at downstream angle of $\theta \leq 35^\circ$. The neutral curve for Re_n takes a minimum and then rises to higher values before taking an asymptotic value. This change of behaviour is shown in figure 5.35. Below a limit of $\theta = 32.5^\circ$ mode 5 is no more the most dangerous mode for instabilities at higher aspect ratio $\Gamma > 0.6$, and as such the most dangerous mode is mode 4 as is obvious from figure 5.21(a) for $\theta = 30^\circ$.

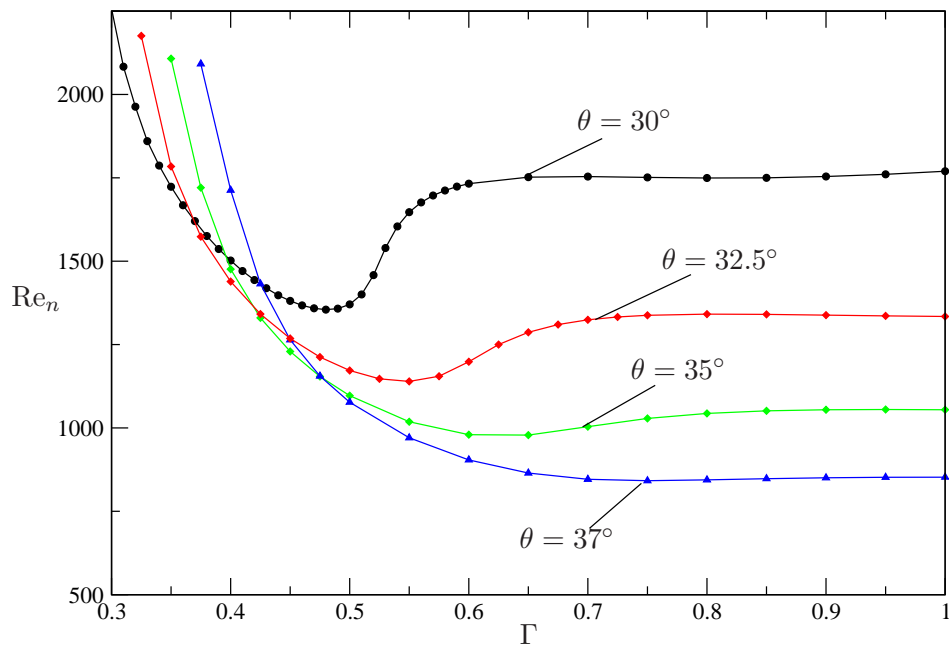


Figure 5.35: Change in behaviour of neutral curves of mode 5 for downstream angles θ mentioned in the region $\Gamma \leq 1.0$.

Dependence of Re_n and k_n on the downstream angle θ for specific cases of $\Gamma = [0.5, 1.0, 2.0, 3.0]$ in the region where mode 4 or mode 5 are the most dangerous modes is shown in figure 5.36. It can be observed that the region in θ for mode 5 to be the most dangerous mode, increases with an increase in aspect ratio Γ .

An interesting feature of the mode 4 for the limit $\Gamma \rightarrow 0$ could be observed by rescaling of the parameters appropriately as in equation 5.1, for $\theta > 23^\circ$. An example of rescaled Re_n^* , k_n^* , and ω_n^* as a function of Γ is shown in figure 5.37. The rescaled Reynolds number remains finite, with the neutral curves showing a

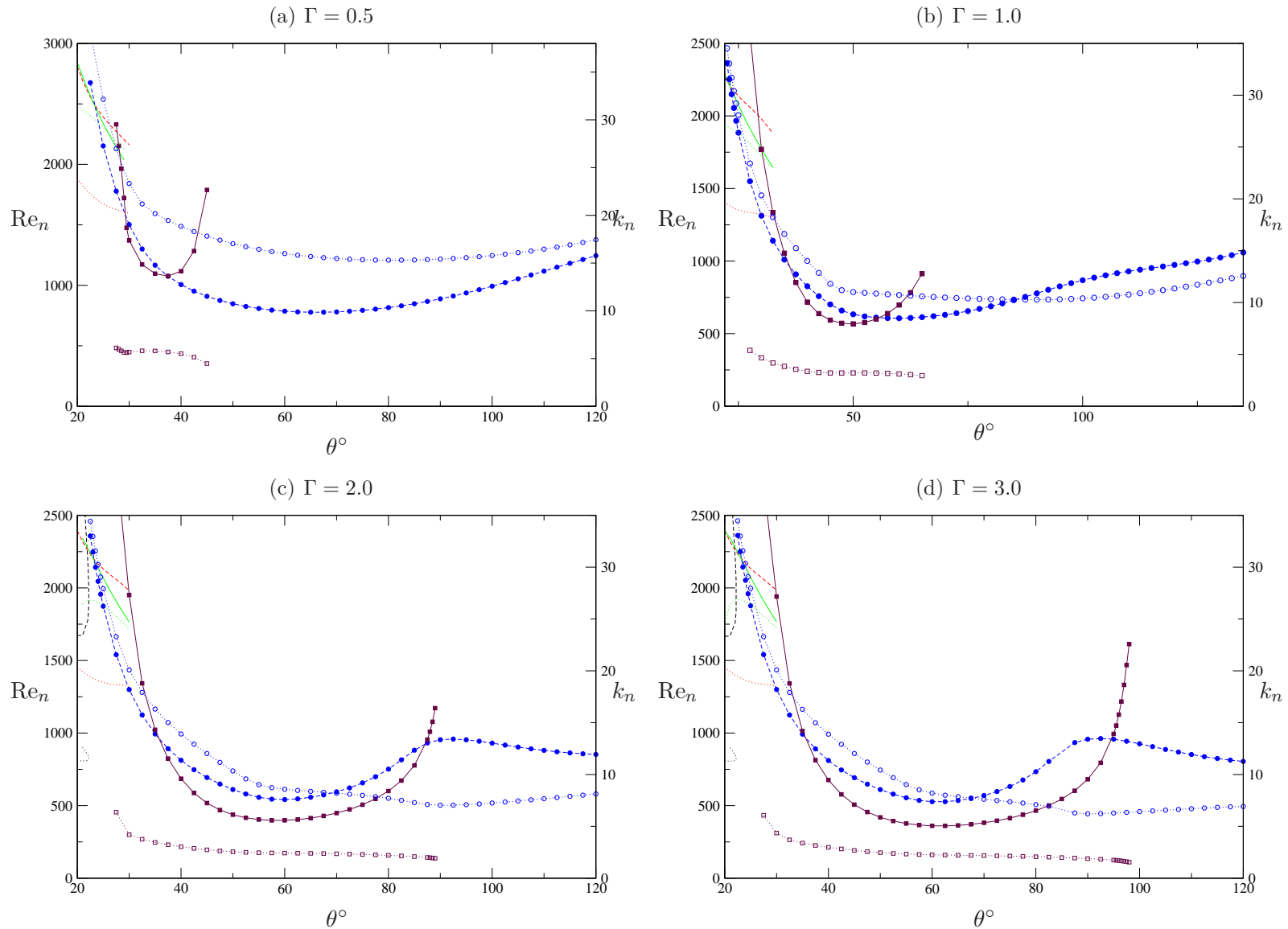


Figure 5.36: Neutral curves for different aspect ratios Γ as indicated. Re_n for modes (2,3,4 and 5) are represented by red dashed, green solid, blue dashed (circles) and maroon solid (squares) lines respectively. Dotted lines (hollow symbols, and same colour scheme) represent corresponding wave number k_n .

behaviour similar to that of rescaled parameters for onside driven rectangular cavities as reported by [Albensoeder \[2004\]](#). Interestingly the value of $Re_n^* = 293.5$ for $\Gamma = 0.1$ and $\theta = 90^\circ$, is very close to the asymptotic limit of rectangular cavity $Re_n^* = 288.2$ as reported by [Albensoeder \[2004\]](#). The comparison of $\omega_n^* = 183.17$ and $k_n^* = 5.64$ for triangular cavity with $\theta = 90^\circ$ and $\Gamma = 0.1$ with $\omega_n^* = 163.7$ and $k_n^* = 5.175$ for a rectangular cavity of aspect ratio $\Gamma = 0.25$ from [Albensoeder \[2004\]](#), suggests that the instability mechanism involved in both geometries is the same.

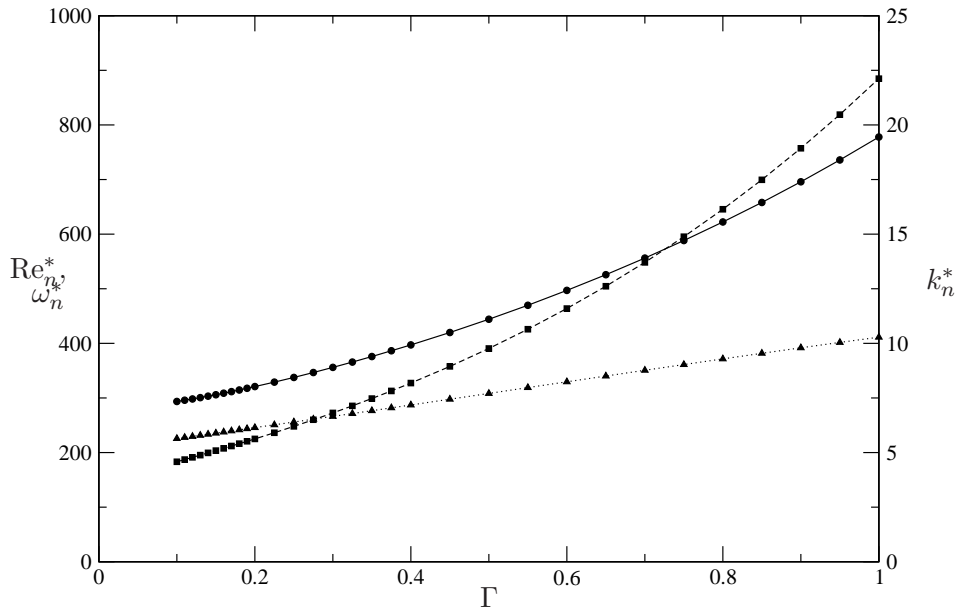


Figure 5.37: Critical data for mode 4 (Re_n^* (circles), ω_n^* (squares) and k_n^* (triangles)) using the scaling (5.1) for shallow cavities at a downstream angle of $\theta = 90^\circ$.

5.2.4 Summary of results

The major observations for instability modes with the lid motion directed towards a specified angle between two sides of specified lengths of a triangular cavity could be summarized as

- For small downstream angles $\theta < 22^\circ$ mode 1 and mode 3 are the dangerous modes, where as mode 3 is active at small aspect ratio $\Gamma < 0.6$ (figure 5.28).

Table 5.4: Limits of downstream angles θ in which different modes are most dangerous at specific aspect ratio Γ .

Γ	Mode 1	Mode 2	Mode 3	Mode 4	Mode 5
0.5		$18^\circ \leq \theta \leq 23.4^\circ$	$\theta \leq 18^\circ$	$23.4^\circ \leq \theta \leq 29.3^\circ$ & $\theta \geq 37.5^\circ$	$29.3^\circ \leq \theta \leq 37.5^\circ$
1.0	$\theta \leq 21.2^\circ$	$21.2^\circ \leq \theta \leq 22.9^\circ$	$22.9^\circ \leq \theta \leq 23.3^\circ$	$23.3^\circ \leq \theta \leq 36^\circ$ & $\theta \geq 55.5^\circ$	$36^\circ \leq \theta \leq 55.5^\circ$
2.0	$\theta \leq 22.2^\circ$	$22.2^\circ \leq \theta \leq 23^\circ$	$23^\circ \leq \theta \leq 23.3^\circ$	$23.3^\circ \leq \theta \leq 35.7^\circ$ & $\theta \geq 87^\circ$	$35.7^\circ \leq \theta \leq 87^\circ$

- At moderately small downstream angles $21^\circ \leq \theta \leq 23.5^\circ$ mode 2 becomes visible as a dangerous mode with neutral curve for Re_n being very close and overlapping with that of mode 3.
- For o downstream angles $\theta \geq 23.5^\circ$ mode 4 and 5 appears as the dangerous modes overlapping each other at different locations depending on Γ and θ .
- For high aspect ratio $\Gamma \rightarrow \infty$ the neutral curves for all the modes tend to take asymptotic value at all the downstream angles.
- For small aspect ratio $\Gamma \ll 1.0$ and higher downstream angles $\theta > 23.5^\circ$ the instability mechanism is centrifugal in nature and the curve for appropriately rescaled Reynolds number Re_n^* shows a trend to take an asymptotic value.

The limits of downstream angles θ at which different modes act as the most dangerous mode are summarized in table 5.4 for representative cases of Γ .

Chapter 6

Conclusions

In this study the linear stability of steady-state two-dimensional flow in triangular cavities was analysed. The angle θ between two sides of the cavity varied from 15° to 135° and the aspect ratio Γ was in the range of $0.2 \leq \Gamma \leq 4.0$. The lid motion was directed either towards the corner where the angle θ was specified or away from it. The instability mechanisms were characterized using the kinetic energy budget and criteria developed for inviscid flow.

All the calculations were made using a numerical code developed for this purpose based on the finite element method. Quadratic interpolation was used for velocities and linear interpolation for pressure. The eigenvalues were determined using the Krylov subspace method. The code was successfully validated by comparing numerical results obtained with some of numerical and experimental results available in literature.

Five different modes of instability were recognized to become critical in the parameter space considered. Two of these modes were identified to be of centrifugal nature from the kinetic energy budget, whereas the remaining were of elliptic nature due to stretching of the primary vortex. One of the centrifugal modes (mode 5) was stationary. The resemblance of wave number k , Reynolds number Re , perturbation flow field and kinetic energy budget for this stationary centrifugal mode with that found in deep rectangular cavities, as reported by [Albensoeder et al. \[2001\]](#), strongly suggests that the instability mechanism involved was the same in both geometries. The second centrifugal mode (mode 4) was oscillatory and was found to be the most dangerous mode for downstream angles

$\theta > 23.5^\circ$ at small aspect ratios $\Gamma \rightarrow 0$. Again the resemblance of the properties of the critical mode and critical data at small aspect ratio with that of centrifugal modes in shallow rectangular cavities [Albensoeder et al. \[2001\]](#) revealed that the instability mechanism was the same.

For small downstream angles $\theta \leq 23.5^\circ$ the primary eddy is strained strongly enough to ensue the elliptic instability mechanisms. All the three elliptic modes occur as critical modes for $\theta \leq 23.5^\circ$ and $0.2 \leq \Gamma \leq 4.0$. Two of these elliptic natured modes are oscillatory. The perturbation flow field at the maxima of kinetic energy production rate for the stationary elliptic mode (mode 3) has a close resemblance with the elliptic instability mode reported for rectangular cavities of $\Gamma = 1.5$ with two facing walls moving in opposite direction by [Albensoeder and Kuhlmann \[2002\]](#).

Occurrence of a certain mode as the most dangerous mode depends on the structure of the basic flow. Changing the parameters of the cavity results in changing the boundary conditions which changes the flow structure in the cavity and thus the flow structure may be prone to different instability mechanisms.

References

- Albensoeder, S. [2004], *Lineare und nichtlineare Stabilität inkompressibler Strömungen im zweiseitig angetriebenen Rechteckbehälter*, Cuvillier Verlag, Göttingen. [77](#)
- Albensoeder, S. and Kuhlmann, H. C. [2002], ‘Linear stability of rectangular cavity flows driven by anti-parallel motion of two facing walls’, *Journal of Fluid Mechanics* **458**, 153–180. [50](#), [80](#)
- Albensoeder, S., Kuhlmann, H. C. and Rath, H. J. [2001], ‘Three-dimensional centrifugal-flow instabilities in the lid-driven cavity problem’, *Phys. Fluids* **13**, 121–135. [3](#), [9](#), [35](#), [45](#), [53](#), [55](#), [79](#), [80](#)
- Anderson, E., Bai, Z., Bischof, C., Blackford, S., Demmel, J., Dongarra, J., Du Croz, J., Greenbaum, A., Hammarling, S., McKenney, A. and Sorensen, D. [1999], *LAPACK Users’ Guide*, third edn, Society for Industrial and Applied Mathematics, Philadelphia, PA. [21](#)
- Batchelor, G. K. [1956], ‘On steady laminar flow with closed streamlines at large Reynolds number’, *J. Fluid Mech.* **1**, 177–190. [2](#)
- Bayly, B. J. [1988], ‘Three-dimensional centrifugal-type instabilities in inviscid two-dimensional flows’, *Phys. Fluids* **31**, 56–64. [2](#), [11](#)
- Ben, Q. L. [2006], *Discontinuous finite elements in fluid dynamics and heat transfer*, Springer Berlin Heidelberg. [12](#)
- Burggraf, O. R. [1966], ‘Analytical and numerical studies of the structure of steady separated flows’, *J. Fluid Mech.* **24**, 113–151. [2](#)

REFERENCES

- Chung, T. J. [1978], *Finite element analysis in fluid dynamics / T. J. Chung*, McGraw-Hill International Book Co., New York. [12](#)
- Demmel, J. W., Eisenstat, S. C., Gilbert, J. R., Li, X. S. and Liu, J. W. H. [1999], ‘A supernodal approach to sparse partial pivoting’, *SIAM J. Matrix Analysis and Applications* **20**(3), 720–755. [17](#), [21](#)
- Di Prima, R. and Swinney, H. [1985], Instabilities and transition in flow between concentric rotating cylinders, *in* H. Swinney and J. Gollub, eds, ‘Hydrodynamic Instabilities and the Transition to Turbulence’, Vol. 45 of *Topics in Applied Physics*, Springer Berlin / Heidelberg, pp. 139–180. [36](#)
- Dick, E. [2009], Introduction to finite element methods in computational fluid dynamics, *in* J. F. Wendt, ed., ‘Computational Fluid Dynamics’, Springer Berlin Heidelberg, pp. 235–274. [12](#)
- Ding, Y. and Kawahara, M. [1998], ‘Linear stability of incompressible flow using a mixed finite element method’, *J. Comput. Phys.* **139**, 243–273. [3](#)
- Eloy, C. and Le Dizès, S. [2001], ‘Stability of the Rankine vortex in a multipolar strain field’, *Phys. Fluids* **13**, 660–676. [43](#), [47](#)
- Erturk, E. and Gokcol, O. [2007], ‘Fine grid numerical solutions of triangular cavity flow’, *Eur. Phys. J. Appl. Phys.* **38**, 97–105. [1](#), [30](#), [31](#)
- Gaskell, P., Thompson, H. and Savage, M. [1999], A finite element analysis of steady viscous flow in triangular cavities, *in* ‘Proceedings of the Institution of Mechanical Engineers Part C-Journal of Mechanical Engineering Science’, Vol. 213, pp. 263–276. [1](#)
- Geuzaine, C. and Remacle, J.-F. [2003], *Gmsh Reference Manual*, 1.12 edn, <http://www.geuz.org/gmsh>. [24](#)
- Ghia, U., Ghia, K. and Shin, C. [1982], ‘High-re solutions for incompressible flow using the Navier-Stokes equations and a multigrid method’, *J. Comput. Physics* **48**, 387–411. [2](#)

- GONZÁLEZ, L. M., AHMED, M., KÜHNEN, J., KUHLMANN, H. C. and THEOFILIS, V. [2011], ‘Three-dimensional flow instability in a lid-driven isosceles triangular cavity’, *Journal of Fluid Mechanics* **675**, 369–396.
URL: <http://dx.doi.org/10.1017/S002211201100022X> 4
- González, L. M., Theofilis, V. and Gómez-Blanco, R. [2007], ‘Finite-element numerical methods for viscous incompressible BiGlobal linear instability analysis on unstructured meshes’, *AIAA J.* **45**, 840–854. 3, 8
- Jyotsna, R. and Vanka, S. P. [1995], ‘Multigrid calculation of steady, viscous flow in a triangular cavity’, *J. Comput. Phys.* **122**, 107–117. 1
- Kawaguti, M. [1961], ‘Numerical solution of the Navier-Stokes equations for the flow in a two-dimensional cavity’, *J. Phys. Soc. Jpn.* **16**, 2307–2315. 2
- Kerswell, R. R. [2002], ‘Elliptical instability’, *Annu. Rev. Fluid Mech.* **34**, 83–113. 2, 11, 44, 47
- Koseff, J. R. and Street, R. L. [1984a], ‘The lid-driven cavity flow: A synthesis of qualitative and quantitative observations’, *Journal of Fluids Engineering* **106**(4), 390–398.
URL: <http://link.aip.org/link/?JFG/106/390/1> 3
- Koseff, J. R. and Street, R. L. [1984b], ‘On end wall effects in a lid-driven cavity flow’, *Journal of Fluids Engineering* **106**(4), 385–389.
URL: <http://link.aip.org/link/?JFG/106/385/1> 3
- Koseff, J., Street, R., Gresho, P., Upson, C., J.A.C.Humphrey and To, W. [1983], Three-dimensional lid-driven cavity flow: experiment and simulation, *in* ‘International Conference on Numerical Methods in Laminar and Turbulent Flow, Seattle, WA, USA, 8 Aug 1983’. 3
- Kuhlmann, H. and Albensoeder, S. [2004], Strained vortices in driven cavities, 75th Annual GAMM Conference, Dresden/Germany. 3
- Kuhlmann, H. and Albensoeder, S. [2008], ‘Three-dimensional flow instabilities in a thermocapillary-driven cavity’, *Phys. Rev. E* **77**, 036303–1–036303–15. 48

REFERENCES

- Kuhlmann, H. C., Wanschura, M. and Rath, H. J. [1997], ‘Flow in two-sided lid-driven cavities: Non-uniqueness, instabilities, and cellular structures’, *J. Fluid Mech.* **336**, 267–299. [50](#)
- Kuhlmann, H. C., Wanschura, M. and Rath, H. J. [1998], ‘Elliptic instability in two-sided liddriven cavity flow’, *European Journal of Mechanics- B/FLUID* **17**, 561–569. [44](#)
- Kühnen, J. [2006], Experimentelle Untersuchung strömungsmechanischer Instabilitäten in einem einseitig angetriebenen Dreieckbehälter, Master’s thesis, Vienna University of Technology. [3](#), [31](#), [36](#)
- Laure, P., Roux, B. and Ben Hadid, H. [1990], ‘Nonlinear study of the flow in a long rectangular cavity subjected to thermocapillary effect’, *Phys. Fluids A* **2**, 516–524. [45](#)
- Li, M. and Tang, T. [1996], ‘Steady viscous flow in a triangular cavity by efficient numerical techniques’, *Computers and Mathematics with Applications* **31**, 55–65. [1](#)
- Meerbergen, K., Spence, A. and Roose, D. [1994], ‘Shift-invert and cayley transforms for detection of rightmost eigenvalues of nonsymmetric matrices’, *BIT Numerical Mathematics* **34**, 409–423. [10.1007/BF01935650](https://doi.org/10.1007/BF01935650).
URL: <http://dx.doi.org/10.1007/BF01935650> [21](#), [22](#)
- Moffat, H. K. [1963], ‘Viscous and resistive eddies near a sharp corner’, *J. Fluid Mech.* **18**, 1–18. [2](#)
- Pan, F. and Acrivos, A. [1967], ‘Steady flows in rectangular cavities’, *J. Fluid Mech.* **28**, 643–655. [2](#)
- Prasad, A. K. and Koseff, J. R. [1989], ‘Reynolds number and end-wall effects on a lid-driven cavity flow’, *Physiscs of Fluids A* **1**(208). [3](#)
- Rayleigh, Lord [1917], ‘On the dynamics of revolving fluids’, *Proc. Roy. Soc. London A* **93**, 148–154. [10](#)

REFERENCES

- Rhee, H. S., Koseff, J. R. and Street, R. L. [1984], ‘Flow visualization of a recirculating flow by rheoscopic liquid and liquid crystal techniques’, *Experiments in Fluids* **2**(57–64), 390–398. [3](#)
- Ribbens, C. J., Watson, L. T. and Wang, C.-Y. [1994], ‘Steady viscous flow in a triangular cavity’, *J. Comput. Phys.* **112**, 173–181. [1](#)
- Roberts, P. [1960], ‘Characteristic value problems posed by differential equations arising in hydrodynamics and hydromagnetics’, *Journal of Mathematical Analysis and Applications* **1**(2), 195–214.
URL: <http://www.sciencedirect.com/science/article/B6WK2-4CRM7WD-1JW/2/7cac7395582fd379a9ceda36de3dbc68> [36](#)
- Saad, Y. [1980], ‘Variations of Arnoldi’s method for computing eigenlements of large unsymmetric matrices’, *Lin. Algebra. Appl.* **34**, 269–295. [20](#)
- Schöberl, J. [1997], ‘Netgen an advancing front 2d/3d-mesh generator based on abstract rules’, *Computing and Visualization in Science* **1**, 41–52. [10.1007/s007910050004](https://doi.org/10.1007/s007910050004).
URL: <http://dx.doi.org/10.1007/s007910050004> [24](#)
- Schreiber, R. and Keller, H. [1983], ‘Driven cavity flows by efficient numerical techniques’, *J. Comput. Physics* **49**, 310–333. [2](#)
- Shewchuk, J. R. [1996], Triangle: Engineering a 2D Quality Mesh Generator and Delaunay Triangulator, in M. C. Lin and D. Manocha, eds, ‘Applied Computational Geometry: Towards Geometric Engineering’, Vol. 1148 of *Lecture Notes in Computer Science*, Springer-Verlag, pp. 203–222. From the First ACM Workshop on Applied Computational Geometry. [24](#)
- Siegmann-Hegerfeld, T., Albensoeder, S. and Kuhlmann, H. C. [2008], ‘Two- and three-dimensional flows in nearly rectangular cavities driven by collinear motion of two facing walls’, *Exp Fluids* **45**, 781–796. [3](#)
- Simuni, L. M. [1964], ‘Numerical solution of the problem of the motion of a fluid in a rectangular hole’, *Inzh. Zh.* **4**, 446. [2](#)

REFERENCES

- Sipp, D. and Jacquin, L. [1998], ‘Elliptic instability in two-dimensional flattened Taylor–Green vortices’, *Phys. Fluids* **10**, 839–849. [11](#)
- Sipp, D. and Jacquin, L. [2000], ‘Three-dimensional centrifugal-type instabilities of two-dimensional flows in rotating systems’, *Phys. Fluids* **12**, 1740–1748. [2](#), [3](#), [11](#)
- Sparrow, E. M., Munro, W. D. and Jonsson, V. K. [1964], ‘Instability of the flow between rotating cylinders: the wide-gap problem’, *jfm* **20**(01), 35–46.
URL: <http://dx.doi.org/10.1017/S0022112064001008> [36](#)
- Theofilis, V. [2000], Globally unstable basic flows in open cavities, in ‘6th AIAA Aeroacoustics Conference and Exhibit, Lahaina, HI, USA’, AIAA Paper 2000-1965. [3](#)
- Theofilis, V. [2003], ‘Advances in global linear instability analysis of nonparallel and three-dimensional flows’, *Prog. Aero. Sci.* **39**, 249–315. [20](#)
- Walowit, J., Tsao, S. and DiPrima, R. [1964], ‘Stability of a flow between arbitrary spaced concentric cylindrical surfaces including the effect of a radial temperature gradient’, *Tr. ASME, J. Appl. Mech* **31**, 585–593. [36](#)
- Zienkiewicz, O., Taylor, R. and Nithiarasu, P. [2008], *Finite Element Method for Fluid Dynamics (6th Edition)*, Elsevier. [12](#)

Curriculum Vitae

Personal Data

Name: Manzoor Ahmed
Date of Birth: 25.05.1977
Place of Birth: Swabi/NWFP/Pakistan
Nationality: Pakistani
Marital Status: Married
Address: E322, Resselgasse 3, 1040 Wien, Austria
Phone: +43 1 58801 32247
Fax: +43 1 58801 32299
Email: amanzoor@mail.tuwien.ac.at



Education

Since 05/2007	Doctoral studies at the Institute of Fluid Mechanics and Heat Transfer, Vienna University of Technology, Austria.
09/2003	M.Sc. Nuclear Engineering from Pakistan Institute of Engineering and Applied Sciences, Islamabad, Pakistan.
09/2001	B.Sc. Mining Engineering from N.W.F.P. University of Engineering & Technology, Peshawar, Pakistan.
06/1996	Higher Secondary School certificate from Pakistan International Public School and College, Abbottabad, Pakistan.
1993	Secondary School certificate from Pakistan International Public School and College, Abbottabad, Pakistan.

Employment

09/2003-05/2007 Researcher at Pakistan Atomic Energy Commission of Pakistan.

Research

Research Interests

Fluid Mechanics, Hydrodynamic Stability, Numerical Methods

Publications

L. M. Gonzalez, M. Ahmed, J. Kühnen, H. C. Kuhlmann and V. Theofilis, Three-dimensional flow instability in a lid-driven isosceles triangular cavity, *Journal of Fluid Mechanics* (to appear).

M. Ahmed and H. C. Kuhlmann Flow instability in triangular lid-driven cavities with wall motion away from a rectangular corner (in preparation)